



CHORUS

This is the accepted manuscript made available via CHORUS. The article has been published as:

Cumulants and correlation functions of net-proton, proton, and antiproton multiplicity distributions in $m_{\text{row}} > m_{\text{Au}} > m_{\text{mo}} > + / m_{\text{mo}} > m_{\text{Au}} > / m_{\text{row}} > / \text{math}$ collisions at energies available at the BNL Relativistic Heavy Ion Collider

M. S. Abdallah et al. (STAR Collaboration)

Phys. Rev. C **104**, 024902 — Published 5 August 2021

DOI: [10.1103/PhysRevC.104.024902](https://doi.org/10.1103/PhysRevC.104.024902)

Cumulants and Correlation Functions of Net-proton, Proton and Antiproton Multiplicity Distributions in Au+Au Collisions at RHIC

M. S. Abdallah,⁵ J. Adam,⁶ L. Adamczyk,² J. R. Adams,³⁹ J. K. Adkins,³⁰ G. Agakishiev,²⁸ I. Aggarwal,⁴¹
M. M. Aggarwal,⁴¹ Z. Ahammed,⁶¹ I. Alekseev,^{3,35} D. M. Anderson,⁵⁵ A. Aparin,²⁸ E. C. Aschenauer,⁶
M. U. Ashraf,¹¹ F. G. Atetalla,²⁹ A. Attri,⁴¹ G. S. Averichev,²⁸ V. Bairathi,⁵³ W. Baker,¹⁰ J. G. Ball Cap,²⁰
K. Barish,¹⁰ A. Behera,⁵² R. Bellwied,²⁰ P. Bhagat,²⁷ A. Bhasin,²⁷ J. Bielcik,¹⁴ J. Bielcikova,³⁸ I. G. Bordyuzhin,³
J. D. Brandenburg,⁶ A. V. Brandin,³⁵ I. Bunzarov,²⁸ J. Butterworth,⁴⁵ X. Z. Cai,⁵⁰ H. Caines,⁶⁴
M. Calderón de la Barca Sánchez,⁸ D. Cebra,⁸ I. Chakaberia,^{31,6} P. Chaloupka,¹⁴ B. K. Chan,⁹ F-H. Chang,³⁷
Z. Chang,⁶ N. Chankova-Bunzarova,²⁸ A. Chatterjee,¹¹ S. Chattopadhyay,⁶¹ D. Chen,¹⁰ J. Chen,⁴⁹ J. H. Chen,¹⁸
X. Chen,⁴⁸ Z. Chen,⁴⁹ J. Cheng,⁵⁷ M. Chevalier,¹⁰ S. Choudhury,¹⁸ W. Christie,⁶ X. Chu,⁶ H. J. Crawford,⁷
M. Csanád,¹⁶ M. Daugherty,¹ T. G. Dedovich,²⁸ I. M. Deppner,¹⁹ A. A. Derevschikov,⁴³ A. Dhamija,⁴¹
L. Di Carlo,⁶³ L. Didenko,⁶ X. Dong,³¹ J. L. Drachenberg,¹ J. C. Dunlop,⁶ N. Elsey,⁶³ J. Engelage,⁷ G. Eppley,⁴⁵
S. Esumi,⁵⁸ O. Evdokimov,¹² A. Ewigleben,³² O. Eyser,⁶ R. Fatemi,³⁰ F. M. Fawzi,⁵ S. Fazio,⁶ P. Federic,³⁸
J. Fedorisin,²⁸ C. J. Feng,³⁷ Y. Feng,⁴⁴ P. Filip,²⁸ E. Finch,⁵¹ Y. Fisyak,⁶ A. Francisco,⁶⁴ C. Fu,¹¹
L. Fulek,² C. A. Gagliardi,⁵⁵ T. Galatyuk,¹⁵ F. Geurts,⁴⁵ N. Ghimire,⁵⁴ A. Gibson,⁶⁰ K. Gopal,²³ X. Gou,⁴⁹
D. Grosnick,⁶⁰ A. Gupta,²⁷ W. Guryn,⁶ A. I. Hamad,²⁹ A. Hamed,⁵ Y. Han,⁴⁵ S. Harabasz,¹⁵ M. D. Harasty,⁸
J. W. Harris,⁶⁴ H. Harrison,³⁰ S. He,¹¹ W. He,¹⁸ X. H. He,²⁶ Y. He,⁴⁹ S. Heppelmann,⁸ S. Heppelmann,⁴²
N. Herrmann,¹⁹ E. Hoffman,²⁰ L. Holub,¹⁴ Y. Hu,¹⁸ H. Huang,³⁷ H. Z. Huang,⁹ S. L. Huang,⁵² T. Huang,³⁷
X. Huang,⁵⁷ Y. Huang,⁵⁷ T. J. Humanic,³⁹ D. Isenhower,¹ W. W. Jacobs,²⁵ C. Jena,²³ A. Jentsch,⁶ Y. Ji,³¹
J. Jia,^{6,52} K. Jiang,⁴⁸ X. Ju,⁴⁸ E. G. Judd,⁷ S. Kabana,⁵³ M. L. Kabir,¹⁰ S. Kagamaster,³² D. Kalinkin,^{25,6}
K. Kang,⁵⁷ D. Kapukchyan,¹⁰ K. Kauder,⁶ H. W. Ke,⁶ D. Keane,²⁹ A. Kechechyan,²⁸ Y. V. Khyzhniak,³⁵
D. P. Kikoła,⁶² C. Kim,¹⁰ B. Kimelman,⁸ D. Kincses,¹⁶ I. Kisel,¹⁷ A. Kiselev,⁶ A. G. Knospe,³² L. Kochenda,³⁵
L. K. Kosarzewski,¹⁴ L. Kramerik,¹⁴ P. Kravtsov,³⁵ L. Kumar,⁴¹ S. Kumar,²⁶ R. Kunnawalkam Elayavalli,⁶⁴
J. H. Kwasizur,²⁵ R. Lacey,⁵² S. Lan,¹¹ J. M. Landgraf,⁶ J. Lauret,⁶ A. Lebedev,⁶ R. Lednicky,²⁸ J. H. Lee,⁶
Y. H. Leung,³¹ C. Li,⁴⁹ C. Li,⁴⁸ W. Li,⁴⁵ X. Li,⁴⁸ Y. Li,⁵⁷ X. Liang,¹⁰ Y. Liang,²⁹ R. Licenik,³⁸ T. Lin,⁵⁵
Y. Lin,¹¹ M. A. Lisa,³⁹ F. Liu,¹¹ H. Liu,²⁵ P. Liu,⁵² T. Liu,⁶⁴ X. Liu,³⁹ Y. Liu,⁵⁵ Z. Liu,⁴⁸ T. Ljubicic,⁶
W. J. Llope,⁶³ R. S. Longacre,⁶ E. Loyd,¹⁰ N. S. Lukow,⁵⁴ X. Luo,¹¹ L. Ma,¹⁸ R. Ma,⁶ Y. G. Ma,¹⁸ N. Magdy,¹²
R. Majka,^{64,*} D. Mallick,³⁶ S. Margetis,²⁹ C. Markert,⁵⁶ H. S. Matis,³¹ J. A. Mazer,⁴⁶ N. G. Minaev,⁴³
S. Mioduszewski,⁵⁵ B. Mohanty,³⁶ M. M. Mondal,⁵² I. Mooney,⁶³ D. A. Morozov,⁴³ A. Mukherjee,¹⁶ M. Nagy,¹⁶
J. D. Nam,⁵⁴ Md. Nasim,²² K. Nayak,¹¹ D. Neff,⁹ J. M. Nelson,⁷ D. B. Nemes,⁶⁴ M. Nie,⁴⁹ G. Nigmatkulov,³⁵
T. Niida,⁵⁸ R. Nishitani,⁵⁸ L. V. Nogach,⁴³ T. Nonaka,⁵⁸ A. S. Nunes,⁶ G. Odyniec,³¹ A. Ogawa,⁶ S. Oh,³¹
V. A. Okorokov,³⁵ B. S. Page,⁶ R. Pak,⁶ A. Pandav,³⁶ A. K. Pandey,⁵⁸ Y. Panebratsev,²⁸ P. Parfenov,³⁵
B. Pawlik,⁴⁰ D. Pawlowska,⁶² H. Pei,¹¹ C. Perkins,⁷ L. Pinsky,²⁰ R. L. Pintér,¹⁶ J. Pluta,⁶² B. R. Pokhrel,⁵⁴
G. Pomiatkin,³⁸ J. Porter,³¹ M. Posik,⁵⁴ V. Prozorova,¹⁴ N. K. Pruthi,⁴¹ M. Przybycien,² J. Putschke,⁶³
H. Qiu,²⁶ A. Quintero,⁵⁴ C. Racz,¹⁰ S. K. Radhakrishnan,²⁹ N. Raha,⁶³ R. L. Ray,⁵⁶ R. Reed,³² H. G. Ritter,³¹
M. Robotkova,³⁸ O. V. Rogachevskiy,²⁸ J. L. Romero,⁸ L. Ruan,⁶ J. Rusnak,³⁸ N. R. Sahoo,⁴⁹ H. Sako,⁵⁸ S. Salur,⁴⁶
J. Sandweiss,^{64,*} S. Sato,⁵⁸ W. B. Schmidke,⁶ N. Schmitz,³³ B. R. Schweid,⁵² F. Seck,¹⁵ J. Seger,¹³ M. Sergeeva,⁹
R. Seto,¹⁰ P. Seyboth,³³ N. Shah,²⁴ E. Shaliev,²⁸ P. V. Shanmuganathan,⁶ M. Shao,⁴⁸ T. Shao,⁵⁰ A. I. Sheikh,²⁹
D. Shen,⁵⁰ S. S. Shi,¹¹ Y. Shi,⁴⁹ Q. Y. Shou,¹⁸ E. P. Sichtermann,³¹ R. Sikora,² M. Simko,³⁸ J. Singh,⁴¹ S. Singha,²⁶
M. J. Skoby,⁴⁴ N. Smirnov,⁶⁴ Y. Söhngen,¹⁹ W. Solyst,²⁵ P. Sorensen,⁶ H. M. Spinka,^{4,*} B. Srivastava,⁴⁴
T. D. S. Stanislaus,⁶⁰ M. Stefaniak,⁶² D. J. Stewart,⁶⁴ M. Strikhanov,³⁵ B. Stringfellow,⁴⁴ A. A. P. Suaide,⁴⁷
M. Sumera,³⁸ B. Summa,⁴² X. M. Sun,¹¹ X. Sun,¹² Y. Sun,⁴⁸ Y. Sun,²¹ B. Surrow,⁵⁴ D. N. Svirida,³
Z. W. Sweger,⁸ P. Szymanski,⁶² A. H. Tang,⁶ Z. Tang,⁴⁸ A. Taranenko,³⁵ T. Tarnowsky,³⁴ J. H. Thomas,³¹
A. R. Timmins,²⁰ D. Tlusty,¹³ T. Todoroki,⁵⁸ M. Tokarev,²⁸ C. A. Tomkiel,³² S. Trentalange,⁹ R. E. Tribble,⁵⁵
P. Tribedy,⁶ S. K. Tripathy,¹⁶ T. Truhlar,¹⁴ B. A. Trzeciak,¹⁴ O. D. Tsai,⁹ Z. Tu,⁶ T. Ullrich,⁶ D. G. Underwood,⁴
I. Upsal,^{49,6} G. Van Buren,⁶ J. Vanek,³⁸ A. N. Vasiliev,⁴³ I. Vassiliev,¹⁷ V. Verkest,⁶³ F. Videbæk,⁶ S. Vokal,²⁸
S. A. Voloshin,⁶³ F. Wang,⁴⁴ G. Wang,⁹ J. S. Wang,²¹ P. Wang,⁴⁸ Y. Wang,¹¹ Y. Wang,⁵⁷ Z. Wang,⁴⁹ J. C. Webb,⁶
P. C. Weidenkaff,¹⁹ L. Wen,⁹ G. D. Westfall,³⁴ H. Wieman,³¹ S. W. Wissink,²⁵ R. Witt,⁵⁹ J. Wu,²⁶ Y. Wu,¹⁰
B. Xi,⁵⁰ Z. G. Xiao,⁵⁷ G. Xie,³¹ W. Xie,⁴⁴ H. Xu,²¹ N. Xu,³¹ Q. H. Xu,⁴⁹ Y. Xu,⁴⁹ Z. Xu,⁶ Z. Xu,⁹ C. Yang,⁴⁹
Q. Yang,⁴⁹ S. Yang,⁴⁵ Y. Yang,³⁷ Z. Yang,¹¹ Z. Ye,⁴⁵ Z. Ye,¹² L. Yi,⁴⁹ K. Yip,⁶ Y. Yu,⁴⁹ H. Zbroszczyk,⁶²
W. Zha,⁴⁸ C. Zhang,⁵² D. Zhang,¹¹ S. Zhang,¹² S. Zhang,¹⁸ X. P. Zhang,⁵⁷ Y. Zhang,²⁶ Y. Zhang,⁴⁸ Y. Zhang,¹¹
Z. J. Zhang,³⁷ Z. Zhang,⁶ Z. Zhang,¹² J. Zhao,⁴⁴ C. Zhou,¹⁸ X. Zhu,⁵⁷ Z. Zhu,⁴⁹ M. Zurek,³¹ and M. Zyzak¹⁷

(STAR Collaboration)

- 53
54
55
56
57
58
59
60
61
62
63
64
65
66
67
68
69
70
71
72
73
74
75
76
77
78
79
80
81
82
83
84
85
86
87
88
89
90
91
92
93
94
95
96
97
98
99
100
101
102
103
104
105
106
107
108
109
110
111
112
113
114
115
- ¹Abilene Christian University, Abilene, Texas 79699
²AGH University of Science and Technology, FPACS, Cracow 30-059, Poland
³Alikhanov Institute for Theoretical and Experimental Physics NRC "Kurchatov Institute", Moscow 117218, Russia
⁴Argonne National Laboratory, Argonne, Illinois 60439
⁵American University of Cairo, New Cairo 11835, New Cairo, Egypt
⁶Brookhaven National Laboratory, Upton, New York 11973
⁷University of California, Berkeley, California 94720
⁸University of California, Davis, California 95616
⁹University of California, Los Angeles, California 90095
¹⁰University of California, Riverside, California 92521
¹¹Central China Normal University, Wuhan, Hubei 430079
¹²University of Illinois at Chicago, Chicago, Illinois 60607
¹³Creighton University, Omaha, Nebraska 68178
¹⁴Czech Technical University in Prague, FNSPE, Prague 115 19, Czech Republic
¹⁵Technische Universität Darmstadt, Darmstadt 64289, Germany
¹⁶ELTE Eötvös Loránd University, Budapest, Hungary H-1117
¹⁷Frankfurt Institute for Advanced Studies FIAS, Frankfurt 60438, Germany
¹⁸Fudan University, Shanghai, 200433
¹⁹University of Heidelberg, Heidelberg 69120, Germany
²⁰University of Houston, Houston, Texas 77204
²¹Huzhou University, Huzhou, Zhejiang 313000
²²Indian Institute of Science Education and Research (IISER), Berhampur 760010, India
²³Indian Institute of Science Education and Research (IISER) Tirupati, Tirupati 517507, India
²⁴Indian Institute Technology, Patna, Bihar 801106, India
²⁵Indiana University, Bloomington, Indiana 47408
²⁶Institute of Modern Physics, Chinese Academy of Sciences, Lanzhou, Gansu 730000
²⁷University of Jammu, Jammu 180001, India
²⁸Joint Institute for Nuclear Research, Dubna 141 980, Russia
²⁹Kent State University, Kent, Ohio 44242
³⁰University of Kentucky, Lexington, Kentucky 40506-0055
³¹Lawrence Berkeley National Laboratory, Berkeley, California 94720
³²Lehigh University, Bethlehem, Pennsylvania 18015
³³Max-Planck-Institut für Physik, Munich 80805, Germany
³⁴Michigan State University, East Lansing, Michigan 48824
³⁵National Research Nuclear University MPhI, Moscow 115409, Russia
³⁶National Institute of Science Education and Research, HBNI, Jatni 752050, India
³⁷National Cheng Kung University, Tainan 70101
³⁸Nuclear Physics Institute of the CAS, Rez 250 68, Czech Republic
³⁹Ohio State University, Columbus, Ohio 43210
⁴⁰Institute of Nuclear Physics PAN, Cracow 31-342, Poland
⁴¹Panjab University, Chandigarh 160014, India
⁴²Pennsylvania State University, University Park, Pennsylvania 16802
⁴³NRC "Kurchatov Institute", Institute of High Energy Physics, Protvino 142281, Russia
⁴⁴Purdue University, West Lafayette, Indiana 47907
⁴⁵Rice University, Houston, Texas 77251
⁴⁶Rutgers University, Piscataway, New Jersey 08854
⁴⁷Universidade de São Paulo, São Paulo, Brazil 05314-970
⁴⁸University of Science and Technology of China, Hefei, Anhui 230026
⁴⁹Shandong University, Qingdao, Shandong 266237
⁵⁰Shanghai Institute of Applied Physics, Chinese Academy of Sciences, Shanghai 201800
⁵¹Southern Connecticut State University, New Haven, Connecticut 06515
⁵²State University of New York, Stony Brook, New York 11794
⁵³Instituto de Alta Investigación, Universidad de Tarapacá, Arica 1000000, Chile
⁵⁴Temple University, Philadelphia, Pennsylvania 19122
⁵⁵Texas A&M University, College Station, Texas 77843
⁵⁶University of Texas, Austin, Texas 78712
⁵⁷Tsinghua University, Beijing 100084
⁵⁸University of Tsukuba, Tsukuba, Ibaraki 305-8571, Japan
⁵⁹United States Naval Academy, Annapolis, Maryland 21402
⁶⁰Valparaiso University, Valparaiso, Indiana 46383
⁶¹Variable Energy Cyclotron Centre, Kolkata 700064, India
⁶²Warsaw University of Technology, Warsaw 00-661, Poland

⁶³Wayne State University, Detroit, Michigan 48201

⁶⁴Yale University, New Haven, Connecticut 06520

(Dated: June 29, 2021)

We report a systematic measurement of cumulants, C_n , for net-proton, proton and antiproton multiplicity distributions, and correlation functions, κ_n , for proton and antiproton multiplicity distributions up to the fourth order in Au+Au collisions at $\sqrt{s_{NN}} = 7.7, 11.5, 14.5, 19.6, 27, 39, 54.4, 62.4$ and 200 GeV. The C_n and κ_n are presented as a function of collision energy, centrality and kinematic acceptance in rapidity, y , and transverse momentum, p_T . The data were taken during the first phase of the Beam Energy Scan (BES) program (2010 – 2017) at the Relativistic Heavy Ion Collider (RHIC) facility. The measurements are carried out at midrapidity ($|y| < 0.5$) and transverse momentum $0.4 < p_T < 2.0$ GeV/ c , using the STAR detector at RHIC. We observe a non-monotonic energy dependence ($\sqrt{s_{NN}} = 7.7 - 62.4$ GeV) of the net-proton C_4/C_2 with the significance of 3.1σ for the 0-5% central Au+Au collisions. This is consistent with the expectations of critical fluctuations in a QCD-inspired model. Thermal and transport model calculations show a monotonic variation with $\sqrt{s_{NN}}$. For the multiparticle correlation functions, we observe significant negative values for a two-particle correlation function, κ_2 , of protons and antiprotons, which are mainly due to the effects of baryon number conservation. Furthermore, it is found that the four-particle correlation function, κ_4 , of protons plays a role in determining the energy dependence of proton C_4/C_1 below 19.6 GeV, which cannot be solely understood by the negative values of κ_2 for protons.

I. INTRODUCTION

The main goal of the BES program at the RHIC is to study the QCD phase structure [1, 2]. This is expected to lead to the mapping of the phase diagram for strong interactions in the space of temperature (T) versus baryon chemical potential (μ_B). Both theoretically and experimentally, several advancements have been made towards this goal. Lattice QCD calculations have established that at high temperatures, there occurs a crossover transition from hadronic matter to a deconfined state of quarks and gluons at $\mu_B = 0$ MeV [3]. Experimental data from RHIC and the Large Hadron Collider (LHC) have provided evidence of this matter with quark and gluon degrees of freedom called the Quark-Gluon Plasma (QGP) [4–7]. The QGP has been found to hadronize into a gas of hadrons, which undergoes chemical freeze-out (inelastic collisions cease) [8] at a temperature close to the lattice QCD-estimated quark-hadron transition temperature at $\mu_B = 0$ MeV [9, 10]. A suite of interesting results from the BES program indicate a change of equation of state of QCD matter, with collision energy from partonic-interaction-dominated matter at higher collision energies to a hadronic-interaction regime at lower energies. These include the observations of breakdown in the number of constituent-quark scaling of the elliptic flow at lower $\sqrt{s_{NN}}$ [11], non-monotonic variation of the slope of the directed flow for protons and net-protons at midrapidity as a function of $\sqrt{s_{NN}}$ [12], nuclear modification factor changing values from smaller than unity to larger than unity at high p_T as we go to lower $\sqrt{s_{NN}}$ [13], and finite to vanishing values of the three-particle correlations with respect to the event plane [14] as we go to lower $\sqrt{s_{NN}}$.

The QCD phase structure at finite temperature and baryon chemical potential has been extensively studied by various QCD-based model calculations, such as the Dyson-Schwinger Equation (DSE) method [15–19], Functional Renormalization Group (FRG) [20], Nambu-Jona-Lasinio (NJL) [21], Polyakov Nambu-Jona-Lasinio (PNJL) [22–24] and other effective models [25, 26]. One of the most important studies of the QCD phase structure relates to the first-order phase boundary and the expected existence of the critical point (CP) [27–32]. This is the end point of a first-order phase boundary between quark-gluon and hadronic phases [33, 34]. Experimental confirmation of the CP would be a landmark of exploring the QCD phase structure. Previous studies of higher-order cumulants of net-proton multiplicity distributions suggest that the possible CP region is unlikely to be below $\mu_B = 200$ MeV [35], which is consistent with the theoretical findings [19, 20, 29, 31, 36]. The versatility of the RHIC machine has permitted the colliding energies of ions to be varied below the injection energy of $\sqrt{s_{NN}} = 19.6$ GeV [37], and thereby the RHIC BES program provides the possibility to scan the QCD phase diagram up to $\mu_B = 420$ MeV with the collider mode, and $\mu_B = 720$ MeV with the fixed-target mode [2, 38]. This, in turn, opens the possibility to find the experimental signatures of a first-order phase transition and the CP [39, 40].

Higher-order cumulants of the distributions of conserved charge, such as net-baryon (B), net-charge (Q), and net-strangeness (S) numbers, are sensitive to the QCD phase transition and CP [41–51]. The signatures of conserved-charge fluctuations near CP have been studied by various model calculations [46, 47, 52–65]. However, these model calculations are based on the assumption of thermal equilibrium with a static and infinite medium. In heavy-ion collisions, finite-size and time effects will put constraints on the significance of the signals [66, 67]. A theoretical calculation suggests the non-equilibrium correlation length $\xi \approx 2-3$ fm for heavy-

* Deceased

ion collisions [68]. Dynamical modeling of heavy-ion collisions with the physics of a critical point and non-equilibrium effects is in progress [69–73]. The signatures of a phase transition or a CP are detectable if they survive the evolution of the system [74]. Due to a stronger dependence on the correlation length (ξ) [46–48], it is proposed to study the higher moments – skewness ($S = \langle(\delta N)^3\rangle/\sigma^3$) and kurtosis ($\kappa = \langle(\delta N)^4\rangle/\sigma^4 - 3$) with $\delta N = N - \langle N \rangle$, or cumulants C_n (defined in Sec. II E) of distributions of conserved quantities. Both the magnitude and the sign of the moments or C_n [47, 75], which quantify the shape of the multiplicity distributions, are important for understanding the phase transition and CP effects. The aim is to search for signatures of the CP over a broad range of μ_B in the QCD phase diagram [35].

Furthermore, the products of the moments or ratios of C_n can be related to susceptibilities associated with the conserved numbers. The product ($\kappa\sigma^2$), or equivalently, the ratio (C_4/C_2) of the net-baryon number distribution is related to the ratio of fourth-order (χ_4^B) to second-order (χ_2^B) baryon number susceptibilities [44, 50, 76–78]. The ratio, χ_4^B/χ_2^B , is expected to deviate from unity near the CP. It has different values for the hadronic and partonic phases [78]. Similarly, the products $S\sigma$ (C_3/C_2) and $\sigma^2/\langle N \rangle$ (C_2/C_1) are related to χ_3^B/χ_2^B and χ_2^B/χ_1^B , respectively. Experimentally, it is not possible to measure the net-baryon distributions, however, theoretical calculations have shown that net-proton multiplicity ($N_p - N_{\bar{p}} = \Delta N_p$) fluctuations reflect the singularity of the charge and baryon number susceptibility, as expected at the CP [43]. Refs. [79, 80] discuss the effect of using net-proton as the approximation for the net-baryon distributions and the acceptance dependence for the moments of the protons and antiprotons.

In an early publication from the STAR experiment on the higher moments of net-proton distributions, the selected kinematics of (anti)proton are $|y| < 0.5$ and $0.4 < p_T < 0.8$ GeV/c, where only the Time Projection Chamber (TPC) [81, 82] was used for (anti)protons identification. Interesting hints of a non-monotonic variation of $\kappa\sigma^2$ (or C_4/C_2) was observed [83]. In this paper, we report measurements of the energy dependence of C_n up to fourth order of the net-proton multiplicity distributions from Au+Au collisions with a larger acceptance of $0.4 < p_T < 2.0$ GeV/c [84]. This is achieved by adding the information from STAR’s Time-of-Flight (TOF) detector [85]. We present results from Au+Au collisions at 9 different collision energies, $\sqrt{s_{NN}} = 7.7, 11.5, 14.5, 19.6, 27, 39, 54.4, 62.4$ and 200 GeV.

The paper is organized as follows. In the next section, we discuss the data sets used, event selection criteria, centrality selection procedure, proton identification method, measurement of raw cumulants of the net-proton distributions, corrections for the effects of centrality bin width (CBW) and efficiency, and estimation of statistical and systematic uncertainties on the measurements. In section III, we present the results of cumulants and their ratios for net protons, protons and antiprotons in Au+Au collisions

as a function of collision energy ($\sqrt{s_{NN}}$), centrality, transverse momentum (p_T) acceptance and rapidity acceptance (Δy). In addition, we present the extracted various order integrated correlation functions of protons and antiprotons from the measured cumulants. In this section, we also discuss the results from the HRG model and transport model calculations. In section IV, we present the summary. Detailed discussions on the efficiency correction, and the estimation of the statistical uncertainties are presented in Appendices A and B, respectively.

II. EXPERIMENT AND DATA ANALYSIS

A. Data set and event selection

The data presented in the paper were obtained using the Time Projection Chamber (TPC) [81] and the Time-of-Flight detectors (TOF) [85] of the Solenoidal Tracker at RHIC (STAR) [81]. The event-by-event proton (N_p) and antiproton ($N_{\bar{p}}$) multiplicities are measured for Au+Au minimum-bias events at $\sqrt{s_{NN}} = 7.7, 11.5, 14.5, 19.6, 27, 39, 54.4, 62.4$ and 200 GeV for collisions occurring within a certain Z -position (V_z) range of the collision vertex (given in Table I) from the TPC center along the beam line. These data sets were taken with a minimum-bias trigger, which was defined using a coincidence of hits in the zero degree calorimeters (ZDCs) [86], vertex position detectors (VPDs) [87], and/or beam-beam counters (BBCs) [88]. The range of $|V_z|$ is chosen to optimize the event statistics and uniformity of the response of the detectors used in the analysis.

In order to reject background events which involve interactions with the beam pipe, the transverse radius of the event vertex is required to be within 2 cm (1 cm for 14.5 GeV) of the center of STAR [8]. We use two methods to determine the V_z : one from a fast scintillator-based vertex position detector, and the other from the most probable point of common origin of the tracks, which are reconstructed from the hits measured in the TPC. To remove pile-up events at energies above 27 GeV, we require the V_z difference between the two methods to be within 3 cm. Further, a detailed study of the TPC tracks as a function of the TOF matched tracks with valid TOF information is carried out and outlier events are rejected. To ensure the quality of the data, a run-by-run study of several variables, such as the total number of uncorrected charged particles measured in the TPC, average transverse momentum ($\langle p_T \rangle$) in an event, mean pseudorapidity (η) and azimuthal angle (ϕ) in an event, is carried out. Outlier runs beyond $\pm 3\sigma$, where σ corresponds to the standard deviation of run-by-run distributions of a variable, are not included in the current analysis. In addition, the distance of closest approach (DCA) of the charged-particle track from the primary vertex, especially the signed transverse DCA (DCA_{xy}) are studied to remove bad events (The signed transverse DCA refers to the DCA with respect to the primary vertex in the

TABLE I. Total number of events for Au+Au collisions analysed for various collision energies ($\sqrt{s_{NN}}$) obtained after all of the event selection criteria are applied. The Z -vertex (V_z) range, the chemical freeze-out temperature (T_{ch}) and baryon chemical potential (μ_B) for 0-5% Au+Au collisions [8] are also given.

| $\sqrt{s_{NN}}$ (GeV) | No. of events (million) | $ V_z $ (cm) | T_{ch} (MeV) | μ_B (MeV) |
|-----------------------|-------------------------|--------------|----------------|---------------|
| 200 | 238 | 30 | 164.3 | 28 |
| 62.4 | 47 | 30 | 160.3 | 70 |
| 54.4 | 550 | 30 | 160.0 | 83 |
| 39 | 86 | 30 | 156.4 | 103 |
| 27 | 30 | 30 | 155.0 | 144 |
| 19.6 | 15 | 30 | 153.9 | 188 |
| 14.5 | 20 | 30 | 151.6 | 264 |
| 11.5 | 6.6 | 30 | 149.4 | 287 |
| 7.7 | 3 | 40 | 144.3 | 398 |

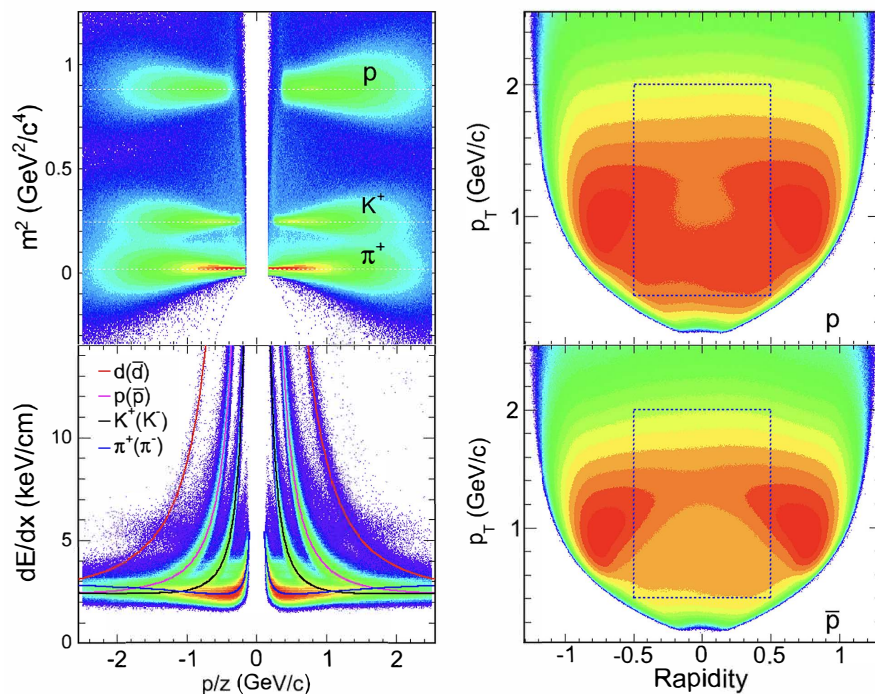


FIG. 1. (Color online) Top left panel: The mass squared (m^2) versus rigidity for charged tracks in Au+Au collisions at $\sqrt{s_{NN}} = 39$ GeV. The rigidity is defined as momentum/ z , where z is the dimensionless ratio of particle charge to the electron charge magnitude. Bottom left panel: The specific ionization energy loss (dE/dx) as a function of rigidity measured in the TPC for the same data set. Also shown as solid lines are the theoretical expectations for each particle species. Right panels: Rapidity (y) versus transverse momentum (p_T). The color reflects the relative yields of protons (top) and antiprotons (bottom) using the TPC PID for Au+Au collisions at $\sqrt{s_{NN}} = 39$ GeV. The dashed boxes represent the acceptance used in the current analysis. Two blobs at large rapidities are contaminated by particles other than (anti)protons. This contamination is rejected in later steps of the analysis.

TABLE II. Proton and antiproton track selection criteria at all energies. The N_{Fit} and $N_{HitPoss}$ represent the number of hits used in track fitting and the maximum number of possible hits in the TPC.

| $ y $ | p_T (GeV/c) | DCA (cm) | N_{Fit} | $N_{Fit}/N_{HitPoss}$ | No. of dE/dx points |
|---------|---------------|----------|-----------|-----------------------|-----------------------|
| < 0.5 | 0.4-2.0 | < 1 | > 20 | > 0.52 | > 5 |

transverse plane. Its sign is the sign of the vector product of the DCA vector and the track momentum). These classes of bad events are primarily related to unstable beam conditions during the data taking and inaccurate space-charge calibration of the TPC.

Table I gives the total number of minimum-bias events analyzed for each $\sqrt{s_{\text{NN}}}$ and the corresponding chemical freeze-out temperature (T_{ch}) and baryon chemical potential (μ_{B}) values for central 0-5% Au+Au collisions. The beam energy values in the BES program are chosen so that the difference in μ_{B} values is not larger than 100 MeV between adjacent collision energies.

B. Track selection, particle identification and acceptance

The proton and antiproton track selection criteria for all the $\sqrt{s_{\text{NN}}}$ are presented in Table II. In order to suppress contamination by tracks from secondary vertices, a requirement of less than 1 cm is placed on DCA between each track and the event vertex. Tracks are required to have at least 20 points used in track fitting out of a maximum of 45 possible hits in the TPC. To prevent multiple counting of split tracks, more than 52% of the maximum-possible fit points are required. A condition is also placed on the number of points (> 5) used to extract the energy loss (dE/dx) values, which is used to identify the (anti)protons from the charged particles detected in the TPC. The results presented here are within kinematics $|y| < 0.5$ and $0.4 < p_{\text{T}} < 2.0$ GeV/ c .

Particle identification (PID) is carried out using the TPC and TOF by measuring the dE/dx and time of flight, respectively. Figure 1 (left top panel) shows a typical plot of the square of the mass (m^2) associated with a track measured in the TPC as a function of rigidity (defined as momentum/ z , where z is the dimensionless ratio of particle charge to the electron charge magnitude) for Au+Au collisions at $\sqrt{s_{\text{NN}}} = 39$ GeV. The m^2 is given by:

$$m^2 = p^2 \left(\frac{c^2 t^2}{L^2} - 1 \right), \quad (1)$$

where p , t , L , and c are the momentum, time-of-flight of the particle, path length, and speed of light, respectively.

Protons and antiprotons can be identified by selecting charged tracks for which $0.6 < m^2 < 1.2$ GeV²/ c^4 .

Figure 1 (left bottom panel) shows the dE/dx of measured charged particles plotted as a function of the rigidity. The measured values of dE/dx are compared to the expected theoretical values [90] (shown as solid lines in Fig. 1) to select the proton and antiproton tracks. A quantity called $N_{\sigma,p}$ for charged tracks in the TPC is defined as:

$$N_{\sigma,p} = (1/\sigma_R) \ln \left(\frac{\langle dE/dx \rangle}{\langle dE/dx \rangle_p^{\text{th}}} \right), \quad (2)$$

where $\langle dE/dx \rangle$ is the truncated mean value of the track energy loss measured in the TPC, $\langle dE/dx \rangle_p^{\text{th}}$ is the corresponding theoretical value for proton (or antiproton) in the STAR TPC [90] and σ_R is the dE/dx resolution which is momentum-dependent and of the order of 7.5% for the momentum range of this analysis. Assuming that the $N_{\sigma,p}$ distribution in a given momentum range is Gaussian, it should peak at zero for proton tracks and the values represent the deviation from the theoretical values for proton tracks in terms of standard deviations (σ_R). Momentum-dependent selection criteria are used for TPC tracks to select protons or antiprotons. For $0.4 < p_{\text{T}} < 0.8$ GeV/ c and momentum (p) less than 1 GeV/ c , $|N_{\sigma,p}| < 2.0$ is chosen and for $0.8 < p_{\text{T}} < 2.0$ GeV/ c and momentum (p) less than 3 GeV/ c , in addition to $|N_{\sigma,p}| < 2.0$, the track is required to have $0.6 < m^2 < 1.2$ GeV²/ c^4 from TOF. The purity is estimated by referring to the $N_{\sigma,p}$ distributions from the TPC in various p_{T} ranges (within 0.4 to 0.8 GeV/ c) to estimate the contamination from other hadrons within the PID selection criteria. For the higher p_{T} range, the m^2 distributions from the TOF are studied after applying the $N_{\sigma,p}$ criteria and the contamination from other hadrons within the PID selection criteria is estimated. The purity of the proton and antiproton samples are better than 97% for all the p_{T} ranges and $\sqrt{s_{\text{NN}}}$ studied.

Figure 1 (right panels) shows the p_{T} versus y for protons and antiprotons selected by the TPC with $|N_{\sigma,p}| < 2.0$ in Au+Au collisions at $\sqrt{s_{\text{NN}}} = 39$ GeV. The acceptance is uniform in y - p_{T} and is the same for other $\sqrt{s_{\text{NN}}}$ studied here. This is a major advantage of collider-based experiments over fixed-target experiments. The boxes show the acceptance criteria used in this analysis. The addition of the TOF extends the PID capabilities to higher p_{T} , thereby allowing for the detection of $\sim 80\%$ of the total protons per unit rapidity (or antiprotons per unit rapidity) produced in the collisions at midrapidity. This is a significant improvement compared to the previous analysis reported in Ref. [83]. The uniform and large acceptance at midrapidity in y , p_{T} and ϕ allows STAR to measure and compare the cumulants in Au+Au collisions at $\sqrt{s_{\text{NN}}} = 7.7$ to 200 GeV.

C. Centrality selection

Centrality selection plays a crucial role in the fluctuation analysis. There are two effects related to the centrality selection which need to be addressed. These are (a) the self-correlation [91, 92] and (b) centrality resolution/fluctuations effects [91–95].

One of the main self-correlation effects arises when particles used for the fluctuation analysis are also used for the centrality definition. This can be significantly reduced by removing the particles used in the fluctuation analysis from the centrality definition. Hence, we exclude protons and antiprotons from charged particles for the centrality selection.

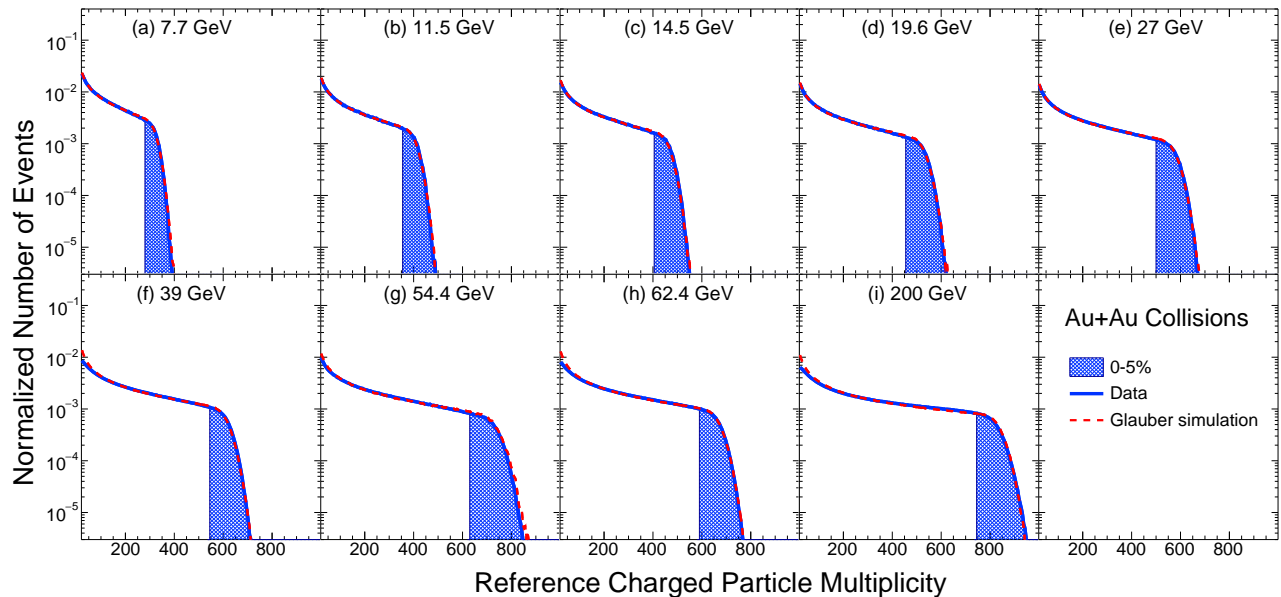


FIG. 2. (Color online) The uncorrected reference charged particle multiplicity (N_{ch}) distributions within pseudorapidity $|\eta| < 1$ by excluding protons and antiprotons in Au+Au collisions at $\sqrt{s_{\text{NN}}} = 7.7 - 200$ GeV. These distributions are used for centrality determination. The shaded region at each $\sqrt{s_{\text{NN}}}$ corresponds to 0-5% central collisions. The dashed line corresponds to Monte Carlo Glauber model simulations [89].

423 The centrality resolution effect arises due to the fact
 424 that the number of participant nucleons and particle multi-
 425 plicities fluctuate even if the impact parameter is fixed.
 426 Through a model simulation it has been shown that the
 427 larger the η acceptance used for centrality selection,
 428 the closer are the values of the cumulants to the actual
 429 values [91]. This is because the centrality resolution is im-
 430 proved by increasing the number of particles for the cen-
 431 trality definition with wider acceptance. Therefore, to
 432 suppress the effect of centrality resolution, one should
 433 use the maximum available acceptance of charged parti-
 434 cles for centrality selection. In addition, it may be men-
 435 tioned that the choice of centrality definition also affects
 436 the way volume fluctuations (discussed later) contribute
 437 to the measurements.

438 These are the driving considerations for the central-
 439 ity selection for net-proton studies presented in this pa-
 440 per and are discussed below. The basic strategy is to
 441 maximize the acceptance window for the centrality de-
 442 termination as allowed by the detectors, and to not use
 443 protons and antiprotons for the centrality selection. In
 444 addition, the centrality definition method given below is
 445 determined after several optimization studies using data
 446 and models. These studies were carried out by varying
 447 the acceptances in η and charged particle types in or-
 448 der to understand the effect of the choice of centrality
 449 determination method on the analysis [92]. The effect
 450 of self-correlation potentially arising due to the decay of
 451 heavier hadrons into protons and antiprotons and other
 452 charged particles has been verified to be negligible from
 453 a study using standard heavy-ion collision event genera-
 454 tors, HIJING [96] and UrQMD [92, 97].

TABLE III. The uncorrected number of charged particles other than protons and antiprotons (N_{ch}) within the pseudorapidity $|\eta| < 1.0$ used for the centrality selection for various collision centralities expressed in % centrality in Au+Au collisions at $\sqrt{s_{\text{NN}}} = 7.7 - 200$ GeV.

| % centrality | N_{ch} values at different $\sqrt{s_{\text{NN}}}$ (GeV) | | | | | | | | |
|--------------|--|------|------|-----|-----|------|------|------|-----|
| | 200 | 62.4 | 54.4 | 39 | 27 | 19.6 | 14.5 | 11.5 | 7.7 |
| 0-5 | 725 | 571 | 621 | 522 | 490 | 448 | 393 | 343 | 270 |
| 5-10 | 618 | 482 | 516 | 439 | 412 | 376 | 330 | 287 | 225 |
| 10-20 | 440 | 338 | 354 | 308 | 289 | 263 | 231 | 199 | 155 |
| 20-30 | 301 | 230 | 237 | 209 | 196 | 178 | 157 | 134 | 105 |
| 30-40 | 196 | 149 | 151 | 136 | 127 | 116 | 103 | 87 | 68 |
| 40-50 | 120 | 91 | 90 | 83 | 78 | 71 | 63 | 53 | 41 |
| 50-60 | 67 | 51 | 50 | 47 | 44 | 40 | 36 | 30 | 23 |
| 60-70 | 34 | 26 | 24 | 24 | 22 | 20 | 19 | 15 | 11 |
| 70-80 | 16 | 12 | 10 | 11 | 10 | 9 | 13 | 7 | 5 |

In order to suppress the self-correlation, centrality resolution and volume fluctuation effects with the available STAR detectors, a new centrality measure is defined, and is different from other analyses reported by STAR [8]. The centrality is determined from the uncorrected charged particle multiplicity within pseudorapidity $|\eta| < 1$ (N_{ch}) after excluding the protons and antiprotons. Strict particle identification criteria are used to remove the proton and antiproton contributions. Charged tracks with $N_{\sigma,p} < -3$ are used and for those tracks which have TOF information an additional criterion, $m^2 < 0.4 \text{ GeV}^2/c^4$ is applied. The resultant distribution of charged particles is corrected for luminosity and

TABLE IV. The average number of participant nucleons ($\langle N_{\text{part}} \rangle$) for various collision centralities in Au+Au collisions at $\sqrt{s_{\text{NN}}} = 7.7 - 200$ GeV from a Monte Carlo Glauber Model. The numbers in parentheses are systematic uncertainties.

| % centrality | $\langle N_{\text{part}} \rangle$ values at different $\sqrt{s_{\text{NN}}}$ (GeV) | | | | | | | | | |
|--------------|--|---------|----------|----------|----------|----------|----------|----------|----------|--|
| | 200 | 62.4 | 54.4 | 39 | 27 | 19.6 | 14.5 | 11.5 | 7.7 | |
| 0-5 | 351 (2) | 347 (3) | 346 (2) | 342(2) | 343 (2) | 338 (2) | 340(2) | 338 (2) | 337 (2) | |
| 5-10 | 299 (4) | 294 (4) | 292 (6) | 294 (6) | 299 (6) | 289 (6) | 289 (6) | 291 (6) | 290 (6) | |
| 10-20 | 234 (5) | 230 (5) | 228 (8) | 230 (9) | 234 (9) | 225 (9) | 225 (8) | 226 (8) | 226 (8) | |
| 20-30 | 168 (5) | 164 (5) | 161 (10) | 162 (10) | 166 (11) | 158 (10) | 159 (9) | 160 (9) | 160 (10) | |
| 30-40 | 117 (5) | 114 (5) | 111 (11) | 111 (11) | 114 (11) | 108 (11) | 109 (11) | 110 (11) | 110 (11) | |
| 40-50 | 78 (5) | 76 (5) | 73 (10) | 74 (10) | 75 (10) | 71 (10) | 72 (10) | 73 (10) | 72 (10) | |
| 50-60 | 49 (5) | 48 (5) | 45 (9) | 46 (9) | 47 (9) | 44 (9) | 45 (9) | 45 (9) | 45 (9) | |
| 60-70 | 29 (4) | 28 (4) | 26 (7) | 26 (7) | 27 (8) | 26 (7) | 26 (7) | 26 (7) | 26 (7) | |
| 70-80 | 16 (3) | 15 (2) | 13 (5) | 14 (5) | 14 (6) | 14 (5) | 14 (6) | 14 (6) | 14 (4) | |

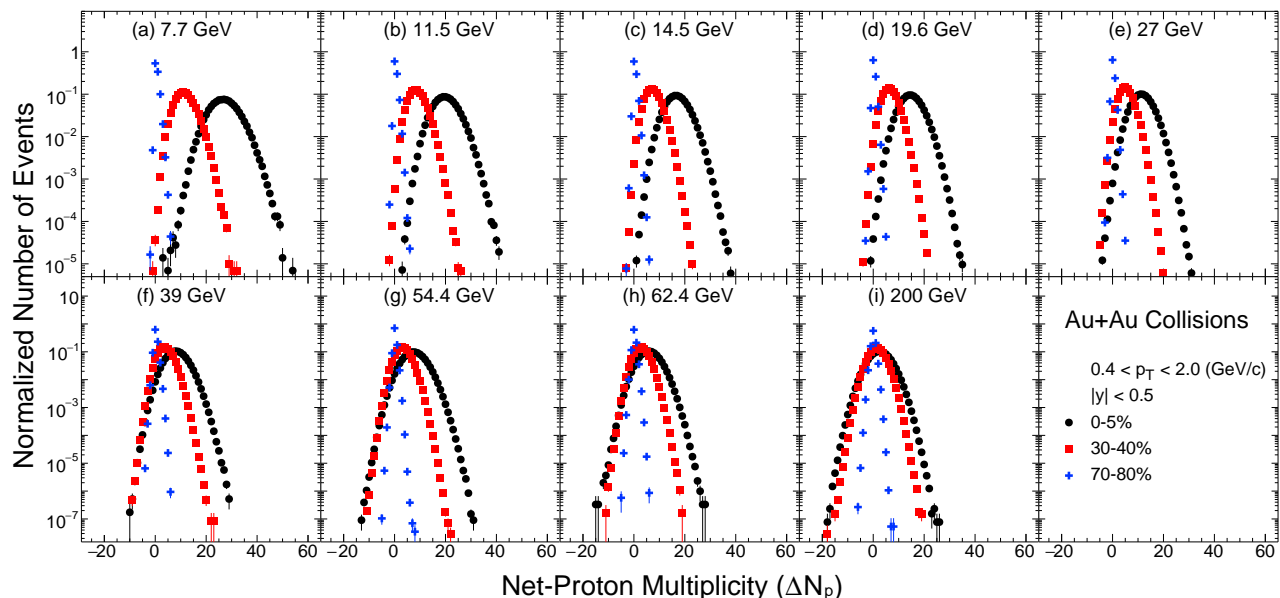


FIG. 3. (Color online) Net-proton multiplicity (ΔN_p) distributions in Au+Au collisions at various $\sqrt{s_{\text{NN}}}$ for 0-5%, 30-40% and 70-80% collision centralities at midrapidity. The statistical errors are small and within the symbol size. The distributions are not corrected neither for the finite-centrality-width effect nor for the reconstruction efficiencies of protons and antiprotons.

468 V_z dependence at each $\sqrt{s_{\text{NN}}}$. The corrected charged⁴⁸³
 469 particle distribution is then fit to a Monte Carlo Glauber⁴⁸⁴
 470 Model [37, 89] to define the centrality classes in the ex-
 471 periment (the percentage cross section and the associated
 472 cuts on the charged-particle multiplicity). In the fitting⁴⁸⁵
 473 process, a multiplicity-dependent efficiency has been ap-⁴⁸⁶
 474 plied [37].

475 Figure 2 shows the reference charged particle multi-⁴⁹¹
 476 plicity distributions after excluding protons and antipro-⁴⁹²
 477 tons used for centrality determination for all of the $\sqrt{s_{\text{NN}}}$ ⁴⁹³
 478 studied here. The lower boundaries of each centrality⁴⁹⁴
 479 class based on N_{ch} are given in Table III. Table IV gives⁴⁹⁵
 480 the average number of participant nucleons ($\langle N_{\text{part}} \rangle$) for⁴⁹⁶
 481 various collision centralities for $\sqrt{s_{\text{NN}}} = 7.7 - 200$ GeV⁴⁹⁷
 482 obtained from a Monte Carlo Glauber model simulation.⁴⁹⁸

D. Uncorrected net-proton multiplicity distributions

Figure 3 shows the event-by-event net-proton multi-
 plicity (ΔN_p) distributions from Au+Au collisions at
 $\sqrt{s_{\text{NN}}} = 7.7 - 200$ GeV for 0-5%, 30-40% and 70-80% col-
 lision centralities. The ΔN_p distribution is obtained by
 counting the number of protons and antiprotons within the
 y - p_{T} acceptance on an event-by-event basis for a
 given collision centrality and $\sqrt{s_{\text{NN}}}$. The distributions
 presented in Fig. 3 are not corrected for the efficiency
 and acceptance effects. In general, the shape of the ΔN_p
 distributions is broader, more symmetric and closer to
 Gaussian, for central collisions than for peripheral colli-
 sions. The shape of the distributions also changes with
 $\sqrt{s_{\text{NN}}}$. Cumulants (C_n) up to the fourth order are ob-
 tained from these distributions for each collision central-

ity and $\sqrt{s_{\text{NN}}}$.

E. Definition of cumulants and integrated correlation functions

In this subsection, we give the definition of the cumulants used in this paper. Let N represent any entry in the data sample, its deviation from its mean value ($\langle N \rangle$, referred to as the 1st moment) is then given by $\delta N = N - \langle N \rangle$. Any r^{th} -order central moment is defined as:

$$\mu_r = \langle (\delta N)^r \rangle. \quad (3)$$

The cumulants of a given data sample could be written in terms of moments as follows:

$$\begin{aligned} C_1 &= \langle N \rangle, \\ C_2 &= \langle (\delta N)^2 \rangle = \mu_2, \\ C_3 &= \langle (\delta N)^3 \rangle = \mu_3, \\ C_4 &= \langle (\delta N)^4 \rangle - 3\langle (\delta N)^2 \rangle^2 \\ &= \mu_4 - 3\mu_2^2, \\ C_n (n > 3) &= \mu_n - \sum_{m=2}^{n-2} \binom{n-1}{m-1} C_m \mu_{n-m}. \end{aligned} \quad (4)$$

The relations between cumulants and various moments are given as:

$$M = C_1, \quad \sigma^2 = C_2, \quad S = \frac{C_3}{(C_2)^{3/2}}, \quad \kappa = \frac{C_4}{(C_2)^2}. \quad (5)$$

where M , σ^2 , S and κ are mean, variance, skewness and kurtosis, respectively. The products $\kappa\sigma^2$ and $S\sigma$ can be expressed in terms of the ratio of cumulants as:

$$\sigma^2/M = \frac{C_2}{C_1}, \quad S\sigma = \frac{C_3}{C_2}, \quad \kappa\sigma^2 = \frac{C_4}{C_2}. \quad (6)$$

With the above definition, we can calculate various order cumulants (moments) and cumulant ratios (moment products) from the measured event-by-event net-proton, proton and antiproton distributions for each centrality at a given $\sqrt{s_{\text{NN}}}$. For two independent variables X and Y , the cumulants of the probability distributions of their sum ($X + Y$), are just the addition of cumulants of the individual distributions for X and Y *i.e.* $C_{n,X+Y} = C_{n,X} + C_{n,Y}$ for n^{th} -order cumulant. For a distribution of difference between X and Y , the cumulants are $C_{n,X-Y} = C_{n,X} + (-1)^n C_{n,Y}$, where even-order cumulants are the addition of the individual cumulants, while the odd-order cumulants are obtained by taking their difference. If the protons and antiprotons are distributed as independent Poissonian distributions, the various order cumulants of net-proton, proton and antiproton distributions can be expressed as:

$$\begin{aligned} C_{n,p} &= C_{1,p}, \quad C_{n,\bar{p}} = C_{1,\bar{p}}, \\ C_{n,p-\bar{p}} &= C_{1,p} + (-1)^n C_{1,\bar{p}} \end{aligned} \quad (7)$$

where the net-proton multiplicity distributions obey the Skellam distribution and the Poisson baseline/expectation values of the net-proton, proton and antiproton cumulant ratios are:

$$\begin{aligned} (\sigma^2/M)_{p,\bar{p}} &= (S\sigma)_{p,\bar{p}} = (\kappa\sigma^2)_{p,\bar{p}} = 1, \\ (\sigma^2/M)_{p-\bar{p}} &= \frac{1}{(S\sigma)_{p-\bar{p}}} = \frac{C_{1,p} + C_{1,\bar{p}}}{C_{1,p} - C_{1,\bar{p}}}, \\ (\kappa\sigma^2)_{p-\bar{p}} &= 1 \end{aligned}$$

where $C_{1,p}$ and $C_{1,\bar{p}}$ are the mean values of proton and antiproton, respectively.

On the other hand, it is expected that close to the CP, the three- and four-particle correlations are dominant relative to two-particle correlations [46]. The various orders integrated correlation functions of proton and antiproton (κ_n , also known as factorial cumulants) are related to the corresponding proton and antiproton cumulants (C_n) through the following relations [98–100]:

$$\begin{aligned} \kappa_1 &= C_1 = \langle N \rangle, \\ \kappa_2 &= -C_1 + C_2, \\ \kappa_3 &= 2C_1 - 3C_2 + C_3, \\ \kappa_4 &= -6C_1 + 11C_2 - 6C_3 + C_4, \\ C_2 &= \kappa_2 + \kappa_1, \\ C_3 &= \kappa_3 + 3\kappa_2 + \kappa_1, \\ C_4 &= \kappa_4 + 6\kappa_3 + 7\kappa_2 + \kappa_1, \end{aligned} \quad (7)$$

where C_1 and κ_1 represent the mean values for protons or antiprotons. For proton and antiproton cumulant ratios C_2/C_1 , C_3/C_2 and C_4/C_2 , they can be expressed in terms of corresponding normalized correlation functions κ_n/κ_1 ($n > 1$) as:

$$\frac{C_2}{C_1} = \frac{\kappa_2}{\kappa_1} + 1, \quad (8)$$

$$\frac{C_3}{C_2} = \frac{\kappa_3/\kappa_1 - 2}{\kappa_2/\kappa_1 + 1} + 3, \quad (9)$$

$$\frac{C_4}{C_2} = \frac{\kappa_4/\kappa_1 + 6\kappa_3/\kappa_1 - 6}{\kappa_2/\kappa_1 + 1} + 7, \quad (10)$$

The higher-order integrated correlation functions κ_n ($n > 1$) are equal to zero when the distributions are Poisson. Thus, κ_n can be used to quantify the deviations from the Poisson distributions in terms of n -particle correlations. For simplicity, from here on, we refer to the κ_n as correlation functions instead of integrated correlation functions.

In the following subsections, we discuss corrections that are related to collision centrality bin width (Sec. F) and detection efficiency (Sec. G). This is followed by the estimation of statistical and systematic uncertainties in sections H and I, respectively.

F. Centrality bin width correction

The data are presented in this paper as a function of various collision centrality classes for 0-5%, 5-10%, 10-

20%, 20-30%, 30-40%, 40-50%, 50-60%, 60-70% and 70-80%. The finite size of centrality bins implies that the average number of protons and antiprotons varies within a centrality class. This variation has to be accounted for while calculating the cumulants in a broad centrality class. In addition, it is known that calculating cumulants in such broad centrality bins leads to a strong enhancement of cumulants and cumulant ratios due to initial volume fluctuations [91, 101].

A Centrality Bin Width Correction (CBWC) is the procedure used to take care of the measurements in a wide centrality bin and is based on weighting the cumulants measured at each multiplicity bin by the number of events in the bin [91, 92, 101]. This procedure is mathematically expressed in the equation below:

$$C_n = \frac{\sum_r n_r C_n^r}{\sum_r n_r} = \sum_r \omega_r C_n^r, \quad (11)$$

where the n_r is the number of events at the r^{th} multiplicity bin for the centrality determination, the C_n^r represents the n^{th} -order cumulant of particle number distributions at r^{th} multiplicity. The corresponding weight for the r^{th} multiplicity bin is $\omega_r = n_r / \sum_r n_r$.

Figure 4 shows the C_n up to the fourth order as a function of $\langle N_{\text{part}} \rangle$ for three different collision energies: $\sqrt{s_{\text{NN}}} = 7.7, 19.6$ and 62.4 GeV. For each C_n case, four different results are shown. One of them is the CBWC result for 9 collision centrality bins, which correspond to 0-5%, 5-10%, 10-20%, 20-30%, ..., 70-80%. For comparison, cumulants are also calculated for the other three cases, which are 10%, 5% and 2.5% centrality bin width without CBWC. The higher-order cumulant results with 10% centrality bins are found to have significant deviations compared to those with 5% and 2.5% centrality bins without CBWC. This finding means that it is important to correct for the CBW effect, as one normally expects that, irrespective of the centrality bin width, the cumulant values should exhibit the same dependence on $\langle N_{\text{part}} \rangle$. It is found that the results get closer to CBWC results with narrower centrality bins and the results with 2.5% centrality bins almost overlap with CBWC results which indicates that the CBWC can effectively suppress the effect of the volume fluctuations on cumulants (up to the fourth order) within a finite centrality bin width.

A different approach, volume fluctuation correction (VFC) method [102, 103], which assumes independent production of protons, has been also applied at $\sqrt{s_{\text{NN}}} = 7.7, 19.6$ and 62.4 GeV for 0-5% Au+Au central collisions. The correction factors are determined by the Glauber model [103]. Figure 5 shows the comparison between the results based on CBWC and VFC methods. As can be seen from the plot, for the 0-5% central collisions the results of CBWC and VFC are found to be consistent within statistical uncertainties. However, follow-up UrQMD model studies reported in Ref. [94], indicate that the VFC method (as discussed in Ref. [102]) does not

work, as the independent particle production model assumed in the VFC is expected to be broken. Therefore, we follow the data-driven method, CBWC, in this paper.

G. Efficiency correction

Figure 6 shows the efficiency-uncorrected C_n for proton, antiproton and net-proton multiplicity distributions in Au+Au collisions at $\sqrt{s_{\text{NN}}} = 7.7 - 200$ GeV as a function of $\langle N_{\text{part}} \rangle$. This section discusses the method of efficiency correction. One such method is called the binomial-model-based method [80, 100, 104–106] and another is the unfolding method [107, 108]. The cumulants presented in the subsequent sections are corrected for efficiency and acceptance effects related to proton and antiproton reconstruction, unless specified otherwise.

1. Binomial model method

The binomial-based method involves two steps. First we obtain the efficiency of proton and antiproton reconstruction in the STAR detector and then correct the cumulants for efficiency and acceptance effects using analytic expressions. The former uses the embedding process and the latter invokes binomial model assumptions for the detector response function for the efficiencies. One can find more details in Appendix A.

The detector acceptance and the efficiency of reconstructing proton and antiproton tracks are determined together by embedding Monte Carlo (MC) tracks, simulated using the GEANT [109] model of the STAR detector response, into real events at the raw data level. One important requirement is the matching of the distributions of reconstructed embedded tracks and real data tracks for quantities reflecting track quality and those used for track selection [8]. The ratio of the distribution of reconstructed to embedded Monte Carlo tracks as a function of p_T gives the efficiency \times acceptance correction factor ($\varepsilon_{\text{TPC}}(p_T)$) for the rapidity interval studied. We refer to this factor as simply efficiency.

The current analysis makes use of both the TPC and the TOF detectors. While the TPC identifies low p_T ($0.4 < p_T < 0.8$ GeV/ c) protons and antiprotons with high purity, the TOF gives better particle identification than the TPC in the higher p_T range ($0.8 < p_T < 2.0$ GeV/ c). However, not all TPC tracks have valid TOF information due to the limited TOF acceptance and the mismatching of the TPC tracks to TOF hits. This extra efficiency is called the TOF-matching efficiency ($\varepsilon_{\text{TOF}}(p_T)$). The TOF-matching efficiency is particle-species-dependent and can be obtained using a data-driven technique, which is defined as the ratio of the number of (anti)proton tracks detected in the TOF to the total number of (anti)proton tracks in the TPC within the same acceptance [8]. Thus, the final average (anti)proton efficiency within a certain p_T range can be calculated as:

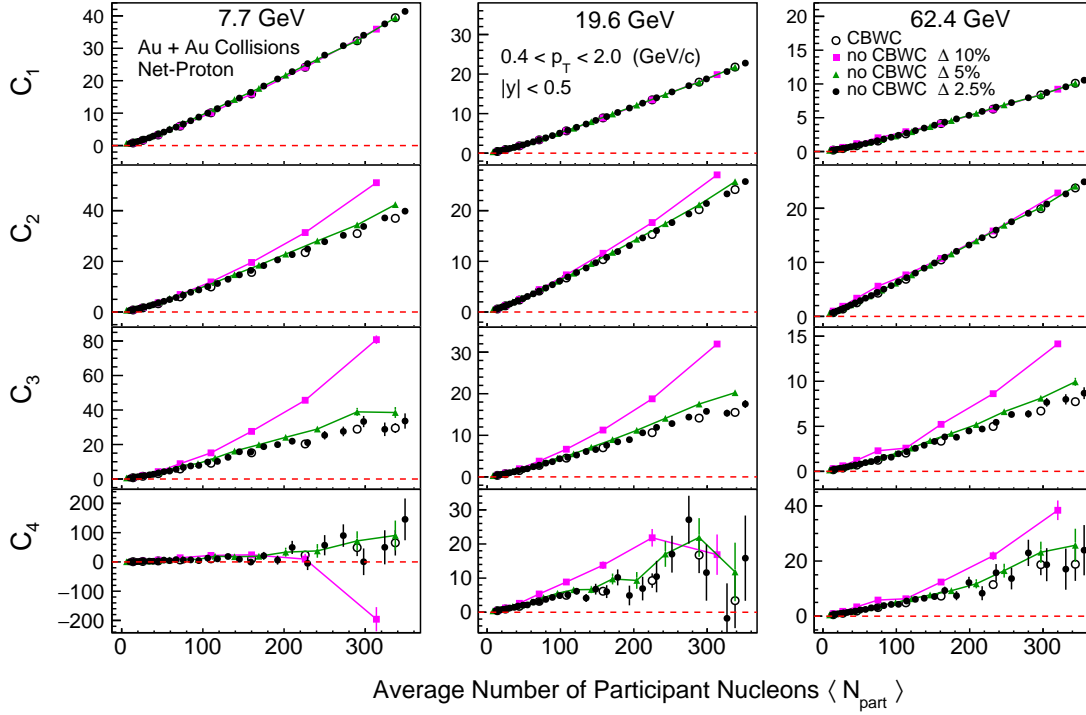


FIG. 4. (Color online) C_n of net-proton distributions in Au+Au collisions at $\sqrt{s_{NN}} = 7.7, 19.6$ and 62.4 GeV as a function of $\langle N_{\text{part}} \rangle$. The results are shown for 10%, 5% and 2.5% centrality bins without CBWC and for 9 centrality bins (0-5%, 5-10%, 10-20%,..., 70-80%) with CBWC. The bars are the statistical uncertainties.

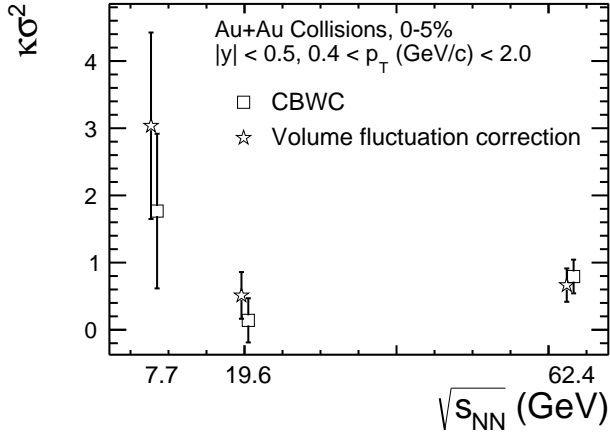


FIG. 5. (Color online) $\kappa\sigma^2$ as a function of collision energy for Au+Au collisions for 0-5% centrality. The data has been corrected for volume fluctuation effects using CBWC, a data driven approach, and a model-dependent volume fluctuation correction method. The bars are the statistical uncertainties.

671 where the p_T -dependent efficiency, $\varepsilon(p_T)$, is defined as
 672 $\varepsilon(p_T) = \varepsilon_{\text{TPC}}(p_T)$ for $0.4 < p_T < 0.8$ GeV/c and $\varepsilon(p_T) =$
 673 $\varepsilon_{\text{TPC}}(p_T) \times \varepsilon_{\text{TOF}}(p_T)$ for $0.8 < p_T < 2.0$ GeV/c. The
 674 function $f(p_T)$ is the efficiency-corrected p_T spectrum
 675 for (anti)protons [8].

676 Figure 7 shows the average efficiency ($\langle \varepsilon \rangle$) for protons
 677 and antiprotons at midrapidity ($|y| < 0.5$) as a function
 678 of collision centrality ($\langle N_{\text{part}} \rangle$). For $0.4 < p_T <$
 679 0.8 GeV/c the efficiency is only from the TPC and for
 680 $0.8 < p_T < 2.0$ GeV/c it is the product of efficiencies
 681 from the TPC and TOF. In Fig. 7, only statistical uncer-
 682 tainties are presented and a $\pm 5\%$ systematic uncertainty
 683 associated with determining the efficiency is considered
 684 in the analysis.

2. Unfolding method

686 In this section we discuss the effect of efficiency cor-
 687 rection on the C_n measurement if the assumption of
 688 binomial detector efficiency response breaks down due
 689 to some of the reasons given in Refs. [110, 111]. The
 690 technique is based on unfolding of the detector re-
 691 sponse [107, 108]. The response function is obtained
 692 by MC simulations carried out in the STAR detector
 693 environment [109]. MC tracks are simulated through
 694 GEANT and embedded in the real data, track recon-
 695 struction is performed as is done in the real experiment.

$$\langle \varepsilon \rangle = \frac{\int_{p_{T_1}}^{p_{T_2}} \varepsilon(p_T) f(p_T) dp_T}{\int_{p_{T_1}}^{p_{T_2}} f(p_T) dp_T}, \quad (12)$$

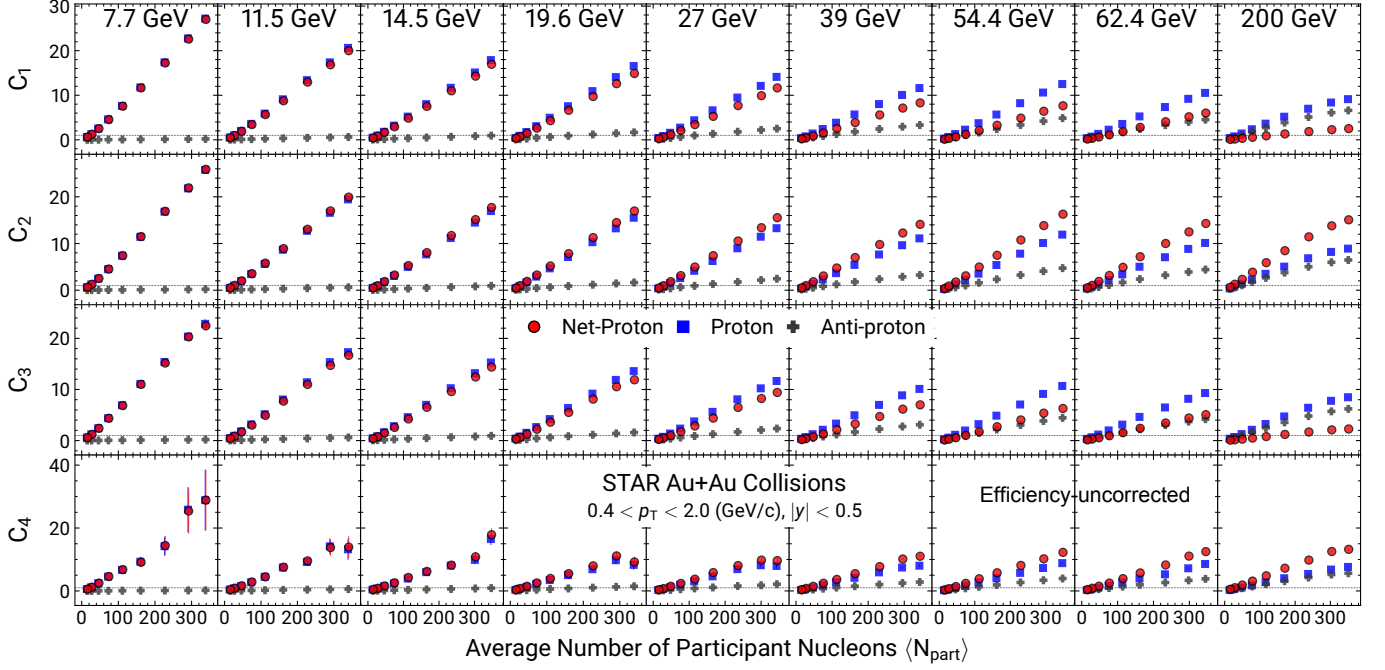


FIG. 6. (Color online) Efficiency-uncorrected C_n of net-proton, proton and antiproton multiplicity distributions in Au+Au collisions at $\sqrt{s_{NN}} = 7.7\text{--}200$ GeV as a function of $\langle N_{\text{part}} \rangle$. The results are CBW-corrected. The bars are the statistical uncertainties.

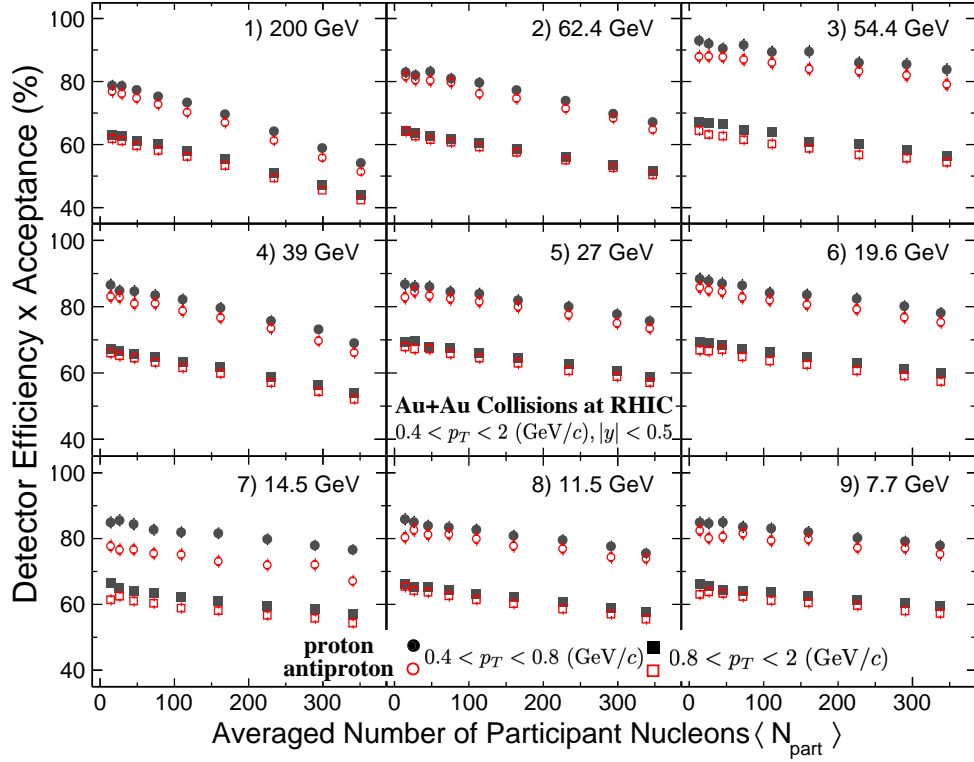


FIG. 7. (Color online) Efficiencies of proton and antiproton as a function of $\langle N_{\text{part}} \rangle$ in Au+Au collisions for various $\sqrt{s_{NN}}$. For the lower p_T range ($0.4 < p_T < 0.8$ GeV/c), only the TPC is used. For the higher p_T range ($0.8 < p_T < 2.0$ GeV/c), both the TPC and TOF are used.

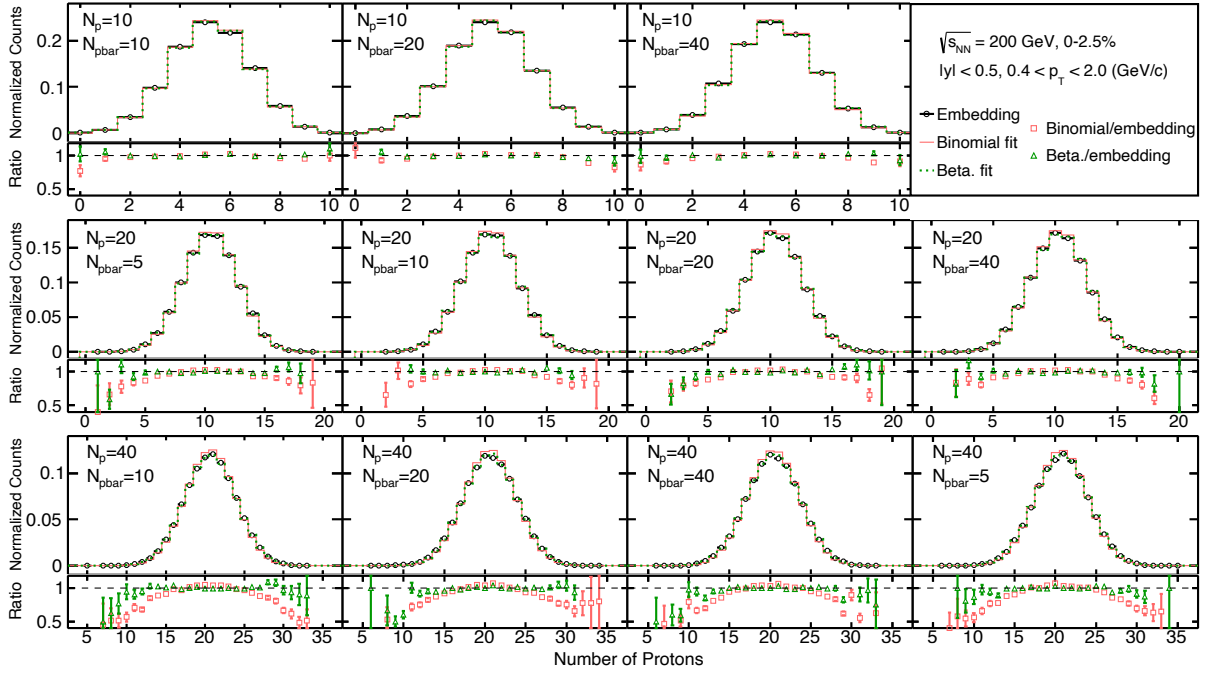


FIG. 8. (Color online) Distributions of reconstructed protons (black circles) from embedding simulations in 200 GeV top 2.5%-central Au+Au collisions. Red lines are fits to the binomial distribution, and green dotted lines represent the fit with the beta-binomial distributions using the α that gives the minimum χ^2/ndf . Each panel presents results for a different combination of the number of embedded protons and antiprotons as labeled in the legend. The ratio of the fits to the embedding data is shown for each panel at the bottom.

696 Many effects can lead to non-binomial detector response
 697 in heavy-ion experiments. One of those effects could be
 698 track merging due to the extreme environment of high
 699 particle multiplicity densities in the detector. Hence, we
 700 have performed the embedding simulations using the real
 701 data for 0-5% Au+Au collisions at $\sqrt{s_{\text{NN}}} = 200$ GeV.
 702 The number of embedded tracks of N_p and $N_{\bar{p}}$ are varied
 703 within $5 \leq N_{p(\bar{p})} \leq 40$. Since we are measuring
 704 the net-proton multiplicity distributions, protons and anti-
 705 protons are embedded simultaneously. We have shown
 706 in Ref. [112] that for the event statistics in the current
 707 analysis, the efficiencies for kaon reconstruction follow
 708 binomial distributions.

709 Figure 8 shows the reconstructed protons from the
 710 embedding data (black circles) of Au+Au collisions
 711 at $\sqrt{s_{\text{NN}}} = 200$ GeV and 0-2.5% collision centrality.
 712 Each panel represents a different number of embedded
 713 (anti)protons. These distributions are fitted by a binomial
 714 distribution (red solid line) at a fixed efficiency ε .
 715 The ratios of the fitted function to the embedding data
 716 are shown in the lower panels. The fitted χ^2/ndf ranges
 717 from 5.2 to 17.8 and the tails of the distributions are
 718 not well described by the binomial distribution for several
 719 combinations of embedded N_p and $N_{\bar{p}}$ tracks. We
 720 find that the embedding data is better described by a
 721 beta-binomial distribution given by:

$$\beta(n : N, a, b) = \int_0^1 dp B(\varepsilon, a, b) B(n; N, \varepsilon), \quad (13)$$

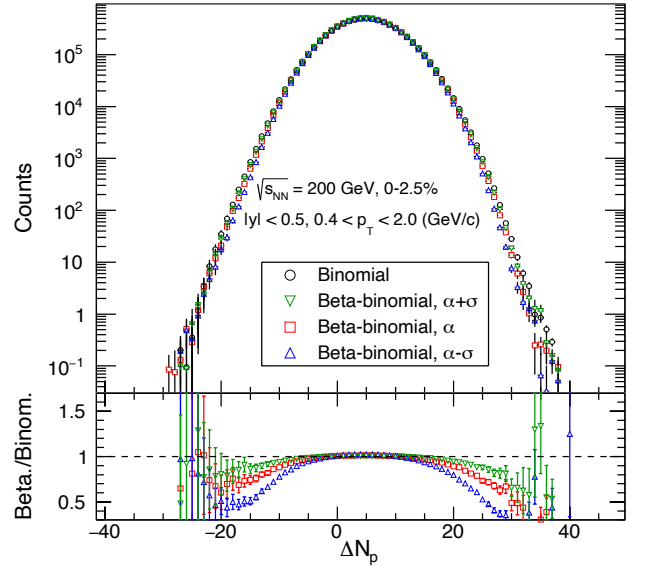


FIG. 9. (Color online) Unfolded net-proton multiplicity distributions for $\sqrt{s_{\text{NN}}} = 200$ GeV Au+Au collisions where the binomial distribution (black circle), beta-binomial distributions with $\alpha + \sigma$ (green triangle), α (red square) and $\alpha - \sigma$ (blue triangle) are utilised in response matrices. Ratios of the beta-binomial unfolded distributions to that from binomial response matrices are shown in the bottom panel.

TABLE V. Net-proton cumulant ratios and their statistical errors for 0-5% central Au+Au collisions at $\sqrt{s_{\text{NN}}} = 200$ GeV, (second column) from the conventional efficiency correction with the binomial detector response, and (third column) from unfolding with the beta-binomial detector response. Systematic errors are also shown for the beta-binomial case. The last column shows the difference between two results normalized by total uncertainty, which is equal to the statistical and systematic uncertainties summed in quadrature.

| Cumulant ratio | binomial \pm statistical error | beta \pm statistical error \pm systematical error | significance |
|----------------|----------------------------------|---|----------------------|
| C_2/C_1 | $1.3 \pm \text{neg.}$ | $1.20 \pm \text{neg.} \pm 0.03$ | 3.1 |
| C_3/C_2 | 0.13 ± 0.01 | $0.13 \pm 0.01 \pm \text{neg.}$ | 4.8×10^{-2} |
| C_4/C_2 | 1.10 ± 0.21 | $0.97 \pm 0.21 \pm 0.08$ | 4.2×10^{-1} |
| C_5/C_1 | 0.10 ± 0.48 | $-0.14 \pm 0.44 \pm 0.11$ | 3.8×10^{-1} |
| C_6/C_2 | -0.45 ± 0.24 | $-0.14 \pm 0.20 \pm 0.07$ | 1.0 |

and with the beta distribution given as:

$$\beta(\varepsilon; a, b) = \varepsilon^a (1 - \varepsilon)^b / B(a, b), \quad (14)$$

where $B(a, b)$ is the beta function. The beta-binomial distribution is given by an urn model. Let us consider N_w white balls and N_b black balls in the urn. One draws a ball from the urn. If it is white (black), return two white (black) balls to the urn. This procedure is repeated with N times, then the resulting distribution of n white balls is given by the beta-binomial distributions as $\beta(n; N, N_w, N_b)$. This is actually equivalent to $\beta(n; N, \alpha, \varepsilon)$, where $N_w = \alpha N$ with $\varepsilon = N_w / (N_w + N_b)$. A smaller α gives a broader distribution than the binomial, while the distribution becomes close to the binomial distribution with a larger value of α .

The beta-binomial distributions are numerically generated with various values of α . These are compared to the embedding data to determine the best fit parameter value of α . The green lines in Fig. 8 show the beta-binomial distribution for the value of α that gives the minimum χ^2/ndf . It is found that $\chi^2/\text{ndf} \approx 1$ for most $(N_p, N_{\bar{p}})$ combinations. With this additional parameter α , it is found that the detector response is better described in the tails by a beta-binomial distribution compared to a binomial distribution.

From the embedding simulations as discussed above, the ε and α are parametrized as a function of N_p and $N_{\bar{p}}$. Using the parametrization, a 4-dimensional response matrix between generated and reconstructed protons and antiprotons is generated with 1 billion events. The limited statistics in the embedding simulations lead to uncertainties on the α values. Therefore, two more response matrices are generated using $\alpha - \sigma$ and $\alpha + \sigma$, where σ is the statistical uncertainty on the α values determined by the embedding simulation. Furthermore, the standard response matrices are also generated with the binomial distribution as a reference using a multiplicity-dependent efficiency. These response matrices are used to correct for the detector effects as a confirmation of this approach by comparing to the binomial correction method described in the previous section. The consistency of the unfolding method has been checked through a detailed simulation and an analytic study.

Figure 9 shows the unfolded net-proton distributions

for 200 GeV Au+Au collisions at 0-2.5% centrality. Results from four assumptions on the detector response are shown, one is the binomial detector response and the other three assume the beta-binomial distributions with different non-binomial α values. The ratios of the beta-binomial unfolded distributions to the binomial unfolded distributions are shown in the bottom panel. The unfolded distributions with beta-binomial response matrices are found to be narrower with a decreasing value of α . Calculations are done for 0-2.5% and 2.5-5.0% centralities separately and averaged to determine the C_n values for the 0-5% centrality. The C_n values and their ratios from data obtained using the binomial model method of efficiency correction and those using the binomial detector response matrix in the unfolding method are consistent. Table V summarizes the cumulant ratios and their errors. Results are also obtained from the unfolding method using the beta-binomial response function with non-binomial parameters in the range $\alpha \pm \sigma$. This range in values of α is used to generate the systematic uncertainties associated with the unfolding method. The deviations of those non-binomial efficiency-corrected results with respect to the conventional efficiency correction with binomial detector response is found to be 3.1σ for C_2/C_1 and less than 1.0σ for C_4/C_2 and for C_3/C_2 . The σ value is the statistical and systematic uncertainties added in quadrature.

These studies have been done for Au+Au collisions for the highest collision energy of $\sqrt{s_{\text{NN}}} = 200$ GeV and top-most 5% centrality. This set of data provides the largest charged-particle-density environment for the detectors, where we expect the maximum non-binomial detector effects. Even in this situation, the differences in the two methods of efficiency correction are at a level of less than one σ . Thus, we conclude that the non-binomial detector effects on higher-order cumulant ratios presented in this work are within the uncertainties quoted for all of the BES-I energies.

H. Statistical uncertainty

The higher-order cumulants are sensitive to the shape of the distribution, and estimating their statistical un-

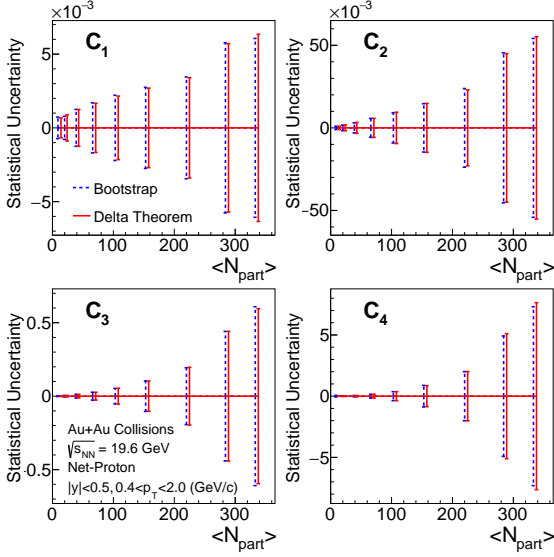


FIG. 10. (Color online) Comparison of the statistical uncertainties on C_n of net-proton distributions in Au+Au collisions at $\sqrt{s_{NN}} = 19.6$ GeV from the delta theorem and bootstrap methods. The results are presented as a function of $\langle N_{\text{part}} \rangle$.

certainty is crucial due to the limited available statistics. It has been shown that among the various methods of obtaining statistical uncertainty on cumulants, the delta theorem method [113] and the bootstrap method [91, 104, 114–116] are the most reliable. Below we briefly discuss the two methods and show that the uncertainty values obtained up to the fourth order cumulant from both methods are consistent.

The delta theorem method gives a concise form of standard error propagation method. This method of statistical uncertainty estimation uses the Central Limit Theorem (CLT). The variance of the statistic ϕ can be calculated as:

$$V(\phi) = \sum_{i,j=1}^m \left(\frac{\partial \phi}{\partial X_i} \right) \left(\frac{\partial \phi}{\partial X_j} \right) \text{Cov}(X_i, X_j), \quad (15)$$

where the $\text{Cov}(X_i, X_j)$ is the covariance between random variables X_i and X_j . Thus, we need to know the covariance between X_i and X_j to calculate the statistical errors.

If particle multiplicities follow a Gaussian distribution with width σ , the statistical uncertainty of the cumulants and cumulant ratios at different orders can be estimated as:

$$\text{error}(C_m) \propto \frac{\sigma^m}{\sqrt{N} \varepsilon^\alpha}, \quad \text{error}(C_n/C_2) \propto \frac{\sigma^{n-2}}{\sqrt{N} \varepsilon^\beta}, \quad (16)$$

where m and n are integer numbers with $m \geq 1$ and $n \geq 2$, α and β are real numbers with $\alpha > 0$ and $\beta > 0$. The N and ε denote the number of events and the particle-reconstruction efficiency, respectively. Thus,

one can find that the statistical uncertainty strongly depends on the width (σ) of the distributions. For similar event statistics, due to the increasing width of the net-proton distributions from peripheral to central collisions, the statistical uncertainties are larger in central collisions than those from peripheral. Furthermore, the reconstruction efficiency increases the statistical uncertainties on the cumulants compared to their corresponding uncorrected case. A more detailed discussion can be found in Appendix B.

The bootstrap method finds the statistical uncertainties on the cumulants in a Monte Carlo way by forming bootstrap samples. It makes use of a random selection of elements with replacement from the original sample to construct bootstrap samples over which the sampling variance of a given order cumulant is calculated [115, 116]. Let X be a random sample representing the experimental dataset. Let μ_r be the estimator of a statistic (such as mean or variance etc.), on which we intend to find the statistical error. Given a parent sample of size n , construct B number of independent bootstrap samples $X_1^*, X_2^*, X_3^*, \dots, X_B^*$, each consisting of n data points randomly drawn with replacement from the parent sample. Then evaluate the estimator in each bootstrap sample:

$$\mu_r^* = \mu_r(X_b^*) \quad b = 1, 2, 3, \dots, B. \quad (17)$$

Then obtain the sampling variance of the estimator as:

$$\text{Var}(\mu_r) = \frac{1}{B-1} \sum_{b=1}^B \left(\mu_r^* - \bar{\mu}_r \right)^2, \quad (18)$$

where $\bar{\mu}_r = \frac{1}{B} \sum_{b=1}^B (\mu_r^*)$. The value of B is optimized and in general, the larger the value of B the better the estimate of the error.

Figure 10 shows the statistical uncertainties on various orders of C_n obtained using the delta theorem and bootstrap methods for Au+Au collisions at $\sqrt{s_{NN}} = 19.6$ GeV. The results are shown as a function of $\langle N_{\text{part}} \rangle$ for each C_n . The value of B is 200. Good agreement of the statistical uncertainties is seen from both methods. The delta theorem method is used for obtaining the statistical uncertainties on the results discussed below.

I. Systematic uncertainty

Systematic uncertainties are estimated by varying the following requirements for $p(\bar{p})$ tracks: DCA, track quality (as reflected by the number of fit points used in track reconstruction), dE/dx and m^2 for $p(\bar{p})$ identification [83]. A $\pm 5\%$ systematic uncertainty associated with determining the efficiency is also considered [8]. All of the different sources of systematic uncertainty are added in quadrature to obtain the final systematic uncertainties on the C_n and its ratios. Figure 11 shows the variations

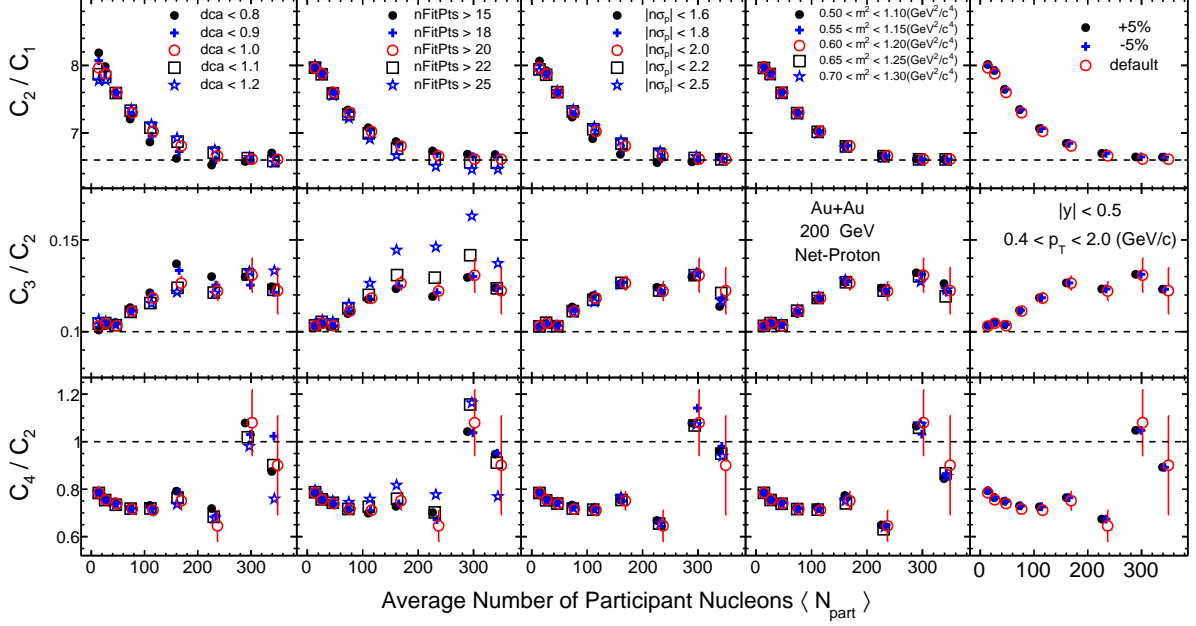


FIG. 11. (Color online) Ratios of cumulants (C_n) as a function of $\langle N_{\text{part}} \rangle$, for net-protons distributions in Au+Au collisions at $\sqrt{s_{\text{NN}}} = 200$ GeV obtained by varying the analysis criteria in terms of track selection criteria, particle identification criteria and efficiency. Since variations with respect to default selection criteria are used to obtain the systematic uncertainties on the measurements, the errors are shown only for the default case.

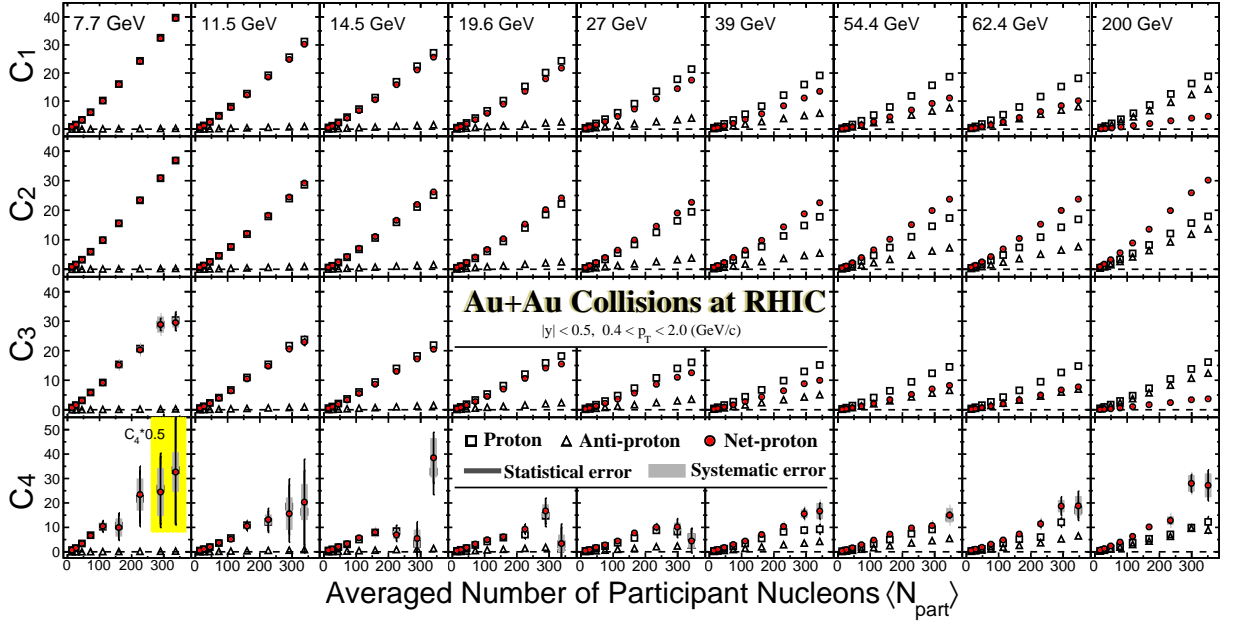


FIG. 12. (Color online) Collision centrality dependence of proton (open squares), antiproton (open triangles) and net-proton (filled circles) cumulants from (7.7 – 200 GeV) Au+Au collisions at RHIC. The data are from $|y| < 0.5$ and $0.4 < p_T < 2.0$ GeV/c. Statistical and systematic uncertainties are shown as the narrow black and wide grey bands, respectively. Note that the net-proton and proton C_4 from 0-5% and 5-10% central Au+Au collisions at 7.7 GeV have been scaled down by a factor of 2, indicated in the yellow box.

TABLE VI. Total systematic uncertainty as well as the absolute uncertainties from individual sources, such as DCA and NhitsFit, for net-proton C_n in 0-5% central Au+Au collisions at $\sqrt{s_{\text{NN}}} = 7.7 - 200$ GeV. The total systematic uncertainties are obtained by adding the uncertainties from individual sources in quadrature.

| $\sqrt{s_{\text{NN}}}$ (GeV) | Cumulant | Total syst. | DCA | NhitsFit | $N_{\sigma,p}$ | m^2 | Efficiency |
|------------------------------|----------|-------------|------|----------|----------------|-------|------------|
| 7.7 | C_1 | 2.42 | 0.85 | 0.78 | 0.99 | 0.028 | 1.88 |
| | C_2 | 2.03 | 0.72 | 0.60 | 0.82 | 0.032 | 1.61 |
| | C_3 | 1.65 | 0.60 | 0.97 | 0.54 | 0.31 | 1.02 |
| | C_4 | 16.20 | 5.56 | 12.54 | 6.40 | 2.68 | 5.11 |
| 11.5 | C_1 | 2.82 | 1.76 | 1.03 | 1.13 | 0.033 | 1.59 |
| | C_2 | 2.34 | 1.44 | 0.73 | 0.99 | 0.020 | 1.37 |
| | C_3 | 1.36 | 0.64 | 0.20 | 0.85 | 0.035 | 0.82 |
| | C_4 | 7.37 | 2.28 | 4.10 | 4.94 | 2.60 | 1.06 |
| 14.5 | C_1 | 1.72 | 0.77 | 0.54 | 0.76 | 0.03 | 1.22 |
| | C_2 | 1.60 | 0.69 | 0.49 | 0.74 | 0.021 | 1.13 |
| | C_3 | 1.16 | 0.52 | 0.44 | 0.51 | 0.047 | 0.78 |
| | C_4 | 8.06 | 2.89 | 3.10 | 5.41 | 0.71 | 4.15 |
| 19.6 | C_1 | 1.46 | 0.60 | 0.62 | 0.56 | 0.045 | 1.03 |
| | C_2 | 1.46 | 0.62 | 0.62 | 0.57 | 0.041 | 1.02 |
| | C_3 | 0.68 | 0.36 | 0.26 | 0.23 | 0.13 | 0.44 |
| | C_4 | 3.65 | 0.86 | 1.99 | 2.58 | 0.59 | 0.89 |
| 27 | C_1 | 1.20 | 0.51 | 0.53 | 0.47 | 0.025 | 0.83 |
| | C_2 | 1.44 | 0.67 | 0.63 | 0.57 | 0.027 | 0.96 |
| | C_3 | 0.62 | 0.33 | 0.27 | 0.23 | 0.035 | 0.39 |
| | C_4 | 3.10 | 1.58 | 1.36 | 1.80 | 0.38 | 1.36 |
| 39 | C_1 | 0.94 | 0.39 | 0.45 | 0.35 | 0.026 | 0.64 |
| | C_2 | 1.48 | 0.67 | 0.67 | 0.59 | 0.033 | 0.97 |
| | C_3 | 0.51 | 0.29 | 0.21 | 0.17 | 0.04 | 0.313 |
| | C_4 | 3.35 | 1.00 | 2.76 | 1.43 | 0.20 | 0.65 |
| 54.4 | C_1 | 0.81 | 0.43 | 0.33 | 0.20 | 0.034 | 0.56 |
| | C_2 | 1.57 | 0.88 | 0.65 | 0.39 | 0.064 | 1.06 |
| | C_3 | 0.42 | 0.27 | 0.15 | 0.078 | 0.025 | 0.27 |
| | C_4 | 2.95 | 1.18 | 1.41 | 1.93 | 1.24 | 0.21 |
| 62.4 | C_1 | 1.04 | 0.45 | 0.49 | 0.35 | 0.044 | 0.71 |
| | C_2 | 2.15 | 1.05 | 1.087 | 0.79 | 0.11 | 1.31 |
| | C_3 | 0.58 | 0.14 | 0.22 | 0.30 | 0.081 | 0.41 |
| | C_4 | 3.99 | 2.40 | 2.30 | 1.38 | 1.21 | 1.23 |
| 200 | C_1 | 0.39 | 0.19 | 0.24 | 0.11 | 0.01 | 0.22 |
| | C_2 | 2.42 | 1.11 | 1.53 | 0.77 | 0.087 | 1.31 |
| | C_3 | 0.39 | 0.24 | 0.18 | 0.19 | 0.074 | 0.14 |
| | C_4 | 4.89 | 2.69 | 3.07 | 1.80 | 1.41 | 1.42 |

of the cumulants ratios with the changes in the above selection criteria for the net-proton distributions in Au+Au collisions at $\sqrt{s_{\text{NN}}} = 200$ GeV.

Table VI gives the systematic uncertainties on the C_n of the net-proton distribution for 0-5% central Au+Au collisions at $\sqrt{s_{\text{NN}}} = 7.7 - 200$ GeV. The statistical and systematic uncertainties are presented separately in the figures.

III. RESULTS

In this section we present the efficiency-corrected cumulants and cumulant ratios of net-proton, proton and antiproton multiplicity distributions in Au+Au collisions at $\sqrt{s_{\text{NN}}} = 7.7, 11.5, 14.5, 19.6, 27, 39, 54.4, 62.4$ and 200 GeV. The cumulant ratios are related to the

ratios of baryon number susceptibilities (χ_B) computed in QCD-motivated models as: $\sigma^2/M = \chi_2^B/\chi_1^B$, $S\sigma = \chi_3^B/\chi_2^B$ and $\kappa\sigma^2 = \chi_4^B/\chi_2^B$ [44, 50, 76–78]. Normalized correlation functions (κ_n/κ_1 , $n > 1$) for proton and antiproton extracted from the measured C_n are also presented. The statistical uncertainties on κ_n are obtained from the uncertainties on C_n using standard error propagation method. These results will be also compared to corresponding results from a hadron resonance gas (HRG) [117] and hadronic-transport-based UrQMD model calculations [118, 119].

In the following subsections, the dependence of the cumulants and correlation functions on collision energy, centrality, rapidity and transverse momentum are presented. The corresponding physics implications are discussed.

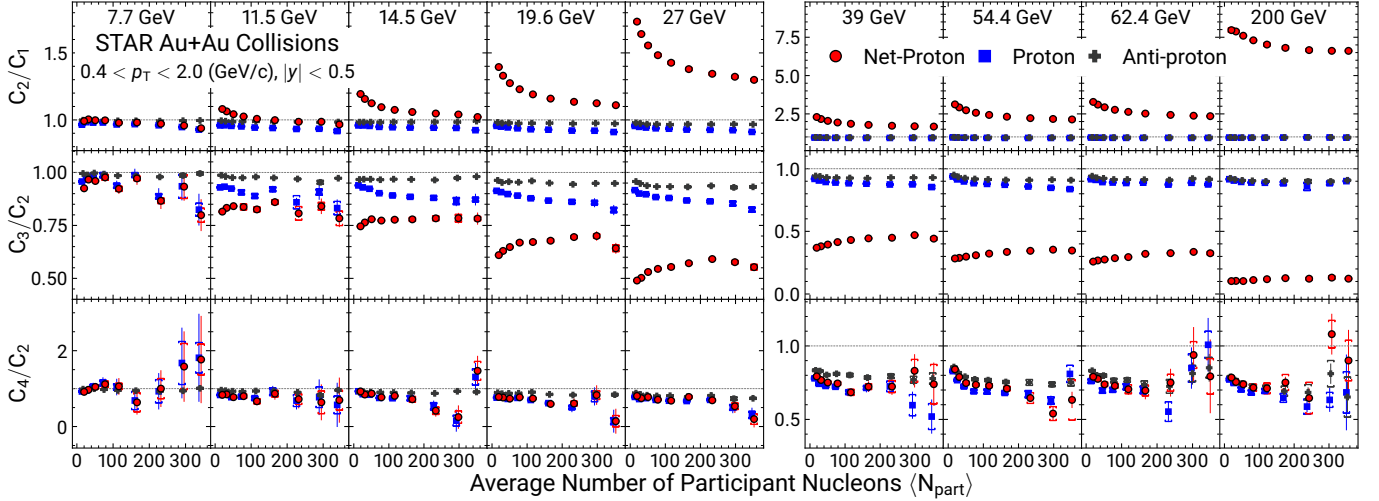


FIG. 13. (Color online) Collision centrality dependence of the cumulant ratios of proton, antiproton and net-proton multiplicity distributions for Au+Au collisions at $\sqrt{s_{\text{NN}}} = 7.7, 11.5, 14.5, 19.6, 27, 39, 54.4, 62.4$ and 200 GeV. The bars and caps represent the statistical and systematic uncertainties, respectively.

A. Centrality dependence

In this subsection, we show the $\langle N_{\text{part}} \rangle$ (representing collision centrality) dependence of the cumulants, cumulant ratios and normalized correlation functions in Au+Au collisions at $\sqrt{s_{\text{NN}}} = 7.7 - 200$ GeV. To understand the evolution of the centrality dependence of the cumulants and cumulant ratios, we invoke the central limit theorem and consider the distribution at any given centrality i to be a superposition of several independent source distributions [35]. Assuming the average number of sources for a given centrality is proportional to the corresponding $\langle N_{\text{part}} \rangle$, the C_n should have a linear dependence on $\langle N_{\text{part}} \rangle$ and the ratios C_2/C_1 , C_3/C_2 and C_4/C_2 should be constant as a function of $\langle N_{\text{part}} \rangle$.

Figure 12 shows the $\langle N_{\text{part}} \rangle$ dependence of C_n for net-proton, proton and antiproton distributions in Au+Au collisions at $\sqrt{s_{\text{NN}}} = 7.7 - 200$ GeV. Since the cumulants are extensive quantities, the C_n for net-proton, proton and antiproton increase with increasing $\langle N_{\text{part}} \rangle$ for all of the $\sqrt{s_{\text{NN}}}$ studied. The different mean values of the proton and antiproton distributions at each energy are determined by the interplay between proton-antiproton pair production and baryon stopping effects. At the lower $\sqrt{s_{\text{NN}}}$, the effects of baryon stopping at midrapidity are more important than at higher $\sqrt{s_{\text{NN}}}$, and therefore the net-proton C_n has dominant contributions from protons. The small mean values for antiprotons at lower $\sqrt{s_{\text{NN}}}$ are due to their low rate of production. At higher $\sqrt{s_{\text{NN}}}$, the pair production process dominates the production of protons and antiprotons at midrapidity. The \bar{p}/p ratio for 0-5% central Au+Au collisions at $\sqrt{s_{\text{NN}}} = 200$ GeV and 7.7 GeV are 0.769 and 0.007, respectively [8, 120]. Large values of C_3 and C_4 also indicate that the net-proton, proton and antiproton distributions are non-Gaussian. To facilitate plotting, the net-proton and proton C_4 from

the 0-5% and 5-10% central Au+Au collisions at $\sqrt{s_{\text{NN}}} = 7.7$ GeV are scaled down by a factor of 2.

Figure 13 shows the $\langle N_{\text{part}} \rangle$ dependence of cumulant ratios C_2/C_1 , C_3/C_2 and C_4/C_2 for net-proton, proton and antiproton distributions measured in Au+Au collisions at $\sqrt{s_{\text{NN}}} = 7.7 - 200$ GeV. In terms of the moments of the distributions, they correspond to σ^2/M (C_2/C_1), $S\sigma$ (C_3/C_2) and $\kappa\sigma^2$ (C_4/C_2). The volume effects are cancelled to the first order in these cumulant ratios. It is found that both of the proton and antiproton cumulant ratios C_2/C_1 and C_3/C_2 show weak variations with $\langle N_{\text{part}} \rangle$. Based on the HRG model with Boltzmann approximation, the orders of baryon number fluctuations can be analytically expressed as $C_1^B/C_2^B = C_3^B/C_2^B = \tanh(\mu_B/T)$ and $C_4^B/C_2^B = 1$, where μ_B and T are the baryon chemical potential and temperature of the system, respectively. The values of net-proton C_2/C_1 show a monotonic decrease with increasing $\langle N_{\text{part}} \rangle$ while the values of C_3/C_2 show a slight increase with $\langle N_{\text{part}} \rangle$. For a fixed centrality, both net-proton C_2/C_1 and C_3/C_2 show strong energy dependence, which can be understood as $C_3/C_2 \propto \tanh(\mu_B/T)$ and $C_2/C_1 \propto 1/\tanh(\mu_B/T)$. At high $\sqrt{s_{\text{NN}}}$, the net-proton $C_3/C_2 \propto \tanh(\mu_B/T) \approx \mu_B/T \rightarrow 0$ and $C_2/C_1 \propto 1/\tanh(\mu_B/T) \approx T/\mu_B > 1$. Since the $\mu_B/T \gg 1$ for the lower energies, the values of net-proton C_2/C_1 and C_3/C_2 approach unity. Due to the connection between higher-order net-proton cumulant ratios and chemical freeze-out μ_B and T , those cumulant ratios have been extensively applied to probe the chemical freeze-out conditions and thermal nature of the medium created in heavy-ion collisions [121–123]. Finally, the net-proton and proton C_4/C_2 ratios have weak $\langle N_{\text{part}} \rangle$ dependence for energies above $\sqrt{s_{\text{NN}}} = 39$ GeV. For energies below $\sqrt{s_{\text{NN}}} = 39$ GeV, the net-proton and proton C_4/C_2 generally show a decreasing trend with increasing $\langle N_{\text{part}} \rangle$, except that, within current uncertain-

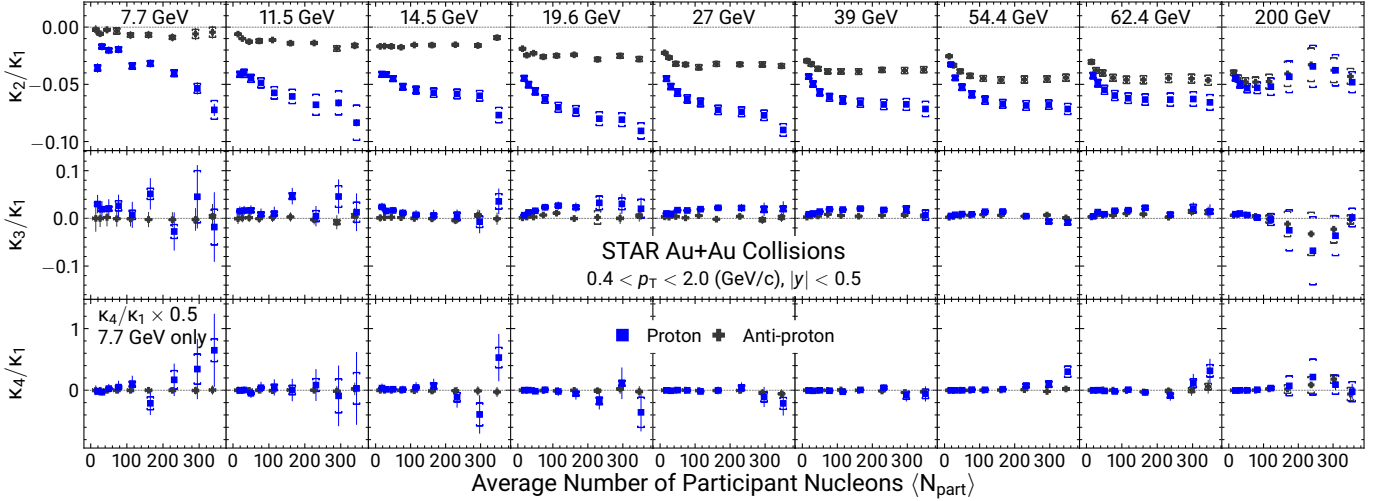


FIG. 14. (Color online) Collision centrality dependence of normalized correlation functions κ_n/κ_1 ($n = 2, 3, 4$) for proton and antiproton multiplicity distributions in Au+Au collisions at $\sqrt{s_{NN}} = 7.7, 11.5, 14.5, 19.6, 27, 39, 54.4, 62.4$ and 200 GeV. The bars and caps represent the statistical and systematic uncertainties, respectively. For clarity, the X-axis values for protons are shifted and the values of proton and antiproton κ_4/κ_1 at $\sqrt{s_{NN}} = 7.7$ GeV are scaled down by a factor of 2.

ties, weak centrality dependences of C_4/C_2 are observed in Au+Au collisions at $\sqrt{s_{NN}} = 7.7$ and 11.5 GeV.

Figure 14 shows the variation of normalized correlation functions κ_n/κ_1 ($n > 1$) with $\langle N_{part} \rangle$ for protons and antiprotons in Au+Au collisions at $\sqrt{s_{NN}} = 7.7 - 200$ GeV. As shown in Eqs. (8)–(10), the proton and antiproton cumulant ratios C_2/C_1 , C_3/C_2 and C_4/C_2 can be expressed in terms of corresponding normalized correlation functions κ_n/κ_1 . Therefore, the results shown in Fig. 14 provide important information on how different orders of multiparticle correlation functions of protons and antiprotons contribute to the cumulant ratios. The values of κ_1 are equal to mean C_1 values for protons and antiprotons, and linearly increase with $\langle N_{part} \rangle$ as shown in Fig. 12. The normalized two-particle correlation functions, κ_2/κ_1 , for protons and antiprotons are found to be negative and increase in magnitude with increasing $\langle N_{part} \rangle$. The values of proton and antiproton κ_2/κ_1 become comparable at $\sqrt{s_{NN}} = 200$ GeV but exhibit larger discrepancies at lower energies. This can be understood as the interplay between baryon stopping and pair production of protons and antiprotons as a function of $\sqrt{s_{NN}}$. Within current uncertainties, no statistically significant deviation from zero is observed in proton normalized correlation functions κ_3/κ_1 and κ_4/κ_1 as a function of collision centrality. As will be discussed later, however, one does observe non-monotonic energy dependence of proton C_4/C_1 in the 0-5% central collisions, see Fig. 25. This is because, as defined in Eq. (7), the fourth-order cumulant C_4 contains contributions from second, third and fourth-order correlation functions (factorial cumulants). In any case, high statistics data from the second phase of the RHIC beam energy scan program (BES-II) are needed to understand the origin of the observed dependences on both collision energy and centrality.

B. Acceptance dependence

In this subsection, we focus on discussing the acceptance dependence of the proton, antiproton and net-proton cumulants (C_n) and cumulant ratios in 0-5% central Au+Au collisions at $\sqrt{s_{NN}} = 7.7 - 200$ GeV. It was pointed out in Refs. [98, 99, 124, 125] that when the rapidity acceptance (Δy) is much smaller than the typical correlation length (ξ) of the system ($\Delta y \ll \xi$), the cumulants (C_n) and correlation functions (κ_n) should scale with some power n of the accepted mean particle multiplicities as $C_n, \kappa_n \propto (\Delta N)^n \propto (\Delta y)^n$. Meanwhile, in the regime where the rapidity acceptance becomes much larger than ξ ($\Delta y \gg \xi$), the C_n and κ_n scale linearly with mean multiplicities or Δy . Thus, the rapidity acceptance dependence of the higher-order cumulants and correlation functions of proton, antiproton and net-proton distributions are important observables to search for a signature of the QCD critical point in heavy-ion collisions. On the other hand, that acceptance dependence of C_n and κ_n could be affected by the effects of non-equilibrium [69, 71, 126] and smearing due to diffusion and hadronic re-scattering [126–129] in the dynamical expansion of the created fireball.

1. Rapidity dependence

Figure 15 shows the rapidity ($-y_{max} < y < y_{max}$, $\Delta y = 2y_{max}$) dependence of the C_n for proton, antiproton and net-proton distributions in 0-5% central Au+Au collisions at $\sqrt{s_{NN}} = 7.7 - 200$ GeV. The measurements are made in the p_T range of 0.4 to 2.0 GeV/c. The rapidity acceptance is cumulatively increased and the C_n values for proton, antiproton and net-proton increase with

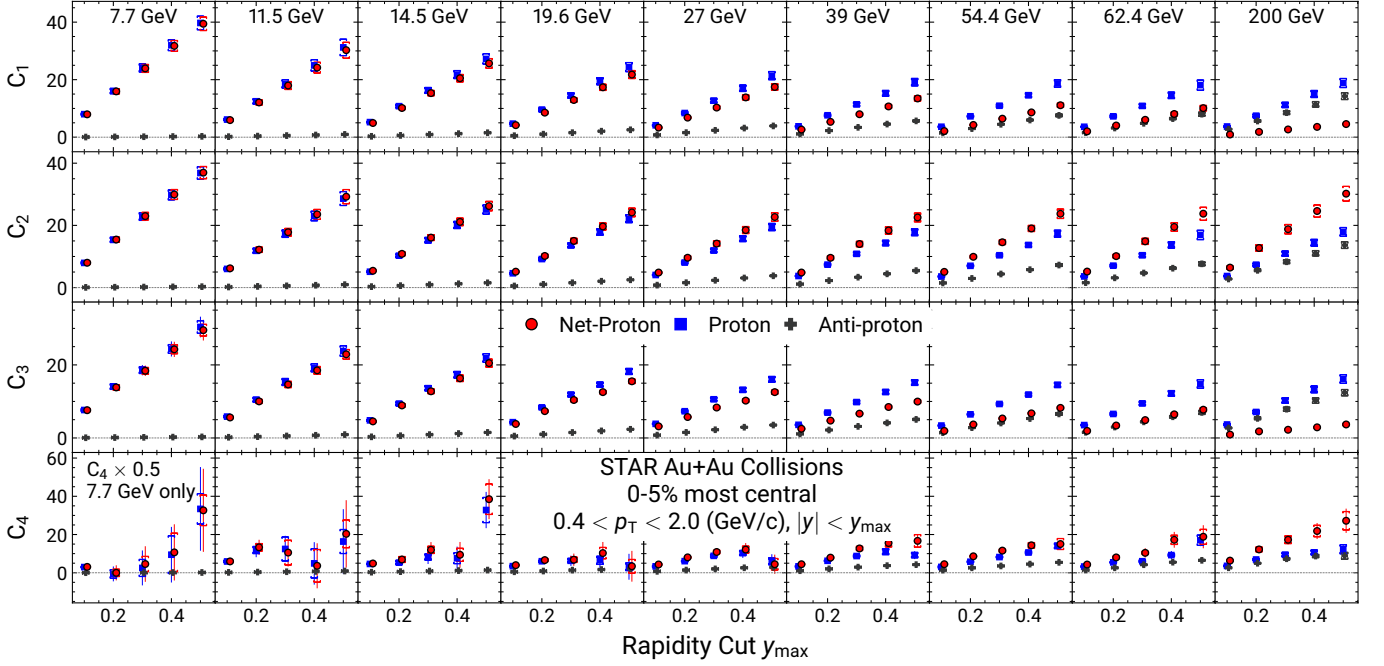


FIG. 15. (Color online) Rapidity acceptance dependence of cumulants of proton, antiproton and net-proton multiplicity distributions in 0-5% central Au+Au collisions at $\sqrt{s_{NN}} = 7.7, 11.5, 14.5, 19.6, 27, 39, 54.4, 62.4$ and 200 GeV. The bars and caps represent statistical and systematic uncertainties, respectively. For clarity, the X-axis values for protons are shifted and the values of proton, antiproton and net-proton C_4 at $\sqrt{s_{NN}} = 7.7$ GeV are scaled down by a factor of 2.

1044 increasing rapidity acceptance. For $\sqrt{s_{NN}} < 27$ GeV¹⁰⁷³
 1045 the proton and net-proton C_n have similar values, an¹⁰⁷⁴
 1046 inevitable consequence of the small production rate of¹⁰⁷⁵
 1047 antiproton at lower energies.¹⁰⁷⁶

1048 Figure 16 shows the variation of normalized correla¹⁰⁷⁷
 1049 tion functions κ_n/κ_1 with rapidity acceptance for pro¹⁰⁷⁸
 1050 ton and antiproton in 0-5% central Au+Au collisions at¹⁰⁷⁹
 1051 $\sqrt{s_{NN}} = 7.7 - 200$ GeV. The κ_2/κ_1 values for protons¹⁰⁸⁰
 1052 and antiprotons are negative and monotonically increas¹⁰⁸¹
 1053 in magnitude when enlarging the rapidity acceptance up¹⁰⁸²
 1054 to $y_{max}=0.5$ ($\Delta y = 1$). For the antiproton, the values¹⁰⁸³
 1055 of κ_2/κ_1 show stronger deviations from zero at higher¹⁰⁸⁴
 1056 $\sqrt{s_{NN}}$. As discussed in Fig. 14, the negative values of¹⁰⁸⁵
 1057 the two-particle correlation functions (κ_2) of protons and¹⁰⁸⁶
 1058 antiprotons are consistent with the expectation of the effe¹⁰⁸⁷
 1059 ct of baryon number conservation. Within current uncer¹⁰⁸⁸
 1060 tainties, the rapidity acceptance dependence for the¹⁰⁸⁹
 1061 κ_3/κ_1 and κ_4/κ_1 of protons and antiprotons in Au+Au¹⁰⁹⁰
 1062 collisions at different $\sqrt{s_{NN}}$ are not significant. The sig¹⁰⁹¹
 1063 nificances of proton κ_4/κ_1 with $|y| < 0.5$ deviating from¹⁰⁹²
 1064 zero are $1.04\sigma, 0.05\sigma, 1.27\sigma, 0.90\sigma, 0.95\sigma, 0.40\sigma, 2.91\sigma,$ ¹⁰⁹³
 1065 $1.43\sigma, 0.11\sigma$ for 0-5% central Au+Au collisions at $\sqrt{s_{NN}}$ ¹⁰⁹⁴
 1066 $= 7.7, 11.5, 14.5, 19.6, 27, 39, 54.4, 62.4$ and 200 GeV,¹⁰⁹⁵
 1067 respectively, where the σ is defined as the sum in quadra¹⁰⁹⁶
 1068 ture of the statistical and systematic uncertainties.¹⁰⁹⁷

1069 Figure 17 shows the rapidity acceptance dependence of¹⁰⁹⁸
 1070 the cumulant ratios $C_2/C_1, C_3/C_2$ and C_4/C_2 for pro¹⁰⁹⁹
 1071 ton, antiproton and net-proton in 0-5% central Au+Au
 1072 collisions at $\sqrt{s_{NN}} = 7.7 - 200$ GeV. Based on Eqs. (8)

to (10), the rapidity acceptance dependence of the cumu¹¹⁰⁰
 1101 lant ratios of proton and antiproton can be understood by
 1102 the interplay between different orders of normalized cor¹¹⁰³
 1103 relation functions (κ_n/κ_1). The negative values of two-
 1104 particle correlation functions (κ_2) for protons and an¹¹⁰⁵
 1105 tiprotons leads to a deviation of the corresponding C_2/C_1
 1106 and C_3/C_2 below unity. Due to low production rate
 1107 of antiproton at low energies, the values of C_2/C_1 and
 1108 C_3/C_2 for the net-proton distributions approach the cor¹¹⁰⁹
 1109 responding values for protons when the beam energy de¹¹¹⁰
 1110 creases. The rapidity acceptance dependence of $C_2/C_1,$
 1111 C_3/C_2 and C_4/C_2 values for protons and antiprotons
 1112 are comparable at $\sqrt{s_{NN}} = 200$ GeV. However, among
 1113 these ratios, protons and antiprotons start to deviate at
 1114 lower beam energies. This is mainly due to baryon stop¹¹¹⁵
 1115 ping and the larger fraction of transported protons compar¹¹¹⁶
 1116 ed with proton-antiproton pair production at midrap¹¹¹⁷
 1117 idity. The C_4/C_2 values for proton, antiproton and net-
 1118 proton distributions are consistent within uncertainties
 1119 for $\sqrt{s_{NN}} = 39, 54.4, 62.4$ and 200 GeV. Significant de¹¹²⁰
 1120 viations from unity are observed for proton and net-pro¹¹²¹
 1121 ton C_4/C_2 at $\sqrt{s_{NN}} = 19.6$ and 27 GeV, and the deviat¹¹²²
 1122 ion decreases with decreasing Δy acceptance, where the
 1123 effects of baryon number conservation plays an important
 1124 role. For energies below 19.6 GeV, the rapidity accep¹¹²⁵
 1125 tance dependence of C_4/C_2 for protons, antiprotons and
 1126 net-protons is not significant within uncertainties.

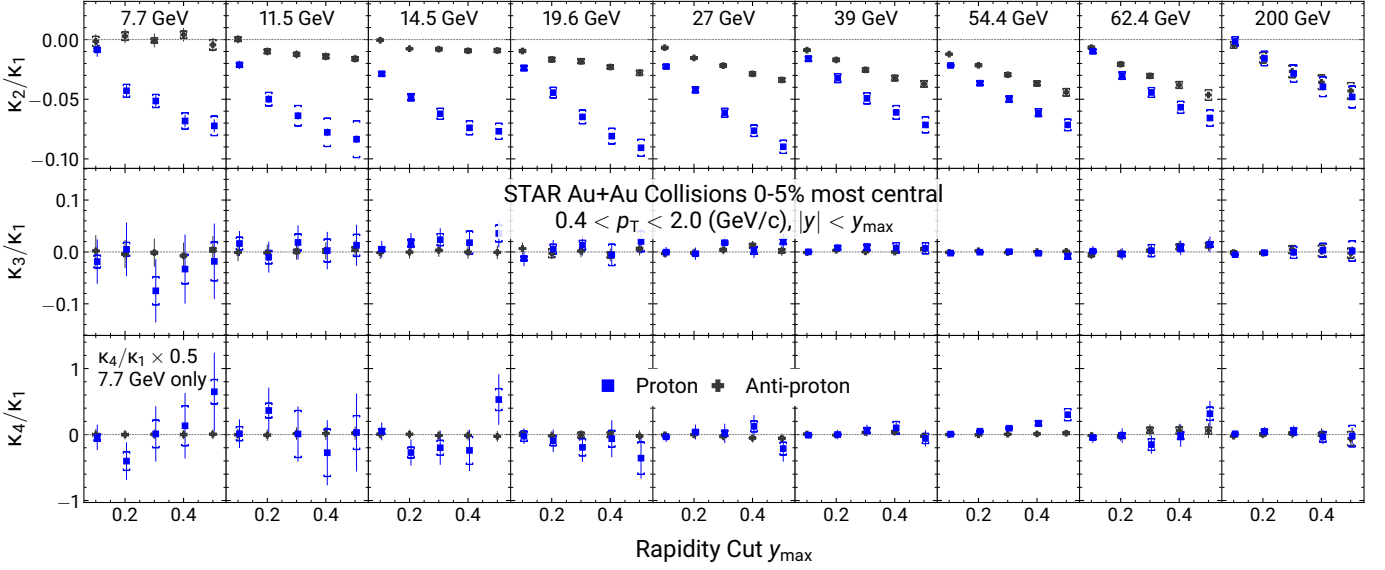


FIG. 16. (Color online) Rapidity acceptance dependence of normalized correlation functions up to fourth order (κ_n/κ_1 , $n = 2, 3, 4$) for proton and antiproton multiplicity distributions in 0-5% central Au+Au collisions at $\sqrt{s_{\text{NN}}} = 7.7, 11.5, 14.5, 19.6, 27, 39, 54.4, 62.4$ and 200 GeV. The X-axis rapidity cut y_{max} is applied as $|y| < y_{\text{max}}$. The bars and caps represent statistical and systematic uncertainties, respectively. For clarity, the X-axis values for protons are shifted and the values of proton and antiproton κ_4/κ_1 at $\sqrt{s_{\text{NN}}} = 7.7$ GeV are scaled down by a factor of 2.

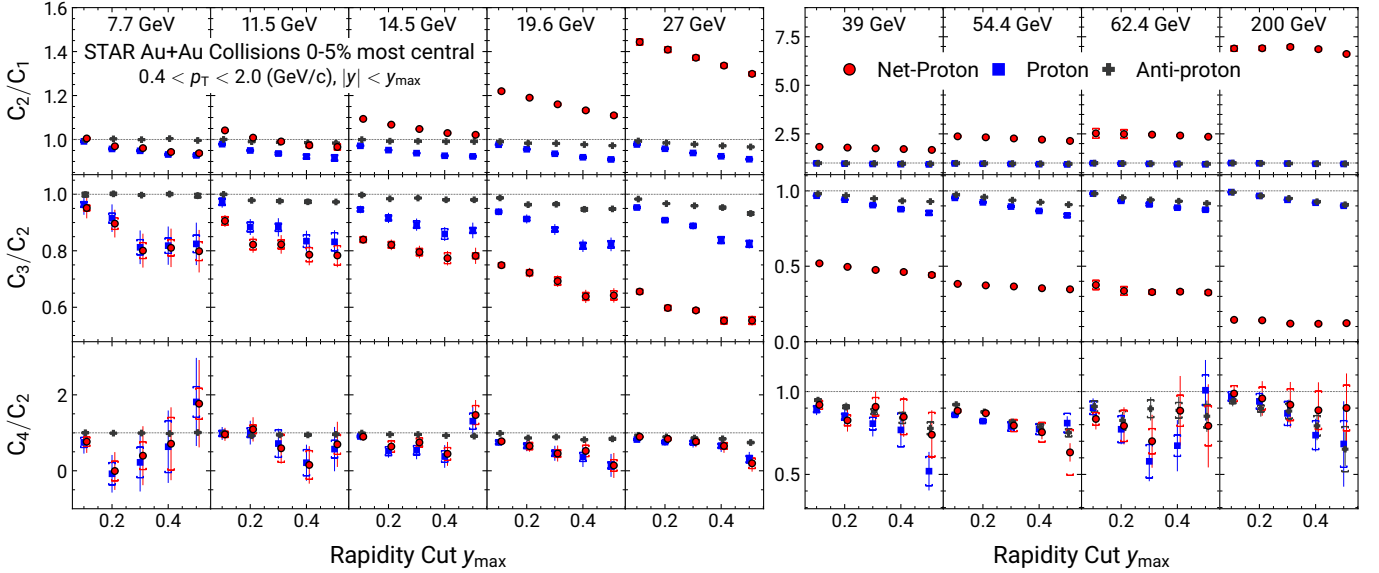


FIG. 17. (Color online) Rapidity-acceptance dependence of cumulant ratios of proton, antiproton and net-proton multiplicity distributions in 0-5% central Au+Au collisions at $\sqrt{s_{\text{NN}}} = 7.7, 11.5, 14.5, 19.6, 27, 39, 54.4, 62.4$ and 200 GeV. The bars and caps represent statistical and systematic uncertainties, respectively. For clarity, the X-axis values for net-protons and protons are shifted.

1100

2. Transverse momentum dependence

Figure 18 shows the p_T acceptance dependence for the C_n of proton, antiproton and net-proton distributions at midrapidity ($|y| < 0.5$) for 0-5% central Au+Au collisions at $\sqrt{s_{\text{NN}}} = 7.7 - 200$ GeV. We fix the lower p_T cut at 0.4 GeV/c, and then the p_T acceptance is increased by

1106

1107

1108

1109

1110

1111

1112

varying the upper limit in steps between 1 and 2 GeV/c. The average efficiency values used in the efficiency correction for various p_T acceptances are calculated based on Eq. (12). By extending the upper p_T coverage from 1 GeV/c to 2 GeV/c, the mean numbers of protons increased about 50% and 80% at $\sqrt{s_{\text{NN}}} = 7.7$ and 200 GeV, respectively. It is found that the C_n values for protons,

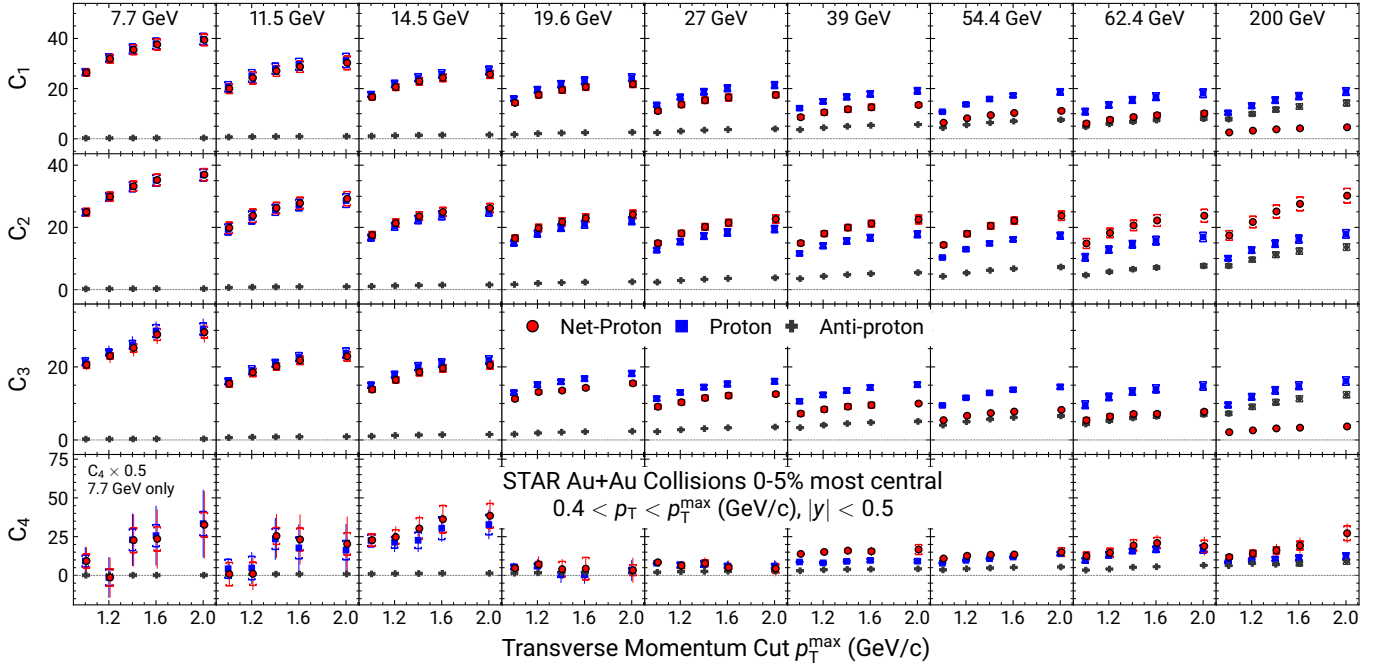


FIG. 18. (Color online) p_T -acceptance dependence of cumulants of proton, antiproton and net-proton multiplicity distributions for 0-5% central Au+Au collisions at $\sqrt{s_{NN}} = 7.7, 11.5, 14.5, 19.6, 27, 39, 54.4, 62.4$ and 200 GeV. The bars and caps represent statistical and systematic uncertainties, respectively. For clarity, the X -axis values for net-protons are shifted and the values of proton, antiproton and net-proton C_4 at $\sqrt{s_{NN}} = 7.7$ GeV are scaled down by a factor of 2.

antiprotons and net protons increase with increasing p_{T142} acceptance, except for a weak p_T acceptance dependence for C_4 observed at energies below 39 GeV.

Figure 19 shows the variation of normalized correlation functions κ_n/κ_1 with p_T acceptance for protons and antiprotons at midrapidity ($|y| < 0.5$) in 0-5% central Au+Au collisions at $\sqrt{s_{NN}} = 7.7 - 200$ GeV. The κ_2/κ_1 values for protons and antiprotons are found to be negative and decrease with increasing p_T acceptance at higher $\sqrt{s_{NN}}$. The κ_2/κ_1 values for antiprotons approach zero when the beam energy is decreased, due to the small production rate of antiprotons at low energies. The negative values of κ_2/κ_1 for protons observed at low energies are mainly dominated by the baryon stopping.

Figure 20 shows the p_T acceptance dependence of C_2/C_1 , C_3/C_2 and C_4/C_2 for proton, antiproton and net-proton distributions in 0-5% central Au+Au collisions at $\sqrt{s_{NN}} = 7.7 - 200$ GeV. In general, most of the ratios show a weak dependence on p_T acceptance for all of the $\sqrt{s_{NN}}$ studied. The C_4/C_2 ratios of proton and net-proton distributions are similar for all $\sqrt{s_{NN}}$ below 27 GeV. The C_3/C_2 ratios for protons and antiprotons are similar at higher beam energy. However, they differ from each other at the lower $\sqrt{s_{NN}}$. From the above differential measurements, it is found that the baryon number conservation strongly influences the cumulants and correlation functions in heavy-ion collisions, especially at low energies. It could be the main reason for the negative two-particle correlation functions for protons and

antiprotons [119].

C. Cumulants from models

Although our results can be compared to several models [118, 130–141], we have chosen two models which do not have phase transition or critical point physics. They have contrasting physics processes to understand the following: (a) the effect of measuring net-protons instead of net-baryons [79, 142], (b) the role of resonance decay for net-proton measurements [143–146], (c) the effect of finite p_T acceptance for the measurements [119, 147], and (d) the effect of net-baryon number conservation [142, 148, 149]. Models without a critical point also provide an appropriate baseline for comparison to data.

1. Hadron resonance gas model

The Hadron Resonance Gas model includes all the relevant degrees of freedom for the hadronic matter and also implicitly takes into account the interactions that are necessary for resonance formation [117, 150]. Hadrons and resonances of masses up to $3 \text{ GeV}/c^2$ are included. Considering a Grand Canonical Ensemble picture, the logarithm of the partition function (Z) in the HRG model

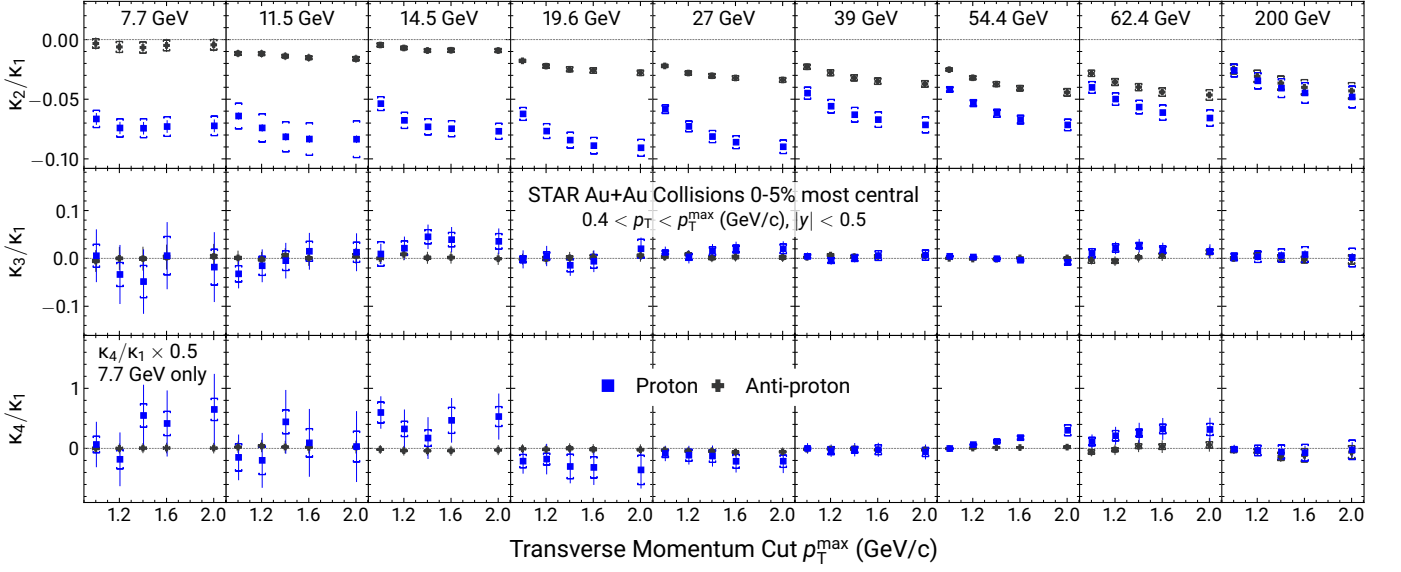


FIG. 19. (Color online) The p_T -acceptance dependence of the normalized correlation functions up to fourth order (κ_n/κ_1 , $n = 2, 3, 4$) for proton and antiproton multiplicity distributions in 0-5% central Au+Au collisions at $\sqrt{s_{NN}} = 7.7, 11.5, 14.5, 19.6, 27, 39, 54.4, 62.4$ and 200 GeV. The bars and caps represent statistical and systematic uncertainties, respectively. For clarity, the X-axis values for protons are shifted and the values of proton and antiproton κ_4/κ_1 at $\sqrt{s_{NN}} = 7.7$ GeV are scaled down by a factor of 2.

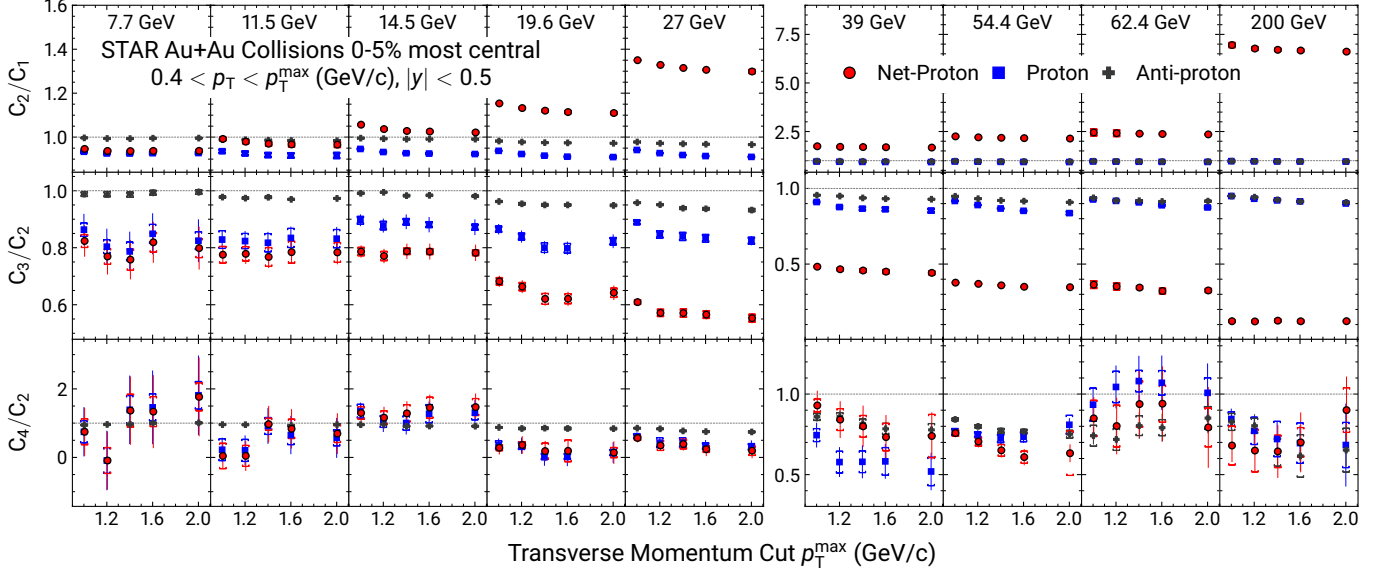


FIG. 20. (Color online) p_T -acceptance dependence of cumulant ratios of proton, antiproton and net-proton multiplicity distributions for 0-5% central Au+Au collisions at $\sqrt{s_{NN}} = 7.7, 11.5, 14.5, 19.6, 27, 39, 54.4, 62.4$ and 200 GeV. The bars and caps represent statistical and systematic uncertainties, respectively. For clarity, the X-axis values for net protons are shifted.

1164 is given as:

$$\ln Z(T, V, \mu) = \sum_B \ln Z_i(T, V, \mu_i) + \sum_M \ln Z_i(T, V, \mu_i), \quad (19)$$

1165 where:

$$\ln Z_i(T, V, \mu_i) = \pm \frac{V g_i}{2\pi^2} \int d^3 p \ln \{1 \pm \exp[(\mu_i - E)/T]\}, \quad (20)$$

1166 T is the temperature, V is the volume of the system, μ_i
1167 is the chemical potential, E is the energy, and g_i is the
1168 degeneracy factor of the i^{th} particle. The total chemi-

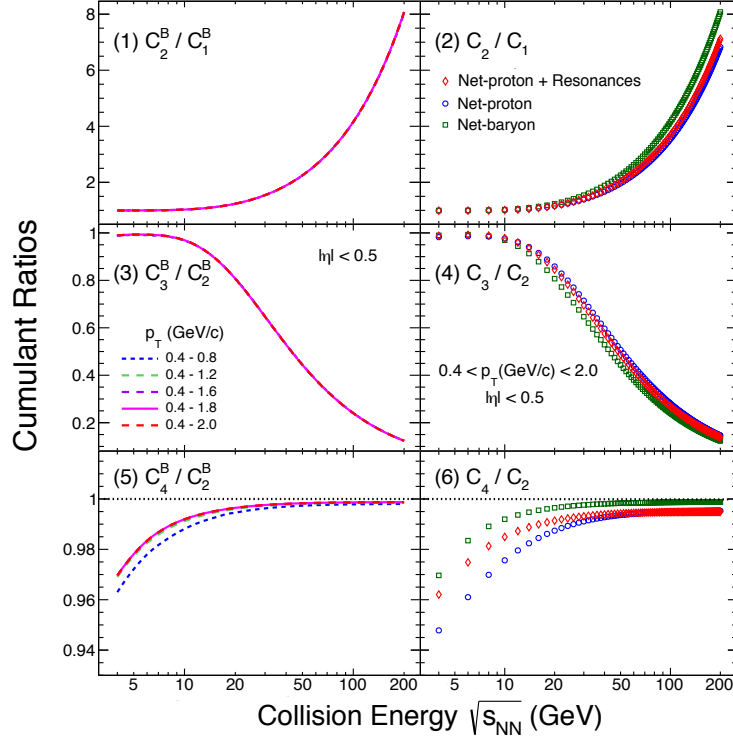


FIG. 21. (Color online) Left panel: Collision energy dependence of C_2^B/C_1^B , C_3^B/C_2^B and C_4^B/C_2^B for various p_T acceptances from the hadron resonance gas model. Right panel: The variation of net-proton and net-baryon C_2/C_1 , C_3/C_2 and C_4/C_2 within the experimental acceptance [117]. Note: this simulation is done within a pseudorapidity window in order to make comparison between baryons of different mass.

cal potential $\mu_i = B_i\mu_B + Q_i\mu_Q + S_i\mu_S$, where B_i , Q_i and S_i are the baryon, electric charge and strangeness number of the i^{th} particle, with corresponding chemical potentials μ_B , μ_Q and μ_S , respectively. The + and - signs in Eq. (20) are for baryons (B) and mesons (M) respectively. The n^{th} -order generalized susceptibility for baryons can be expressed as [150]:

$$\chi_{x,\text{baryon}}^{(n)} = \frac{x^n}{VT^3} \int d^3p \sum_{k=0}^{\infty} (-1)^k (k+1)^n \exp\left\{\frac{-(k+1)E}{T}\right\} \exp\left\{\frac{(k+1)\mu}{T}\right\}, \quad (21)$$

and for mesons:

$$\chi_{x,\text{meson}}^{(n)} = \frac{x^n}{VT^3} \int d^3p \sum_{k=0}^{\infty} (k+1)^n \exp\left\{\frac{-(k+1)E}{T}\right\} \exp\left\{\frac{(k+1)\mu}{T}\right\}. \quad (22)$$

The factor x represents either B , Q or S of the particle, depending on whether the computed χ_x represents baryon, electric charge or strangeness susceptibility.

For a particle of mass m with p_T , η and ϕ , the volume element (d^3p) and energy (E) can be written as $d^3p = p_T m_T \cosh(\eta) dp_T d\eta d\phi$ and $E = m_T \cosh \eta$, where

$m_T = \sqrt{p_T^2 + m^2}$. The experimental acceptance can be incorporated by considering the appropriate integration ranges in η , p_T , ϕ and charge states by considering the values of $|x|$. The total generalized susceptibilities will then be the sum of the contributions from baryons and mesons as in $\chi_x^{(n)} = \sum \chi_{x,\text{baryon}}^{(n)} + \sum \chi_{x,\text{meson}}^{(n)}$.

Figure 21 shows the variation of C_2^B/C_1^B , C_3^B/C_2^B and C_4^B/C_2^B as functions of $\sqrt{s_{\text{NN}}}$ from a hadron resonance gas model [117]. The results are shown for different p_T acceptances. The differences due to acceptance are very small, and the maximum effect is at the level of 5% for $\sqrt{s_{\text{NN}}} = 7.7$ GeV for C_4^B/C_2^B . The HRG results also show that the net-proton results with resonance decays are smaller compared to net baryons and larger than net protons without the decay effect. Here also the effect is at the level of 5% for the lowest $\sqrt{s_{\text{NN}}}$ and smaller at higher energies in the case of C_4^B/C_2^B . The corresponding effect on C_3^B/C_2^B and C_2^B/C_1^B is larger at the higher energies and of the order of 17% for net protons without resonance decay and net baryons, while the effect is 10% for net-proton with resonance decays and net-baryons.

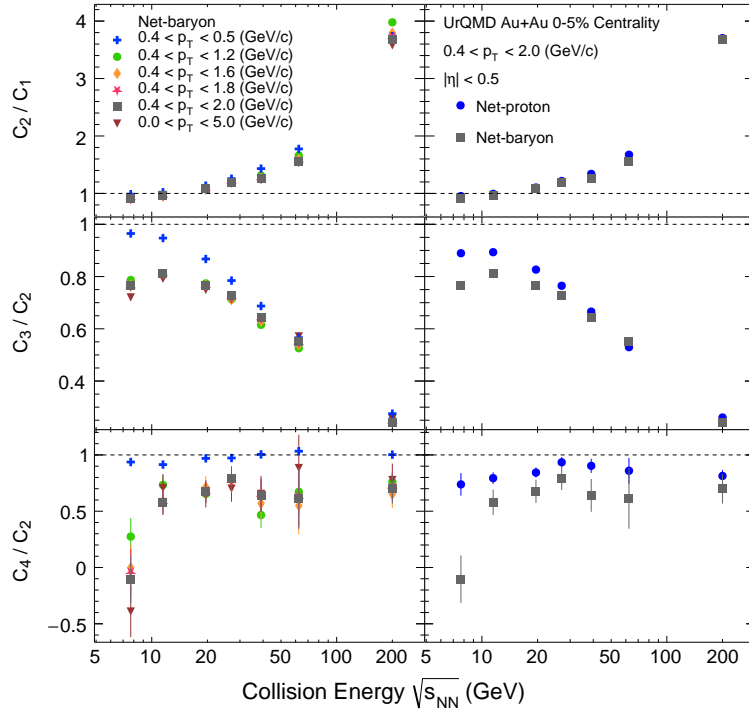


FIG. 22. (Color online) Left panel: UrQMD results on p_T acceptance dependence of C_2/C_1 , C_3/C_2 and C_4/C_2 ratio as a function of $\sqrt{s_{NN}}$ for net baryons. Right panel: Same ratios within the experimental acceptance for net protons and net baryons. Note: similar to Fig 21, this simulation is done within a pseudorapidity window in order to make comparison between baryons of different mass.

2. UrQMD Model

The UrQMD (Ultra relativistic Quantum Molecular Dynamics) model [97, 151] is a microscopic transport model where the phase space description of the reactions are considered. It treats the propagation of all hadrons as classical trajectories in combination with stochastic binary scattering, color string formation and resonance decays. It incorporates baryon-baryon, meson-baryon and meson-meson interactions. The collisional term includes more than 50 baryon species and 45 meson species. The model preserves the conservation of electric charge, baryon number, and strangeness number as expected for QCD matter. It also models the phenomenon of baryon stopping, an essential feature encountered in heavy-ion collisions at lower beam energies. In this model, the space-time evolution of the fireball is studied in terms of excitation and fragmentation of color strings and formation and decay of hadronic resonances. Since the model does not include the physics of the quark-hadron phase transition or the QCD critical point, the comparison of the data to the results obtained from the UrQMD model will shed light on the contributions from the hadronic phase and its associated processes, baryon number conservation and effect of measuring only net protons relative to net baryons.

In Fig. 22, the panels on the left present the energy dependence of C_n ratios of net-baryon distributions for

various p_T acceptance. It is observed that the larger the p_T acceptance, the smaller the cumulant ratios. Furthermore, with the same p_T acceptance, the values of net-baryon C_4/C_2 and C_2/C_1 ratios decrease with decreasing energies. Figure 22 right also shows the comparison of the cumulant ratios for net-baryon and net-proton distributions within the experimental acceptance for various $\sqrt{s_{NN}}$. The differences between results from different acceptance are larger for UrQMD compared to the HRG model. In UrQMD the difference between net baryons and net protons is larger at the lower beam energies for a fixed p_T and y acceptance. The negative C_4/C_2 values of net-baryon distributions observed at low energies could be mainly due to the effect of baryon number conservation. The effects of resonance weak decay and hadronic re-scattering on proton and net-proton number fluctuations in heavy-ion collisions have also been investigated in Ref. [146] within the JAM model. It is important to point out that in both the HRG model and UrQMD transport model calculations, a suppression in C_4/C_2 at low collision energy is observed, as evident from the right plots of Fig. 21 and Fig. 22, respectively. In the case of the transport results, the suppression is attributed to the effect of baryon number conservation in strong interactions. However, the interpretation does not apply to the HRG calculation, since for the grand canonical ensemble (GCE), the event-by-event conservation is absent although, on average, the conservation law is preserved.

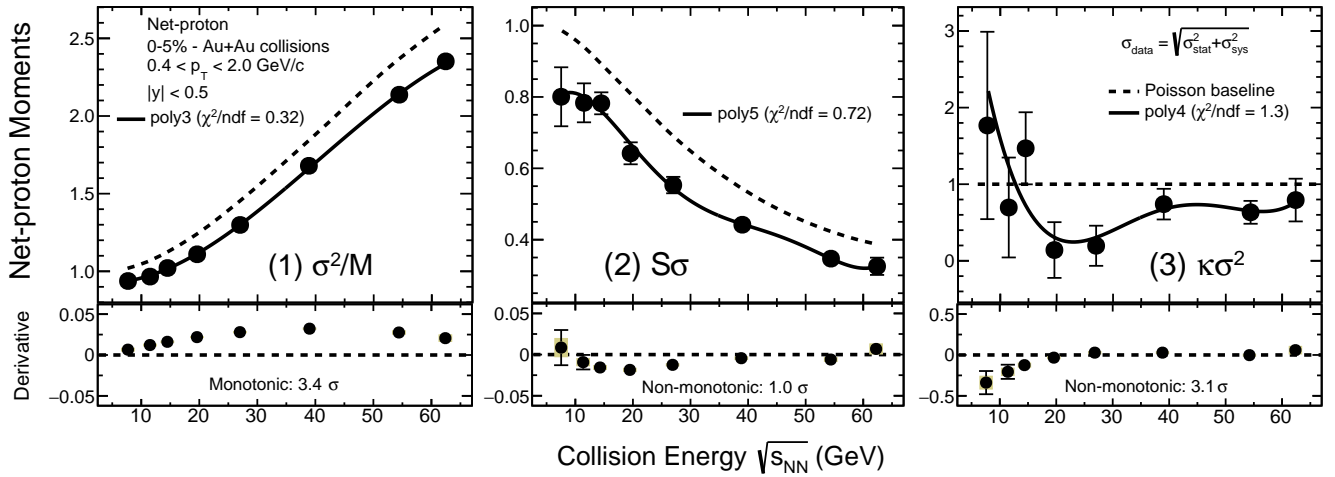


FIG. 23. (Color online) Upper Panel: (1) σ^2/M , (2) $S\sigma$ and (3) $\kappa\sigma^2$ of net-proton distributions for 0-5% central Au+Au collisions from $\sqrt{s_{NN}} = 7.7 - 62.4$ GeV. The error bars on the data points are statistical and systematic uncertainties added in quadrature. The black solid lines are polynomial fit functions which well describe the cumulant ratios. The legends also specify the chi-squared per degree of freedom for the respective fits. The black dashed lines are the Poisson baselines. Lower Panel: Derivative of the fitted polynomial as a function of collision energy. The bar and the gold band on the derivatives represent the statistical and systematic uncertainties, respectively.

In addition to the law of conservation, quantum effects and the change of temperature and baryon chemical potential could play a role here. It is worth noting that the energy dependence of the suppression in C_4/C_2 depends on the details of modeling, especially on proton (baryon) rapidity distributions as it is directly reflecting the local baryon density. This effect is particularly important at lower energy region due to strong stopping in such collisions. Recently, J. Mohs, S. Ryu and H. Elfner reported rather different rapidity distributions for protons in Pb+Pb collisions around SPS energies, compared to those of UrQMD calculations. This is achieved by retuning parameters in string excitation and decay in the hadronic transport model SMASH [152]. In order to establish a non-critical baseline for the critical point search, more systematic theoretical studies of the higher-order cumulant as a function of collision energy with the reliable dynamical models are called for.

3. Energy dependence

Figure 23 shows the collision-energy dependence of cumulant ratios (1) σ^2/M , (2) $S\sigma$ and (3) $\kappa\sigma^2$ of net-proton distributions for 0-5% central Au+Au collisions from $\sqrt{s_{NN}} = 7.7 - 62.4$ GeV. As shown in Fig. 23, a polynomial of order four (five) well describes the plotted collision-energy dependence of $\kappa\sigma^2$ ($S\sigma$) of net-proton distributions for central Au+Au collisions with a $\chi^2/\text{ndf} = 1.3(0.72)$. The local derivative of the fitted polynomial function shown in the lower panel of Fig. 23 changes sign, demonstrating the non-monotonic variation of the measurements with respect to collision energy. The statistical and systematic uncertainties on derivatives are

obtained by randomly varying the data points at each energy within their statistical and systematic uncertainties.

The significance of the observed non-monotonic dependence of $\kappa\sigma^2$ ($S\sigma$) on collision energy, in the energy range $\sqrt{s_{NN}} = 7.7 - 62.4$ GeV, is obtained based on the fourth (fifth) order polynomial fitting procedure. This significance is evaluated by randomly varying the $\kappa\sigma^2$ and $S\sigma$ data points within their total Gaussian uncertainties (statistical and systematic uncertainties added in quadrature) at each corresponding energy. This procedure is repeated a million times for $\kappa\sigma^2$ and for $S\sigma$. Out of 1 million trials, there are 1143 cases for $\kappa\sigma^2$ and 158640 cases for $S\sigma$ where the signs of the derivative at all $\sqrt{s_{NN}}$ are found to be the same. Thus, the probability that at least one derivative at a given $\sqrt{s_{NN}}$ has a different sign from the derivatives at remaining energies among the 1 million trials performed is 0.99886 (0.84136), which corresponds to a 3.1 σ (1.0 σ) effect for $\kappa\sigma^2$ ($S\sigma$). Similarly, based on the third-order polynomial fitting procedure, the cumulant ratio σ^2/M on the other hand ($\chi^2/\text{ndf} = 0.32$), exhibits a monotonic dependence on collision energy with a significance of 3.4 σ . Thus we find that the cumulant ratios as a function of collision energy change from a monotonic variation to a non-monotonic variation with $\sqrt{s_{NN}}$ as we go to higher orders. This is consistent with the QCD-based model expectation that, the higher the order of the moments, the more sensitive it is to physics processes such as a critical point [46, 75]. A test of the non-monotonicity energy dependence with $\kappa\sigma^2$ is also carried out with the energy range $\sqrt{s_{NN}} = 7.7 - 200$ GeV and the resulting significance is 3.0 σ .

Figure 24 shows the collision-energy dependence of the cumulant ratios of net-proton multiplicity distributions

TABLE VII. The right-tail p values of a chi-squared test between experimental data and various models (shown in Fig. 24) for the energy dependence of the net-proton cumulant ratios in 0-5% central Au+Au collisions at two ranges of collision energy: $\sqrt{s_{\text{NN}}} = 7.7 - 27$ GeV and $7.7 - 62.4$ GeV (the latter shown in the parenthesis). Those p values denote the probability of obtaining discrepancies at least as large as the results actually observed [153]. The right-tail p values are calculated via $p = \Pr(\chi_n^2 > \chi^2)$, where χ_n^2 obeys the chi-square distribution with n independent energy data points and the χ^2 values are obtained in the chi-squared test.

| Cumulant Ratios | HRG GCE | HRG CE | HRG GCE+E.V. (R=0.5 fm) | UrQMD |
|-----------------|-------------------|-----------------|-------------------------|-----------------|
| C_2/C_1 | <0.001(<0.001) | <0.001(<0.001) | <0.001(<0.001) | <0.001(<0.001) |
| C_3/C_2 | <0.001(<0.001) | 0.0754 (<0.001) | <0.001(<0.001) | <0.001(<0.001) |
| C_4/C_2 | 0.00553 (0.00174) | 0.0450 (0.128) | 0.0145 (0.0107) | 0.0221 (0.0577) |

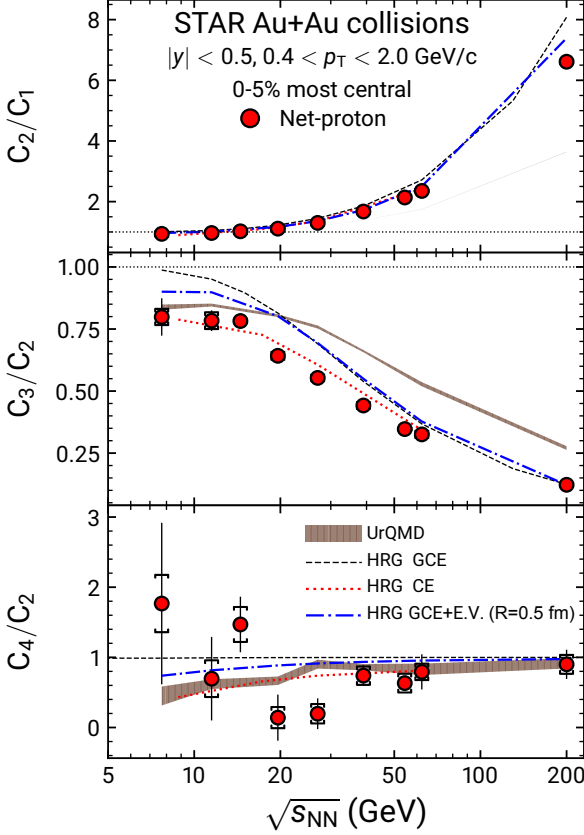


FIG. 24. (Color online) Collision energy dependence of C_2/C_1 , C_3/C_2 and C_4/C_2 for net-proton multiplicity distributions in 0-5% central Au+Au collisions. The experimental net-proton measurements are compared to corresponding values from UrQMD and HRG models within the experimental acceptances. The bars and caps represent the statistical and systematic uncertainties of the experimental data, respectively. The widths of the bands reflect the statistical uncertainties for the model calculations.

1330 experimental measurements of net-proton C_4/C_2 ratios show
 1331 a non-monotonic variation with $\sqrt{s_{\text{NN}}}$. On the other
 1332 hand, the net-proton C_3/C_2 (C_2/C_1) in both model and
 1333 data show a smooth decrease (increase) trend with increas-
 1334 ing $\sqrt{s_{\text{NN}}}$. Although both models show a smooth
 1335 energy dependence, the third-order ratios in the mid-
 1336 dle panel are larger for UrQMD than for (GCE) HRG
 1337 at collision energies above 14.5 GeV. At lower energy, a
 1338 suppression relative to the results of GCE HRG is ob-
 1339 served. On the other hand, the canonical ensemble (CE)
 1340 HRG, has presented a consistent suppression in all three
 1341 panels. In this approach, the baryon number conserva-
 1342 tion is the main source of the suppression [154, 155].
 1343 It is interesting to point out that GCE models incor-
 1344 porating excluded volume effects (GCE E.V.) can also
 1345 reproduce the suppression. The larger the repulsive vol-
 1346 ume, the stronger the suppression. Since the repulsive
 1347 volume reflects the ‘baryon density’, the observed sup-
 1348 pression GCE E.V. is due to the local density. For de-
 1349 tails, see Refs. [141, 156, 157]. To quantify the level
 1350 of agreement between the experimental measurements
 1351 and the model calculations, the widely used χ^2 test
 1352 has been applied for two energy ranges ($\sqrt{s_{\text{NN}}} = 7.7$
 1353 $- 27$ and $7.7 - 62.4$ GeV). The χ^2 value is calculated
 1354 as $\chi^2(R) = \sum_{\sqrt{s_{\text{NN}}}} \frac{|R_{\text{data}} - R_{\text{model}}|^2}{\text{error}^2}$, where R denotes the
 1355 cumulant ratios (C_2/C_1 , C_3/C_2 , C_4/C_2) and the ‘er-
 1356 ror’ represents the statistical and systematic uncertain-
 1357 ties of the data and the statistical uncertainties of the
 1358 model added in quadrature. In addition, the obtained χ^2
 1359 value can be converted to the corresponding right-tail p -
 1360 value, which is the probability of obtaining discrepan-
 1361 cies at least as large as the results actually observed [153].
 1362 The resulting right tail p -values listed in Table VII are
 1363 calculated via $p = \Pr(\chi_n^2 > \chi^2)$, where χ_n^2 obeys the
 1364 chi-square distribution with n independent energy data
 1365 points and the χ^2 values are obtained in the chi-squared
 1366 test. Usually, for the right tail p -value test, $p < 0.05$ is
 1367 the commonly used standard to reject the null hypoth-
 1368 esis and claim a significant deviation between the data
 1369 and model results. It is found that the p -values from
 1370 the the χ^2 test are smaller than 0.05 for all of the dif-
 1371 ferent variants of HRG and the UrQMD model at $\sqrt{s_{\text{NN}}}$
 1372 $= 7.7 - 27$ GeV, which means the deviations between
 1373 data and model results are significant and cannot be ex-
 1374 plained by statistical fluctuations. But, for the range

1324 for 0-5% central Au+Au collisions. The comparison has
 1325 been made between experimental measurements and the
 1326 corresponding results from the HRG and UrQMD mod-
 1327 els. We observe that both models, which do not have
 1328 phase transition effects, show monotonic variations of the
 1329 cumulant ratios with beam energy. However, the experi-

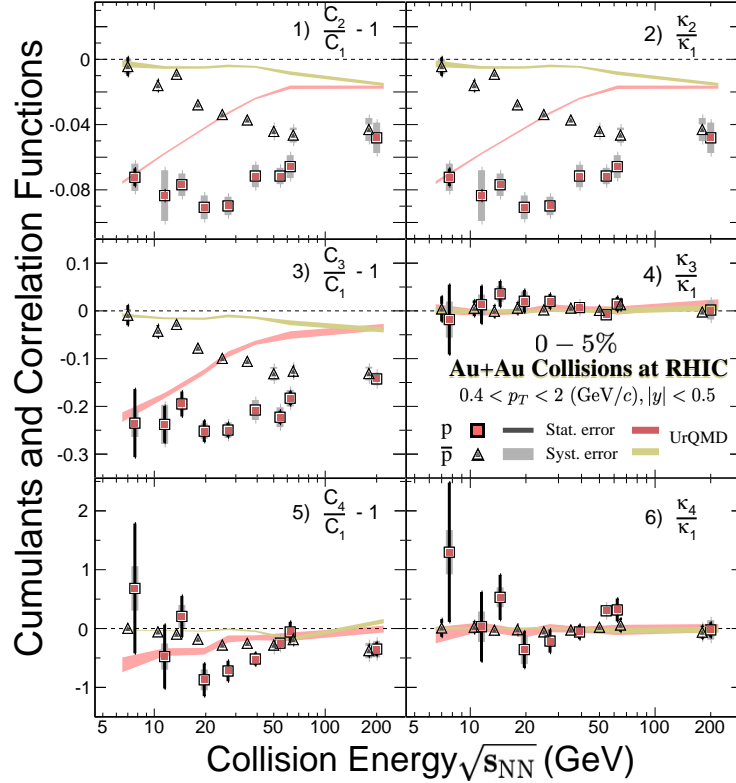


FIG. 25. (Color online) Collision energy dependence of the scaled (anti)proton cumulants and correlation functions in 0-5% central Au+Au collisions at $\sqrt{s_{NN}} = 7.7, 11.5, 14.5, 19.6, 27, 39, 54.4, 62.4$ and 200 GeV. The error bars and bands represent the statistical and systematic uncertainties, respectively. The results from UrQMD model calculation are also shown for comparison.

1375 $\sqrt{s_{NN}} = 7.7 - 62.4$ GeV, the p -values of C_4/C_2 for the 401
 1376 HRG CE and UrQMD model cases are 0.128 and 0.0577 402
 1377 respectively. Clearly as far as these tests are concerned 403
 1378 all of the above-mentioned models, showing monotonic 404
 1379 energy dependences, do not fit the data in the most rele- 405
 1380 vant energy region, $\sqrt{s_{NN}} \leq 27$ GeV. This result will be 406
 1381 further tested with the high-precision data from RHIC 407
 1382 BES-II program. 1408

1383 Based on Eq. (7), the cumulants can be expressed in 1410
 1384 terms of the sum of various-order multiparticle correla- 1411
 1385 tion functions. In order to understand the contributions 1412
 1386 to the cumulants, one can present different orders of cor- 1413
 1387 relation functions separately. Figure 25 shows the en- 1414
 1388 ergy dependence of the cumulants and correlation func- 1415
 1389 tions normalized by the mean numbers of protons and 1416
 1390 antiprotons in 0-5% central Au+Au collisions. By defini- 1417
 1391 tion and as shown in Fig. 25, the values of $C_2/C_1 - 1$ 1418
 1392 are equal to κ_2/κ_1 . It is observed that the normalized sec- 1419
 1393 ond and third-order cumulants minus unity ($C_2/C_1 - 1$ 1420
 1394 $C_3/C_1 - 1$) are negative and show an increasing (de- 1421
 1395 creasing) energy dependence in magnitude for protons 1422
 1396 (antiprotons) with decreasing collision energies. From 1423
 1397 the right panels in Fig. 25, the third-order normalized 1424
 1398 correlation functions (κ_3/κ_1) of protons and antiprotons 1425
 1399 show flat energy dependence and are consistent with zero 1426
 1400 within uncertainties. Therefore, the energy dependence

for C_3/C_1 is dominated by the negative two-particle nor-
 malized correlation functions (κ_2/κ_1), which is mainly
 due to the effects of baryon number conservation. The
 normalized four-particle correlation functions (κ_4/κ_1) of
 antiprotons show flat energy dependence and are consis-
 tent with zero within uncertainties. In panel 5) of
 Fig. 25, we observe a similar energy dependence trend
 for the normalized fourth order cumulants (C_4/C_1) of
 protons as for the net-proton C_4/C_2 in 0-5% central
 Au+Au collisions shown in Fig. 24. For $\sqrt{s_{NN}} \geq 19.6$
 GeV, the values of proton C_4/C_1 are dominated by the
 negative two-particle correlation function (κ_2) of protons
 (see panel 2 in Fig. 25). For $\sqrt{s_{NN}} < 19.6$ GeV, the
 four-particle correlation function (κ_4) of protons plays
 a role in determining the energy dependence of proton
 C_4/C_1 , which cannot be solely understood by the sup-
 pression effects due to negative values of κ_2 for protons.
 As discussed in Refs. [98, 158], the observed large val-
 ues of the four-particle correlation function of protons
 (κ_4) could be attributed to the formation of proton clus-
 ter and related to the signature of a critical point or a
 first order phase transition. Therefore, it is necessary to
 perform precise measurements of the κ_4/κ_1 of protons
 below 19.6 GeV with high statistics data taken in the
 second phase of the beam energy scan at RHIC. In addi-
 tion, we compare the experimental data in Fig. 25 with

UrQMD model calculations. The energy dependence of the second- and third-order normalized cumulants and correlation functions can be qualitatively described by the UrQMD model. However, the non-monotonic energy dependence observed in the proton C_4/C_1 cannot be described by the UrQMD model. Furthermore, the three- and four-particle correlation functions (κ_3 and κ_4) for (anti)protons from UrQMD show flat energy dependence and are consistent with zero. Thus, it indicates that the higher-order (anti)proton correlation functions κ_3 and κ_4 are not sensitive to the effect of baryon number conservation within the current acceptance, and therefore can serve as good probes of critical fluctuations in heavy-ion collisions [119, 146].

IV. SUMMARY AND OUTLOOK

In summary, we report a systematic study of the cumulants of the net-proton, proton and antiproton multiplicity distributions from Au+Au collisions at $\sqrt{s_{NN}} = 7.7 - 200$ GeV. The data have been collected with the STAR experiment in the first phase of the RHIC beam energy scan acquired over the period of 2010 - 2017. The energy, centrality and acceptance dependence of the correlation functions of protons and antiprotons are presented in this paper. Both cumulants and correlation functions up to fourth order at midrapidity ($|y| < 0.5$) within $0.4 < p_T < 2.0$ GeV/c in Au+Au collisions are presented to search for the signatures of a critical point and/or a first-order phase transition over a broad region of baryon chemical potential.

The protons and antiprotons are identified with greater than 97% purity using the TPC and TOF detectors of STAR. The centrality selection is based on midrapidity pions and kaons only to avoid self-correlation effects. The maximum-allowed rapidity acceptance around midrapidity has been used for centrality determination to minimize the effect of centrality resolution. The variation of the average number of protons and antiprotons in a given centrality bin has been accounted for by applying a centrality bin-width correction, which also minimizes volume fluctuation effects. The cumulants are corrected for the proton and antiproton reconstruction efficiencies using a binomial response function. Study of the unfolding technique for efficiency correction of cumulants has shown that, even in the 0-5% central Au+Au collisions at $\sqrt{s_{NN}} = 200$ GeV, the case with the highest multiplicity, the results are consistent with the commonly-used binomial approach within current statistical uncertainties. The statistical errors on the cumulants are based on the delta theorem method and are shown to be consistent with those obtained by the bootstrap method. A detailed estimate of the systematic uncertainties is also presented. Results on cumulant ratios from different variants of the HRG and the UrQMD models are presented to understand the effects of experimental acceptance, resonance decay, baryon number conservation, and

net-proton versus net-baryon analysis. The cumulant ratios show a centrality and energy dependence, which are neither reproduced by purely hadronic-transport-based UrQMD model calculations, nor by different variants of the hadron resonance gas model. Specifically, the net-proton C_4/C_2 ratio for 0-5% central Au+Au collisions shows a non-monotonic variation with $\sqrt{s_{NN}}$, with a significance of 3.1σ . This is consistent with the expectations of critical fluctuations in a QCD-inspired model. A χ^2 test has been applied to quantify the level of agreement between experimental data and model calculations. The resulting p -values suggest that the models fail to explain the 0-5% Au+Au collision data at $\sqrt{s_{NN}} \leq 27$ GeV. The y and p_T acceptance dependence of the cumulants and their ratios provide valuable data to understand the range of the correlations and their relation to the acceptance of the detector [98, 125]. Furthermore, the systematic analysis presented here can be used to constrain the freeze-out conditions in high-energy heavy-ion collisions using QCD-based approaches, and to understand the nature of thermalization in such collisions [121–123]. From the analysis of multiparticle correlation functions, one observes significant negative values for κ_2 of protons and antiprotons, which are mainly due to the effects of baryon number conservation in heavy-ion collisions. The values of κ_3 of protons and antiprotons are consistent with zero for all of the collision energies studied. Further, the energy dependence trend of proton C_4/C_1 below 19.6 GeV cannot be solely understood by the negative values of κ_2 for protons, and the four-particle correlation function of protons (κ_4) is found to play a role, which needs to be confirmed with the high statistics data taken in RHIC BES-II, which began data-taking in 2018. Upgrades to the STAR detector system have significantly improved the quality of the measurements [2]. Primarily the goal of BES-II is to make high-statistics measurements, with extended kinematic range in rapidity and transverse momentum for the measurements discussed in this paper. The extended kinematic range in rapidity and transverse momentum are brought about by upgrading the inner TPC (iTPC) to extend the measurement coverage to $|\eta| < 1.5$, the p_T acceptance down to 100 MeV/c and improved dE/dx resolution. Particle identification capability will be extended to $-1.6 < \eta < 1.0$ with the addition of an endcap TOF (eTOF) detector. The collected event statistics to date, along with the goal for 2021, are listed in Table VIII.

At the same time, STAR will take data in fixed-target mode to extend $\sqrt{s_{NN}}$ to 3 GeV. With these upgrades, and with the benefits of extended kinematic coverage and the use of sensitive observables, the RHIC BES Phase-II program will allow measurements of unprecedented precision for exploring the QCD phase structure within $200 < \mu_B$ (MeV) < 720 .

TABLE VIII. Total number of collected/expected events in BES phase II for various collision energies ($\sqrt{s_{NN}}$) [2].

| $\sqrt{s_{NN}}$ (GeV) | Year | No. of events (million) |
|-----------------------|------|-------------------------|
| 27 | 2018 | 500 |
| 19.6 | 2019 | 400 |
| 17.3 | 2021 | 250 |
| 14.5 | 2019 | 300 |
| 11.5 | 2020 | 230 |
| 9.2 | 2020 | 160 |
| 7.7 | 2021 | 100 |

ACKNOWLEDGEMENT

We thank S. Gupta, F. Karsch, M. Kitazawa, V. Koch, D. Mishra, J. M. Pawlowski, K. Rajagopal, K. Redlich, M. Stephanov for stimulating discussions related to this work. We thank the RHIC Operations Group and RCF at BNL, the NERSC Center at LBNL, and the Open Science Grid consortium for providing resources and support.

This work was supported in part by the Office of Nuclear Physics within the U.S. DOE Office of Science, the U.S. National Science Foundation, the Ministry of Education and Science of the Russian Federation, National Natural Science Foundation of China, Chinese Academy of Science, the Ministry of Science and Technology of China and the Chinese Ministry of Education, the Higher Education Sprout Project by Ministry of Education at NCKU, the National Research Foundation of Korea, Czech Science Foundation and Ministry of Education, Youth and Sports of the Czech Republic, Hungarian National Research, Development and Innovation Office, New National Excellency Programme of the Hungarian Ministry of Human Capacities, Department of Atomic Energy and Department of Science and Technology of the Government of India, the National Science Centre of Poland, the Ministry of Science, Education and Sports of the Republic of Croatia, RosAtom of Russia and German Bundesministerium für Bildung, Wissenschaft, Forschung und Technologie (BMBF), Helmholtz Association, Ministry of Education, Culture, Sports, Science, and Technology (MEXT) and Japan Society for the Promotion of Science (JSPS).

-
- [1] M. M. Aggarwal *et al.* (STAR Collaboration), (2010) [arXiv:1007.2613 \[nucl-ex\]](#).
- [2] BES-II White Paper (STAR Note) <https://drupal.star.bnl.gov/STAR/starnotes/public/sn0598>.
- [3] Y. Aoki, G. Endrodi, Z. Fodor, S. D. Katz, and K. K. Szabo, *Nature* **443**, 675 (2006), [arXiv:hep-lat/0611014 \[hep-lat\]](#).
- [4] I. Arsene *et al.* (BRAHMS Collaboration), *Nucl. Phys.* **A757**, 1 (2005), [arXiv:nucl-ex/0410020](#).
- [5] B. Back *et al.* (PHOBOS Collaboration), *Nucl. Phys.* **A757**, 28 (2005), [arXiv:nucl-ex/0410022](#).
- [6] K. Adcox *et al.* (PHENIX Collaboration), *Nucl. Phys.* **A757**, 184 (2005), [arXiv:nucl-ex/0410003](#).
- [7] J. Adams *et al.* (STAR Collaboration), *Nucl. Phys.* **A757**, 102 (2005), [arXiv:nucl-ex/0501009](#).
- [8] L. Adamczyk *et al.* (STAR Collaboration), *Phys. Rev.* **C96**, 044904 (2017), [arXiv:1701.07065 \[nucl-ex\]](#).
- [9] S. Borsanyi, Z. Fodor, C. Hoelbling, S. D. Katz, S. Krieg, C. Ratti, and K. K. Szabo (Wuppertal-Budapest Collaboration), *JHEP* **09**, 073 (2010), [arXiv:1005.3508 \[hep-lat\]](#).
- [10] A. Bazavov *et al.* (HotQCD Collaboration), *Phys. Lett.* **B795**, 15 (2019), [arXiv:1812.08235 \[hep-lat\]](#).
- [11] L. Adamczyk *et al.* (STAR Collaboration), *Phys. Rev. Lett.* **110**, 142301 (2013), [arXiv:1301.2347 \[nucl-ex\]](#).
- [12] L. Adamczyk *et al.* (STAR Collaboration), *Phys. Rev. Lett.* **112**, 162301 (2014), [arXiv:1401.3043 \[nucl-ex\]](#).
- [13] L. Adamczyk *et al.* (STAR Collaboration), *Phys. Rev. Lett.* **121**, 032301 (2018).
- [14] L. Adamczyk *et al.* (STAR Collaboration), *Phys. Rev. Lett.* **113**, 052302 (2014), [arXiv:1404.1433 \[nucl-ex\]](#).
- [15] C. S. Fischer, J. Luecker, and C. A. Welzbacher, *Phys. Rev. D* **90**, 034022 (2014), [arXiv:1405.4762 \[hep-ph\]](#).
- [16] C. Shi, Y.-L. Wang, Y. Jiang, Z.-F. Cui, and H.-S. Zong, *JHEP* **07**, 014 (2014), [arXiv:1403.3797 \[hep-ph\]](#).
- [17] F. Gao and Y.-x. Liu, *Phys. Rev.* **D94**, 076009 (2016), [arXiv:1607.01675 \[hep-ph\]](#).
- [18] C. S. Fischer, *Prog. Part. Nucl. Phys.* **105**, 1 (2019), [arXiv:1810.12938 \[hep-ph\]](#).
- [19] F. Gao and J. M. Pawlowski, *Phys. Rev. D* **102**, 034027 (2020), [arXiv:2002.07500 \[hep-ph\]](#).
- [20] W.-J. Fu, J. M. Pawlowski, and F. Rennecke, *Phys. Rev.* **D101**, 054032 (2020), [arXiv:1909.02991 \[hep-ph\]](#).
- [21] M. Buballa, *Phys. Rept.* **407**, 205 (2005), [arXiv:hep-ph/0402234](#).
- [22] W.-J. Fu, Z. Zhang, and Y.-x. Liu, *Phys. Rev.* **D77**, 014006 (2008), [arXiv:0711.0154 \[hep-ph\]](#).
- [23] T. K. Herbst, J. M. Pawlowski, and B.-J. Schaefer, *Phys. Lett. B* **696**, 58 (2011), [arXiv:1008.0081 \[hep-ph\]](#).
- [24] Z. Li, K. Xu, X. Wang, and M. Huang, *Eur. Phys. J.* **C79**, 245 (2019), [arXiv:1801.09215 \[hep-ph\]](#).
- [25] K. Fukushima and T. Hatsuda, *Rept. Prog. Phys.* **74**, 014001 (2011), [arXiv:1005.4814 \[hep-ph\]](#).
- [26] K. Fukushima and C. Sasaki, *Prog. Part. Nucl. Phys.* **72**, 99 (2013), [arXiv:1301.6377 \[hep-ph\]](#).
- [27] M. A. Stephanov, K. Rajagopal, and E. V. Shuryak, *Phys. Rev.* **D60**, 114028 (1999), [arXiv:hep-ph/9903292 \[hep-ph\]](#).
- [28] M. A. Stephanov, *Prog. Theor. Phys. Suppl.* **153**, 139 (2004), [arXiv:hep-ph/0402115](#).
- [29] Z. Fodor and S. D. Katz, *JHEP* **04**, 050 (2004), [arXiv:hep-lat/0402006 \[hep-lat\]](#).
- [30] M. A. Stephanov, *PoS LAT2006*, 024 (2006), [arXiv:hep-lat/0701002](#).
- [31] R. V. Gavai and S. Gupta, *Phys. Rev.* **D78**, 114503 (2008), [arXiv:0806.2233 \[hep-lat\]](#).

- [32] S. Gupta, PoS **CPOD2009**, 025 (2009), [arXiv:0909.4630 \[nucl-ex\]](#).¹⁶⁹⁵
1696
- [33] S. Ejiri, *Phys. Rev.* **D78**, 074507 (2008), [arXiv:0804.3227 \[hep-lat\]](#).¹⁶⁹⁷
1698
- [34] E. S. Bowman and J. I. Kapusta, *Phys. Rev.* **C79**, 015202 (2009), [arXiv:0810.0042 \[nucl-th\]](#).¹⁶⁹⁹
1700
- [35] M. M. Aggarwal *et al.* (STAR Collaboration), *Phys. Rev. Lett.* **105**, 022302 (2010), [arXiv:1004.4959 \[nucl-ex\]](#).¹⁷⁰¹
1702
- [36] A. Bazavov *et al.*, *Phys. Rev. D* **95**, 054504 (2017), [arXiv:1701.04325 \[hep-lat\]](#).¹⁷⁰³
1704
- [37] B. I. Abelev *et al.* (STAR Collaboration), *Phys. Rev. Lett.* **C81**, 024911 (2010), [arXiv:0909.4131 \[nucl-ex\]](#).¹⁷⁰⁶
1707
- [38] J. Adam *et al.* (STAR Collaboration), (2020), [arXiv:2007.14005 \[nucl-ex\]](#).¹⁷⁰⁸
1709
- [39] X. Luo and N. Xu, *Nucl. Sci. Tech.* **28**, 112 (2017), [arXiv:1701.02105 \[nucl-ex\]](#).¹⁷¹⁰
1711
- [40] A. Bzdak, S. Esumi, V. Koch, J. Liao, M. Stephanov and N. Xu, *Phys. Rept.* **853**, 1 (2020), [arXiv:1906.00936 \[nucl-th\]](#).¹⁷¹²
1713
1714
- [41] M. Asakawa, U. W. Heinz, and B. Muller, *Phys. Rev. Lett.* **85**, 2072 (2000), [arXiv:hep-ph/0003169 \[hep-ph\]](#).¹⁷¹⁵
1716
- [42] Y. Hatta and T. Ikeda, *Phys. Rev. D* **67**, 014028 (2003), [arXiv:hep-ph/0210284](#).¹⁷¹⁷
1718
- [43] Y. Hatta and M. A. Stephanov, *Phys. Rev. Lett.* **91**, 102003 (2003), [Erratum: *Phys. Rev. Lett.* **91**, 129901 (2003)], [arXiv:hep-ph/0302002 \[hep-ph\]](#).¹⁷¹⁹
1720
1721
- [44] S. Ejiri, F. Karsch, and K. Redlich, *Phys. Lett.* **B633**, 275 (2006), [arXiv:hep-ph/0509051 \[hep-ph\]](#).¹⁷²²
1723
- [45] V. Koch, A. Majumder, and J. Randrup, *Phys. Rev. Lett.* **95**, 182301 (2005), [arXiv:nucl-th/0505052 \[nucl-th\]](#).¹⁷²⁴
1725
1726
- [46] M. A. Stephanov, *Phys. Rev. Lett.* **102**, 032301 (2009), [arXiv:0809.3450 \[hep-ph\]](#).¹⁷²⁷
1728
- [47] M. Asakawa, S. Ejiri, and M. Kitazawa, *Phys. Rev. Lett.* **103**, 262301 (2009), [arXiv:0904.2089 \[nucl-th\]](#).¹⁷²⁹
1730
- [48] C. Athanasiou, K. Rajagopal, and M. Stephanov, *Phys. Rev. Lett.* **D82**, 074008 (2010), [arXiv:1006.4636 \[hep-ph\]](#).¹⁷³¹
1732
- [49] B. Friman, F. Karsch, K. Redlich, and V. Skokov, *Eur. Phys. J.* **C71**, 1694 (2011), [arXiv:1103.3511 \[hep-ph\]](#).¹⁷³³
1734
- [50] S. Gupta, X. Luo, B. Mohanty, H. G. Ritter, and N. Xu, *Science* **332**, 1525 (2011), [arXiv:1105.3934 \[hep-ph\]](#).¹⁷³⁵
1736
- [51] H.-T. Ding, F. Karsch, and S. Mukherjee, *Int. J. Mod. Phys.* **E24**, 1530007 (2015), [arXiv:1504.05274 \[hep-lat\]](#).¹⁷³⁷
1738
- [52] B. J. Schaefer and M. Wagner, *Phys. Rev. Lett.* **D85**, 034027 (2012), [arXiv:1111.6871 \[hep-ph\]](#).¹⁷³⁹
1740
- [53] J.-W. Chen, J. Deng, and L. Labun, *Phys. Rev. Lett.* **D92**, 054019 (2015), [arXiv:1410.5454 \[hep-ph\]](#).¹⁷⁴¹
1742
- [54] Y. Lu, Y.-L. Du, Z.-F. Cui, and H.-S. Zong, *Eur. Phys. J.* **C75**, 495 (2015), [arXiv:1508.00651 \[hep-ph\]](#).¹⁷⁴³
1744
- [55] J.-W. Chen, J. Deng, H. Kohyama, and L. Labun, *Phys. Rev. Lett.* **D93**, 034037 (2016), [arXiv:1509.04968 \[hep-ph\]](#).¹⁷⁴⁵
1746
- [56] V. Vovchenko, D. V. Anchishkin, M. I. Gorenstein, and R. V. Poberezhnyuk, *Phys. Rev. Lett.* **C92**, 054901 (2015), [arXiv:1506.05763 \[nucl-th\]](#).¹⁷⁴⁷
1748
1749
- [57] L. Jiang, P. Li, and H. Song, *Phys. Rev. Lett.* **C94**, 024918 (2016), [arXiv:1512.06164 \[nucl-th\]](#).¹⁷⁵⁰
1751
- [58] A. Mukherjee, J. Steinheimer, and S. Schramm, *Phys. Rev. Lett.* **C96**, 025205 (2017), [arXiv:1611.10144 \[nucl-th\]](#).¹⁷⁵²
1753
- [59] C. Herold, M. Nahrgang, Y. Yan, and C. Kobdaj, *Phys. Rev. Lett.* **C93**, 021902 (2016), [arXiv:1601.04839 \[hep-ph\]](#).¹⁷⁵⁴
1755
- [60] W. Fan, X. Luo, and H. Zong, *Chin. Phys. Lett.* **C43**, 033103 (2019), [arXiv:1702.08674 \[hep-ph\]](#).¹⁷⁵⁶
1757
1758
- [61] H. Zhang, D. Hou, T. Kojo, and B. Qin, *Phys. Rev. Lett.* **D96**, 114029 (2017), [arXiv:1709.05654 \[hep-ph\]](#).
- [62] G.-y. Shao, Z.-d. Tang, X.-y. Gao, and W.-b. He, *Eur. Phys. J. C* **78**, 138 (2018), [arXiv:1708.04888 \[hep-ph\]](#).
- [63] P. Isserstedt, M. Buballa, C. S. Fischer, and P. J. Gunkel, *Phys. Rev. D* **100**, 074011 (2019), [arXiv:1906.11644 \[hep-ph\]](#).
- [64] D. Mroczek, A. R. Nava Acuna, J. Noronha-Hostler, P. Parotto, C. Ratti, and M. A. Stephanov, *Phys. Rev. C* **103**, 034901 (2021), [arXiv:2008.04022 \[nucl-th\]](#).
- [65] W.-j. Fu, X. Luo, J. M. Pawłowski, F. Rennecke, R. Wen, and S. Yin, (2021), [arXiv:2101.06035 \[hep-ph\]](#).
- [66] L. F. Palhares, E. S. Fraga, and T. Kodama, *J. Phys. G* **G37**, 094031 (2010).
- [67] Z. Pan, Z.-F. Cui, C.-H. Chang, and H.-S. Zong, *Int. J. Mod. Phys. A* **A32**, 1750067 (2017), [arXiv:1611.07370 \[hep-ph\]](#).
- [68] B. Berdnikov and K. Rajagopal, *Phys. Rev. Lett.* **D61**, 105017 (2000), [arXiv:hep-ph/9912274 \[hep-ph\]](#).
- [69] S. Mukherjee, R. Venugopalan, and Y. Yin, *Phys. Rev. Lett.* **117**, 222301 (2016), [arXiv:1605.09341 \[hep-ph\]](#).
- [70] M. Stephanov and Y. Yin, *Phys. Rev. Lett.* **D98**, 036006 (2018).
- [71] S. Wu, Z. Wu, and H. Song, *Phys. Rev. Lett.* **C99**, 064902 (2019), [arXiv:1811.09466 \[nucl-th\]](#).
- [72] K. Rajagopal, G. Ridgway, R. Weller, and Y. Yin, *Phys. Rev. Lett.* **D102**, 094025 (2020), [arXiv:1908.08539 \[hep-ph\]](#).
- [73] X. An, G. Başar, M. Stephanov, and H.-U. Yee, *Phys. Rev. Lett.* **C102**, 034901 (2020), [arXiv:1912.13456 \[hep-th\]](#).
- [74] M. A. Stephanov, *Phys. Rev. Lett.* **D81**, 054012 (2010), [arXiv:0911.1772 \[hep-ph\]](#).
- [75] M. A. Stephanov, *Phys. Rev. Lett.* **107**, 052301 (2011), [arXiv:1104.1627 \[hep-ph\]](#).
- [76] M. Cheng *et al.*, *Phys. Rev. Lett.* **D79**, 074505 (2009), [arXiv:0811.1006 \[hep-lat\]](#).
- [77] B. Stokic, B. Friman, and K. Redlich, *Phys. Lett. B* **B673**, 192 (2009), [arXiv:0809.3129 \[hep-ph\]](#).
- [78] R. V. Gavai and S. Gupta, *Phys. Lett. B* **B696**, 459 (2011), [arXiv:1001.3796 \[hep-lat\]](#).
- [79] M. Kitazawa and M. Asakawa, *Phys. Rev. Lett.* **C86**, 024904 (2012), [Erratum: *Phys. Rev. Lett.* **C86**, 069902 (2012)], [arXiv:1205.3292 \[nucl-th\]](#).
- [80] A. Bzdak and V. Koch, *Phys. Rev. Lett.* **C86**, 044904 (2012), [arXiv:1206.4286 \[nucl-th\]](#).
- [81] K. H. Ackermann *et al.* (STAR Collaboration), *Nucl. Instrum. Meth.* **A499**, 624 (2003).
- [82] M. Anderson *et al.*, *Nucl. Instrum. Meth.* **A499**, 659 (2003), [arXiv:nucl-ex/0301015](#).
- [83] L. Adamczyk *et al.* (STAR Collaboration), *Phys. Rev. Lett.* **112**, 032302 (2014), [arXiv:1309.5681 \[nucl-ex\]](#).
- [84] J. Adam *et al.* (STAR), *Phys. Rev. Lett.* **126**, 092301 (2021), [arXiv:2001.02852 \[nucl-ex\]](#).
- [85] W. J. Llope (STAR Collaboration), *Nucl. Instrum. Meth.* **A661**, S110 (2012).
- [86] C. Adler, A. Denisov, E. Garcia, M. J. Murray, H. Strobele, and S. N. White, *Nucl. Instrum. Meth.* **A470**, 488 (2001), [arXiv:nucl-ex/0008005 \[nucl-ex\]](#).
- [87] W. J. Llope *et al.*, *Nucl. Instrum. Meth.* **A522**, 252 (2004), [arXiv:nucl-ex/0308022 \[nucl-ex\]](#).
- [88] F. S. Bieser *et al.*, *Nucl. Instrum. Meth.* **A499**, 766 (2003).
- [89] M. L. Miller, K. Reygers, S. J. Sanders, and P. Steinberg, *Ann. Rev. Nucl. Part. Sci.* **57**, 205 (2007),

- arXiv:nucl-ex/0701025 [nucl-ex]. 1823
- [90] H. Bichsel, *Nucl. Instrum. Meth.* **A562**, 154 (2006). 1824
- [91] X. Luo, J. Xu, B. Mohanty, and N. Xu, *J. Phys.* **G40**, 105104 (2013), arXiv:1302.2332 [nucl-ex]. 1825
- [92] A. Chatterjee, Y. Zhang, J. Zeng, N. R. Sahoo, and X. Luo, *Phys. Rev.* **C101**, 034902 (2020), arXiv:1910.08004 [nucl-ex]. 1826
- [93] M. Zhou and J. Jia, *Phys. Rev.* **C98**, 044903 (2018), arXiv:1803.01812 [nucl-th]. 1827
- [94] T. Sugiura, T. Nonaka, and S. Esumi, *Phys. Rev.* **C100**, 044904 (2019), arXiv:1903.02314 [nucl-th]. 1828
- [95] A. Chatterjee, Y. Zhang, H. Liu, R. Wang, S. He and X. Luo, *Chin. Phys. C* **45**, 064003 (2021), arXiv:2009.03755 [nucl-ex]. 1829
- [96] M. Gyulassy and X.-N. Wang, *Comput. Phys. Commun.* **83**, 307 (1994), arXiv:nucl-th/9502021. 1830
- [97] S. A. Bass *et al.*, *Prog. Part. Nucl. Phys.* **41**, 255 (1998), arXiv:nucl-th/9803035 [nucl-th]. 1831
- [98] B. Ling and M. A. Stephanov, *Phys. Rev.* **C93**, 034915 (2016), arXiv:1512.09125 [nucl-th]. 1832
- [99] A. Bzdak, V. Koch, and N. Strodthoff, *Phys. Rev.* **C95**, 054906 (2017), arXiv:1607.07375 [nucl-th]. 1833
- [100] M. Kitazawa and X. Luo, *Phys. Rev.* **C96**, 024910 (2017), arXiv:1704.04909 [nucl-th]. 1834
- [101] S. He and X. Luo, *Chin. Phys. C* **42**, 104001 (2018), arXiv:1802.02911 [physics.data-an]. 1835
- [102] V. Skokov, B. Friman, and K. Redlich, *Phys. Rev.* **C88**, 034911 (2013), arXiv:1205.4756 [hep-ph]. 1836
- [103] P. Braun-Munzinger, A. Rustamov, and J. Stachel, *Nucl. Phys.* **A960**, 114 (2017), arXiv:1612.00702 [nucl-th]. 1837
- [104] X. Luo, *Phys. Rev.* **C91**, 034907 (2015), arXiv:1410.3914 [physics.data-an]. 1838
- [105] T. Nonaka, M. Kitazawa, and S. Esumi, *Phys. Rev.* **C95**, 064912 (2017), arXiv:1702.07106 [physics.data-an]. 1839
- [106] X. Luo and T. Nonaka, *Phys. Rev.* **C99**, 044917 (2019), arXiv:1812.10303 [physics.data-an]. 1840
- [107] P. Garg, D. K. Mishra, P. K. Netrakanti, A. K. Mohanty, and B. Mohanty, *J. Phys.* **G40**, 055103 (2013), arXiv:1211.2074 [nucl-ex]. 1841
- [108] S. Esumi, K. Nakagawa, and T. Nonaka, *Nucl. Instrum. Meth.* **A987**, 164802 (2021), arXiv:2002.11253 [physics.data-an]. 1842
- [109] V. Fine and P. Nevski, in *Proceedings CHEP 2000, 143* (2000). 1843
- [110] A. Bzdak, R. Holzmann, and V. Koch, *Phys. Rev.* **C94**, 064907 (2016), arXiv:1603.09057 [nucl-th]. 1844
- [111] T. Nonaka, M. Kitazawa, and S. Esumi, *Nucl. Instrum. Meth.* **A906**, 10 (2018), arXiv:1805.00279 [physics.data-an]. 1845
- [112] L. Adamczyk *et al.* (STAR Collaboration), *Phys. Lett.* **B785**, 551 (2018), arXiv:1709.00773 [nucl-ex]. 1846
- [113] X. Luo, *J. Phys.* **G39**, 025008 (2012), arXiv:1109.0593 [physics.data-an]. 1847
- [114] A. Pandav, D. Mallick, and B. Mohanty, *Nucl. Phys.* **A991**, 121608 (2019), arXiv:1809.08892 [nucl-ex]. 1848
- [115] B. Efron, *The Annals of Statistics* **7** p1-26 (1979). 1849
- [116] B. Efron, *Computers and the Theory of Statistics Thinking the Unthinkable* (Society for Industrial and Applied Mathematics, 1979). 1850
- [117] P. Garg, D. K. Mishra, P. K. Netrakanti, B. Mohanty, A. K. Mohanty, B. K. Singh, and N. Xu, *Phys. Lett.* **B726**, 691 (2013), arXiv:1304.7133 [nucl-ex]. 1851
- [118] J. Xu, S. Yu, F. Liu, and X. Luo, *Phys. Rev.* **C94**, 024901 (2016), arXiv:1606.03900 [nucl-ex]. 1852
- [119] S. He and X. Luo, *Phys. Lett.* **B774**, 623 (2017), arXiv:1704.00423 [nucl-ex]. 1853
- [120] B. I. Abelev *et al.* (STAR Collaboration), *Phys. Rev.* **C79**, 034909 (2009), arXiv:0808.2041 [nucl-ex]. 1854
- [121] A. Bazavov *et al.*, *Phys. Rev. Lett.* **109**, 192302 (2012), arXiv:1208.1220 [hep-lat]. 1855
- [122] S. Borsanyi, Z. Fodor, S. D. Katz, S. Krieg, C. Ratti, and K. K. Szabo, *Phys. Rev. Lett.* **111**, 062005 (2013), arXiv:1305.5161 [hep-lat]. 1856
- [123] S. Gupta, D. Mallick, D. K. Mishra, B. Mohanty, and N. Xu, (2020), arXiv:2004.04681 [hep-ph]. 1857
- [124] A. Bzdak and V. Koch, *Phys. Rev.* **C96**, 054905 (2017), arXiv:1707.02640 [nucl-th]. 1858
- [125] J. Brewer, S. Mukherjee, K. Rajagopal, and Y. Yin, *Phys. Rev.* **C98**, 061901 (2018), arXiv:1804.10215 [hep-ph]. 1859
- [126] M. Asakawa, M. Kitazawa, and B. Müller, *Phys. Rev.* **C101**, 034913 (2020), arXiv:1912.05840 [nucl-th]. 1860
- [127] Y. Ohnishi, M. Kitazawa, and M. Asakawa, *Phys. Rev.* **C94**, 044905 (2016), arXiv:1606.03827 [nucl-th]. 1861
- [128] M. Sakaida, M. Asakawa, H. Fujii, and M. Kitazawa, *Phys. Rev.* **C95**, 064905 (2017), arXiv:1703.08008 [nucl-th]. 1862
- [129] M. Nahrgang, M. Bluhm, T. Schaefer, and S. A. Bass, *Phys. Rev.* **D99**, 116015 (2019), arXiv:1804.05728 [nucl-th]. 1863
- [130] J. Li, H.-j. Xu, and H. Song, *Phys. Rev.* **C97**, 014902 (2018), arXiv:1707.09742 [nucl-th]. 1864
- [131] Y. Lin, L. Chen, and Z. Li, *Phys. Rev.* **C96**, 044906 (2017), arXiv:1707.04375 [hep-ph]. 1865
- [132] G. A. Almasi, B. Friman, and K. Redlich, *Phys. Rev.* **D96**, 014027 (2017), arXiv:1703.05947 [hep-ph]. 1866
- [133] Z. Yang, X. Luo, and B. Mohanty, *Phys. Rev.* **C95**, 014914 (2017), arXiv:1610.07580 [nucl-ex]. 1867
- [134] C. Zhou, J. Xu, X. Luo, and F. Liu, *Phys. Rev.* **C96**, 014909 (2017), arXiv:1703.09114 [nucl-ex]. 1868
- [135] A. Zhao, X. Luo, and H. Zong, *Eur. Phys. J.* **C77**, 207 (2017). 1869
- [136] V. Vovchenko, L. Jiang, M. I. Gorenstein, and H. Stoecker, *Phys. Rev.* **C98**, 024910 (2018), arXiv:1711.07260 [nucl-th]. 1870
- [137] M. Albright, J. Kapusta, and C. Young, *Phys. Rev.* **C92**, 044904 (2015), arXiv:1506.03408 [nucl-th]. 1871
- [138] K. Fukushima, *Phys. Rev.* **C91**, 044910 (2015), arXiv:1409.0698 [hep-ph]. 1872
- [139] P. K. Netrakanti, X. F. Luo, D. K. Mishra, B. Mohanty, A. Mohanty, and N. Xu, *Nucl. Phys.* **A947**, 248 (2016), arXiv:1405.4617 [hep-ph]. 1873
- [140] K. Morita, B. Friman, and K. Redlich, *Phys. Lett.* **B741**, 178 (2015), arXiv:1402.5982 [hep-ph]. 1874
- [141] S. Samanta and B. Mohanty, (2019), arXiv:1905.09311 [hep-ph]. 1875
- [142] S. He, X. Luo, Y. Nara, S. Esumi, and N. Xu, *Phys. Lett.* **B762**, 296 (2016), arXiv:1607.06376 [nucl-ex]. 1876
- [143] M. Nahrgang, M. Bluhm, P. Alba, R. Bellwied, and C. Ratti, *Eur. Phys. J.* **C75**, 573 (2015), arXiv:1402.1238 [hep-ph]. 1877
- [144] D. K. Mishra, P. Garg, P. K. Netrakanti, and A. K. Mohanty, *Phys. Rev.* **C94**, 014905 (2016), arXiv:1607.01875 [hep-ph]. 1878
- [145] M. Bluhm, M. Nahrgang, S. A. Bass, and T. Schaefer, *Eur. Phys. J.* **C77**, 210 (2017), arXiv:1612.03889 [nucl-

- th].
- [146] Y. Zhang, S. He, H. Liu, Z. Yang, and X. Luo, *Phys Rev.* **C101**, 034909 (2020), arXiv:1905.01095 [nucl-ex].
- [147] F. Karsch, K. Morita, and K. Redlich, *Phys. Rev.* **C93**, 034907 (2016), arXiv:1508.02614 [hep-ph].
- [148] A. Bzdak, V. Koch, and V. Skokov, *Phys. Rev.* **C87**, 014901 (2013), arXiv:1203.4529 [hep-ph].
- [149] P. Braun-Munzinger, A. Rustamov, and J. Stachel, (2019), arXiv:1907.03032 [nucl-th].
- [150] F. Karsch and K. Redlich, *Phys. Lett.* **B695**, 136 (2011), arXiv:1007.2581 [hep-ph].
- [151] M. Bleicher *et al.*, *J. Phys.* **G25**, 1859 (1999), arXiv:hep-ph/9909407 [hep-ph].
- [152] J. Mohs, S. Ryu, and H. Elfner, *J. Phys. G* **47**, 065101 (2020), arXiv:1909.05586 [nucl-th].
- [153] R. L. Wasserstein and N. A. Lazar, *American Statistician* **70**, 129 (2016).
- [154] J.-H. Fu, *Phys. Rev.* **C96**, 034905 (2017), arXiv:1610.07138 [nucl-th].
- [155] P. Braun-Munzinger, B. Friman, K. Redlich, A. Rustamov, and J. Stachel, (2020), arXiv:2007.02463 [nucl-th].
- [156] J. Fu, *Phys. Lett.* **B722**, 144 (2013).
- [157] A. Bhattacharyya, S. Das, S. K. Ghosh, R. Ray, and S. Samanta, *Phys. Rev.* **C90**, 034909 (2014), arXiv:1310.2793 [hep-ph].
- [158] A. Bzdak, V. Koch, and V. Skokov, *Eur. Phys. J.* **C77**, 288 (2017), arXiv:1612.05128 [nucl-th].
- [159] T. Nonaka, T. Sugiura, S. Esumi, H. Masui, and X. Luo, *Phys. Rev.* **C94**, 034909 (2016), arXiv:1604.06212 [nucl-th].

Appendix A: Efficiency Correction

In order to correct the C_n for efficiency effects, one has to invoke a model assumption for the response of the detector. The detector response is assumed to follow a binomial probability distribution function. The probability distribution function of measured proton number n_p and antiproton number $n_{\bar{p}}$ can be expressed as [80, 104]:

$$p(n_p, n_{\bar{p}}) = \sum_{N_p=n_p}^{\infty} \sum_{N_{\bar{p}}=n_{\bar{p}}}^{\infty} P(N_p, N_{\bar{p}}) \times \frac{N_p!}{n_p! (N_p - n_p)!} (\varepsilon_p)^{n_p} (1 - \varepsilon_p)^{N_p - n_p} \times \frac{N_{\bar{p}}!}{n_{\bar{p}}! (N_{\bar{p}} - n_{\bar{p}})!} (\varepsilon_{\bar{p}})^{n_{\bar{p}}} (1 - \varepsilon_{\bar{p}})^{N_{\bar{p}} - n_{\bar{p}}} \quad (\text{A1})$$

where the $P(N_p, N_{\bar{p}})$ is the original joint probability distribution of number of proton (N_p) and antiproton ($N_{\bar{p}}$) and $\varepsilon_p, \varepsilon_{\bar{p}}$ are the efficiency of reconstructing the protons

and antiprotons, respectively. In order to arrive at an expression for efficiency-corrected cumulants or moments, the bivariate factorial moments are first defined as:

$$F_{i,k}(N_p, N_{\bar{p}}) = \left\langle \frac{N_p!}{(N_p - i)!} \frac{N_{\bar{p}}!}{(N_{\bar{p}} - k)!} \right\rangle = \sum_{N_p=i}^{\infty} \sum_{N_{\bar{p}}=k}^{\infty} P(N_p, N_{\bar{p}}) \frac{N_p!}{(N_p - i)!} \frac{N_{\bar{p}}!}{(N_{\bar{p}} - k)!} \quad (\text{A2})$$

$$f_{i,k}(n_p, n_{\bar{p}}) = \left\langle \frac{n_p!}{(n_p - i)!} \frac{n_{\bar{p}}!}{(n_{\bar{p}} - k)!} \right\rangle = \sum_{n_p=i}^{\infty} \sum_{n_{\bar{p}}=k}^{\infty} p(n_p, n_{\bar{p}}) \frac{n_p!}{(n_p - i)!} \frac{n_{\bar{p}}!}{(n_{\bar{p}} - k)!} \quad (\text{A3})$$

The efficiency-corrected factorial moments are then given as:

$$F_{i,k}(N_p, N_{\bar{p}}) = \frac{f_{i,k}(n_p, n_{\bar{p}})}{(\varepsilon_p)^i (\varepsilon_{\bar{p}})^k}. \quad (\text{A4})$$

Then the n^{th} order efficiency-corrected moments of net-proton distributions are related to the efficiency-corrected factorial moments as:

$$m_n(N_p - N_{\bar{p}}) = \langle (N_p - N_{\bar{p}})^n \rangle = \sum_{i=0}^n (-1)^i \binom{n}{i} \langle N_p^{n-i} N_{\bar{p}}^i \rangle = \sum_{i=0}^n (-1)^i \binom{n}{i} \left[\sum_{r_1=0}^{n-i} \sum_{r_2=0}^i s_2(n-i, r_1) s_2(i, r_2) F_{r_1, r_2}(N_p, N_{\bar{p}}) \right] = \sum_{i=0}^n \sum_{r_1=0}^{n-i} \sum_{r_2=0}^i (-1)^i \binom{n}{i} s_2(n-i, r_1) s_2(i, r_2) F_{r_1, r_2}(N_p, N_{\bar{p}}) \quad (\text{A5})$$

The Stirling numbers of the first ($s_1(n, i)$) and second kind ($s_2(n, i)$), are defined as:

$$\frac{N!}{(N-n)!} = \sum_{i=0}^n s_1(n, i) N^i \quad (\text{A6})$$

$$N^n = \sum_{i=0}^n s_2(n, i) \frac{N!}{(N-i)!} \quad (\text{A7})$$

using the recursion relation:

$$C_r(N_p - N_{\bar{p}}) = m_r(N_p - N_{\bar{p}}) - \sum_{s=1}^{r-1} \binom{r-1}{s-1} C_s(N_p - N_{\bar{p}}) m_{r-s}(N_p - N_{\bar{p}}) \quad (\text{A8})$$

where the C_r denotes the r^{th} -order cumulants of net-proton distributions.

If the protons and antiprotons has the same efficiency, $\varepsilon_p = \varepsilon_{\bar{p}} = \varepsilon$, the expressions for the first four efficiency-corrected cumulants can be explicitly written as:

$$\begin{aligned} C_1^{X-Y} &= \frac{\langle x \rangle - \langle y \rangle}{\varepsilon} \\ C_2^{X-Y} &= \frac{C_2^{x-y} + (\varepsilon - 1)(\langle x \rangle + \langle y \rangle)}{\varepsilon^2} \\ C_3^{X-Y} &= \frac{C_3^{x-y} + 3(\varepsilon - 1)(C_2^x - C_2^y) + (\varepsilon - 1)(\varepsilon - 2)(\langle x \rangle - \langle y \rangle)}{\varepsilon^3} \\ C_4^{X-Y} &= \frac{C_4^{x-y} - 2(\varepsilon - 1)C_3^{x+y} + 8(\varepsilon - 1)(C_3^x + C_3^y) + (5 - \varepsilon)(\varepsilon - 1)C_2^{x+y}}{\varepsilon^4} \\ &\quad + \frac{8(\varepsilon - 1)(\varepsilon - 2)(C_2^x + C_2^y) + (\varepsilon^2 - 6\varepsilon + 6)(\varepsilon - 1)(\langle x \rangle + \langle y \rangle)}{\varepsilon^4} \end{aligned} \quad (\text{A9})$$

where N , n and i are non-negative integer numbers. The efficiency-corrected cumulants of net-proton distributions can be obtained from the efficiency-corrected moments by

where the (X, Y) and (x, y) are the numbers of (p, \bar{p}) produced and measured, respectively. The efficiency-corrected cumulants are sensitive to the efficiency and depend on the lower order measured cumulants.

In the current analysis, the proton and antiproton p_T range is from 0.4 to 2 GeV/c. This has been possible by using particle identification information for the TPG in the p_T range 0.4 to 0.8 GeV/c and the TPC+TOF in the momentum range 0.8 to 2 GeV/c. This results in two different efficiencies for proton reconstruction and two different values for antiprotons. Hence the above

formulation which holds for one single value of efficiency and $\varepsilon = \varepsilon_p = \varepsilon_{\bar{p}}$ has to be modified to take care of four different efficiency values, two each for the proton and antiproton corresponding to different p_T ranges. Let $\varepsilon_{p_1}, \varepsilon_{p_2}$ and $\varepsilon_{\bar{p}_1}, \varepsilon_{\bar{p}_2}$ denote the efficiency for protons and antiprotons in the two sub-phase spaces, and denote the corresponding number of protons and antiprotons in the two sub-phase spaces by N_{p_1}, N_{p_2} and $N_{\bar{p}_1}, N_{\bar{p}_2}$, respectively. Using analogous formulations as above, the bivariate factorial moments of protons and antiprotons distributions is given as:

$$\begin{aligned} F_{r_1, r_2}(N_p, N_{\bar{p}}) &= F_{r_1, r_2}(N_{p_1} + N_{p_2}, N_{\bar{p}_1} + N_{\bar{p}_2}) = \sum_{i_1=0}^{r_1} \sum_{i_2=0}^{r_2} s_1(r_1, i_1) s_1(r_2, i_2) \langle (N_{p_1} + N_{p_2})^{i_1} (N_{\bar{p}_1} + N_{\bar{p}_2})^{i_2} \rangle \\ &= \sum_{i_1=0}^{r_1} \sum_{i_2=0}^{r_2} s_1(r_1, i_1) s_1(r_2, i_2) \langle \sum_{s=0}^{i_1} \binom{i_1}{s} N_{p_1}^{i_1-s} N_{p_2}^s \sum_{t=0}^{i_2} \binom{i_2}{t} N_{\bar{p}_1}^{i_2-t} N_{\bar{p}_2}^t \rangle \\ &= \sum_{i_1=0}^{r_1} \sum_{i_2=0}^{r_2} \sum_{s=0}^{i_1} \sum_{t=0}^{i_2} s_1(r_1, i_1) s_1(r_2, i_2) \binom{i_1}{s} \binom{i_2}{t} \langle N_{p_1}^{i_1-s} N_{p_2}^s N_{\bar{p}_1}^{i_2-t} N_{\bar{p}_2}^t \rangle \\ &= \sum_{i_1=0}^{r_1} \sum_{i_2=0}^{r_2} \sum_{s=0}^{i_1} \sum_{t=0}^{i_2} \sum_{u=0}^{i_1-s} \sum_{v=0}^s \sum_{j=0}^{i_2-t} \sum_{k=0}^t s_1(r_1, i_1) s_1(r_2, i_2) \binom{i_1}{s} \binom{i_2}{t} \\ &\quad \times s_2(i_1 - s, u) s_2(s, v) s_2(i_2 - t, j) s_2(t, k) \times F_{u, v, j, k}(N_{p_1}, N_{p_2}, N_{\bar{p}_1}, N_{\bar{p}_2}) \end{aligned} \quad (\text{A10})$$

Similar to Eq. (A4) for the multivariate case, the efficiency-corrected multivariate factorial moments of

1969 proton and antiproton distributions in the current case
1970 are given as:

$$F_{u,v,j,k}(N_{p_1}, N_{p_2}, N_{\bar{p}_1}, N_{\bar{p}_2}) = \frac{f_{u,v,j,k}(n_{p_1}, n_{p_2}, n_{\bar{p}_1}, n_{\bar{p}_2})}{(\varepsilon_{p_1})^u (\varepsilon_{p_2})^v (\varepsilon_{\bar{p}_1})^j (\varepsilon_{\bar{p}_2})^k} \quad (\text{A11})$$

1971 where $f_{u,v,j,k}(N_{p_1}, N_{p_2}, N_{\bar{p}_1}, N_{\bar{p}_2})$ are the measured mul-
1972 tivariate factorial moments of proton and antiproton dis-
1973 tributions. By using Eq. (A5), (A8), (A10) and (A11),
1974 one can obtain the efficiency-corrected moments and cu-
1975 mulants of net-proton distributions for the case where
1976 the protons (antiprotons) have different efficiency in two
1977 sub-phase spaces. Through simulations as discussed in
1978 Refs. [104, 159], it has been shown that this formulation
1979 works consistently. Another binomial-model-based effi-
1980 ciency correction method using track-by-track efficiency

is discussed in Ref. [106].

1982 Appendix B: Statistical Uncertainties Estimation

According to Eqs. (A5), (A8) and (A10), the efficiency-
corrected moments are expressed in terms of the factori-
al moments, and thereby the factorial moments are the
random variable X_i in Eq. (15). The covariance of the
multivariate moments can be written as:

$$\text{Cov}(m_{r,s}, m_{u,v}) = \frac{1}{n} (m_{r+u, s+v} - m_{r,s} m_{u,v}) \quad (\text{B1})$$

where n is the number of events, $m_{r,s} = \langle X_1^r X_2^s \rangle$ and
 $m_{u,v} = \langle X_1^u X_2^v \rangle$ are the multivariate moments, and the
 X_1 and X_2 are random variables. In this paper, X_1
and X_2 represent proton and antiproton number, respec-
tively. Based on Eq. (B1), one can obtain the covariance
for the multivariate factorial moments as:

$$\begin{aligned} \text{Cov}(f_{r,s}, f_{u,v}) &= \text{Cov} \left(\sum_{i=0}^r \sum_{j=0}^s s_1(r,i) s_1(s,j) m_{i,j}, \sum_{k=0}^u \sum_{h=0}^v s_1(u,k) s_1(v,h) m_{k,h} \right) \\ &= \sum_{i=0}^r \sum_{j=0}^s \sum_{k=0}^u \sum_{h=0}^v s_1(r,i) s_1(s,j) s_1(u,k) s_1(v,h) \times \text{Cov}(m_{i,j}, m_{k,h}) \\ &= \frac{1}{n} \sum_{i=0}^r \sum_{j=0}^s \sum_{k=0}^u \sum_{h=0}^v s_1(r,i) s_1(s,j) s_1(u,k) s_1(v,h) \times (m_{i+k, j+h} - m_{i,j} m_{k,h}) \\ &= \frac{1}{n} (f_{(r,u),(s,v)} - f_{r,s} f_{u,v}) \end{aligned} \quad (\text{B2})$$

1994 where the $f_{(r,u),(s,v)}$ is defined as:

$$\begin{aligned} f_{(r,u),(s,v)} &= \left\langle \frac{X_1!}{(X_1-r)!} \frac{X_1!}{(X_1-u)!} \frac{X_2!}{(X_2-s)!} \frac{X_2!}{(X_2-v)!} \right\rangle \\ &= \sum_{i=0}^r \sum_{j=0}^s \sum_{k=0}^u \sum_{h=0}^v \sum_{\alpha=0}^{i+k} \sum_{\beta=0}^{j+h} s_1(r,i) s_1(s,j) s_1(u,k) s_1(v,h) \\ &\quad \times s_2(i+k, \alpha) s_2(j+h, \beta) f_{\alpha, \beta} \end{aligned} \quad (\text{B3})$$

1995 The definition of the bivariate factorial moments $f_{r,s}$
1996 $f_{u,v}$ and $f_{\alpha, \beta}$ can be found in Eq. (A3). The Equa-
1997 tion (B2) can be used in the standard error propaga-

1998 tion formula, Eq. (15), to obtain the statistical uncer-
1999 tainties of the efficiency-corrected cumulants. The de-
2000 tailed derivation of the analytical formulae for statistical
2001 uncertainties on cumulants and moments exists in the
2002 literature [104, 113]. If we put $\varepsilon_p = \varepsilon_{\bar{p}} = 1$, the statisti-
2003 cal uncertainties on the cumulants and cumulant ratios
2004 up to the eighth-order expressed in terms of central mo-
2005 ments (μ_n) are given below, where the uncertainties are
the square root of the variances.

$$\text{Var}(C_1) = \mu_2/n$$

$$\text{Var}(C_2) = (-\mu_2^2 + \mu_4)/n$$

$$\text{Var}(C_3) = (9\mu_2^3 - 6\mu_2\mu_4 - \mu_3^2 + \mu_6)/n$$

$$\text{Var}(C_4) = (-36\mu_2^4 + 48\mu_2^2\mu_4 + 64\mu_2\mu_3^2 - 12\mu_2\mu_6 - 8\mu_3\mu_5 - \mu_4^2 + \mu_8)/n$$

$$\text{Var}(C_5) = (\mu_{10} + 900\mu_2^5 - 900\mu_2^3\mu_4 - 1000\mu_2^2\mu_3^2 + 160\mu_2^2\mu_6 + 240\mu_2\mu_3\mu_5 + 125\mu_2\mu_4^2 - 20\mu_2\mu_8 + 200\mu_3^2\mu_4 - 20\mu_3\mu_7 - 10\mu_4\mu_6 - \mu_5^2)/n$$

$$\text{Var}(C_6) = (-30\mu_{10}\mu_2 + \mu_{12} - 8100\mu_2^6 + 13500\mu_2^4\mu_4 + 39600\mu_2^3\mu_3^2 - 2880\mu_2^3\mu_6 - 9720\mu_2^2\mu_3\mu_5 - 3600\mu_2^2\mu_4^2 + 405\mu_2^2\mu_8 - 9600\mu_2\mu_3^2\mu_4 + 840\mu_2\mu_3\mu_7 - 400\mu_4^4 + 216\mu_2\mu_5^2 + 510\mu_2\mu_4\mu_6 + 440\mu_3^2\mu_6 + 1020\mu_3\mu_4\mu_5 - 40\mu_3\mu_9 + 225\mu_4^3 - 30\mu_4\mu_8 - 12\mu_5\mu_7 - \mu_6^2)/n$$

$$\text{Var}(C_7) = (861\mu_{10}\mu_2^2 - 70\mu_{10}\mu_4 - 70\mu_{11}\mu_3 - 42\mu_{12}\mu_2 + \mu_{14} + 396900\mu_2^7 - 529200\mu_2^5\mu_4 - 1102500\mu_2^4\mu_3^2 + 79380\mu_2^4\mu_6 + 299880\mu_2^3\mu_3\mu_5 + 176400\mu_2^3\mu_4^2 - 10080\mu_2^3\mu_8 + 558600\mu_2^2\mu_3^2\mu_4 - 33600\mu_2^2\mu_3\mu_7 - 29400\mu_2^2\mu_4\mu_6 - 10584\mu_2^2\mu_5^2 + 137200\mu_2\mu_3^4 - 43120\mu_2\mu_3^2\mu_6 - 76440\mu_2\mu_3\mu_4\mu_5 + 2310\mu_2\mu_3\mu_9 - 14700\mu_2\mu_4^3 + 1890\mu_2\mu_4\mu_8 + 966\mu_2\mu_5\mu_7 + 343\mu_2\mu_6^2 - 15680\mu_3^3\mu_5 - 14700\mu_3^2\mu_4^2 + 1505\mu_3^2\mu_8 + 2590\mu_3\mu_4\mu_7 + 2254\mu_3\mu_5\mu_6 + 1715\mu_4^2\mu_6 + 1911\mu_4\mu_5^2 - 42\mu_5\mu_9 - 14\mu_6\mu_8 - \mu_7^2)/n$$

$$\text{Var}(C_8) = (-28560\mu_{10}\mu_2^3 + 5600\mu_{10}\mu_2\mu_4 + 4256\mu_{10}\mu_3^2 - 56\mu_{10}\mu_6 + 5376\mu_{11}\mu_2\mu_3 - 112\mu_{11}\mu_5 + 1624\mu_{12}\mu_2^2 - 140\mu_{12}\mu_4 - 112\mu_{13}\mu_3 - 56\mu_{14}\mu_2 + \mu_{16} - 6350400\mu_2^8 + 12700800\mu_2^6\mu_4 + 59270400\mu_2^5\mu_3^2 - 2399040\mu_2^5\mu_6 - 15523200\mu_2^4\mu_3\mu_5 - 6174000\mu_2^4\mu_4^2 + 322560\mu_2^4\mu_8 - 35280000\mu_2^3\mu_3^2\mu_4 + 1626240\mu_2^3\mu_3\mu_7 + 1340640\mu_2^3\mu_4\mu_6 + 677376\mu_2^3\mu_5^2 - 8467200\mu_2^2\mu_3^4 + 2759680\mu_2^2\mu_3^2\mu_6 + 5597760\mu_2^2\mu_3\mu_4\mu_5 - 119840\mu_2^2\mu_3\mu_9 + 882000\mu_2^2\mu_4^3 - 108360\mu_2^2\mu_4\mu_8 - 77952\mu_2^2\mu_5\mu_7 - 26656\mu_2^2\mu_6^2 + 2007040\mu_2\mu_3^3\mu_5 + 3684800\mu_2\mu_3^2\mu_4^2 - 160160\mu_2\mu_3^2\mu_8 - 322560\mu_2\mu_3\mu_4\mu_7 - 257152\mu_2\mu_3\mu_5\mu_6 - 172480\mu_2\mu_4^2\mu_6 - 178752\mu_2\mu_4\mu_5^2 + 3808\mu_2\mu_5\mu_9 + 1680\mu_2\mu_6\mu_8 + 512\mu_2\mu_7^2 + 940800\mu_3^4\mu_4 - 71680\mu_3^3\mu_7 - 203840\mu_3^2\mu_4\mu_6 - 75264\mu_3^2\mu_5^2 - 156800\mu_3\mu_4^2\mu_5 + 8960\mu_3\mu_4\mu_9 + 6496\mu_3\mu_5\mu_8 + 4480\mu_3\mu_6\mu_7 - 4900\mu_4^4 + 5040\mu_4^2\mu_8 + 9856\mu_4\mu_5\mu_7 + 4704\mu_4\mu_6^2 + 6272\mu_5^2\mu_6 - 16\mu_7\mu_9 - \mu_8^2)/n$$

$$\text{Var}\left(\frac{C_2}{C_1}\right) = \left(-\frac{\mu_2^2}{\langle N \rangle^2} + \frac{\mu_4}{\langle N \rangle^2} - \frac{2\mu_2\mu_3}{\langle N \rangle^3} + \frac{\mu_2^3}{\langle N \rangle^4}\right)/n$$

$$\text{Var}\left(\frac{C_3}{C_2}\right) = \left(9\mu_2 - \frac{6\mu_4}{\mu_2} + \frac{6\mu_3^2}{\mu_2^2} + \frac{\mu_6}{\mu_2} - \frac{2\mu_3\mu_5}{\mu_2^2} + \frac{\mu_3^2\mu_4}{\mu_2^4}\right)/n$$

$$\text{Var}\left(\frac{C_4}{C_2}\right) = \left(-9\mu_2^2 + 9\mu_4 + \frac{40\mu_3^2}{\mu_2} - \frac{6\mu_6}{\mu_2} - \frac{8\mu_3\mu_5}{\mu_2^2} + \frac{6\mu_4^2}{\mu_2^2} + \frac{\mu_8}{\mu_2^2} + \frac{8\mu_3^2\mu_4}{\mu_2^3} - \frac{2\mu_4\mu_6}{\mu_2^3} + \frac{\mu_4^3}{\mu_2^4}\right)/n$$

$$\begin{aligned}
\text{Var}\left(\frac{C_5}{C_1}\right) &= \left(\frac{\mu_{10}}{\langle N \rangle^2} + \frac{900\mu_2^5}{\langle N \rangle^2} - \frac{900\mu_2^3\mu_4}{\langle N \rangle^2} - \frac{1000\mu_2^2\mu_3^2}{\langle N \rangle^2} + \frac{160\mu_2^2\mu_6}{\langle N \rangle^2} + \frac{240\mu_2\mu_3\mu_5}{\langle N \rangle^2} + \frac{125\mu_2\mu_4^2}{\langle N \rangle^2} \right. \\
&\quad - \frac{20\mu_2\mu_8}{\langle N \rangle^2} + \frac{200\mu_3^2\mu_4}{\langle N \rangle^2} - \frac{20\mu_3\mu_7}{\langle N \rangle^2} - \frac{10\mu_4\mu_6}{\langle N \rangle^2} - \frac{\mu_5^2}{\langle N \rangle^2} + \frac{600\mu_2^4\mu_3}{\langle N \rangle^3} - \frac{60\mu_2^3\mu_5}{\langle N \rangle^3} - \frac{300\mu_2^2\mu_3\mu_4}{\langle N \rangle^3} \\
&\quad \left. - \frac{200\mu_2\mu_3^3}{\langle N \rangle^3} + \frac{20\mu_2\mu_3\mu_6}{\langle N \rangle^3} + \frac{30\mu_2\mu_4\mu_5}{\langle N \rangle^3} + \frac{20\mu_3^2\mu_5}{\langle N \rangle^3} - \frac{2\mu_5\mu_6}{\langle N \rangle^3} + \frac{100\mu_3^3\mu_2^2}{\langle N \rangle^4} - \frac{20\mu_2^2\mu_3\mu_5}{\langle N \rangle^4} + \frac{\mu_2\mu_5^2}{\langle N \rangle^4} \right) / n \\
\text{Var}\left(\frac{C_6}{C_2}\right) &= \left(-\frac{30\mu_{10}}{\mu_2} + \frac{\mu_{12}}{\mu_2^2} - 3600\mu_2^4 + 5400\mu_2^2\mu_4 + 30000\mu_2\mu_3^2 - 1800\mu_2\mu_6 - 8160\mu_3\mu_5 - 225\mu_4^2 \right. \\
&\quad + 345\mu_8 - \frac{3900\mu_3^2\mu_4}{\mu_2} + \frac{840\mu_3\mu_7}{\mu_2} - \frac{120\mu_4\mu_6}{\mu_2} + \frac{216\mu_5^2}{\mu_2} + \frac{2300\mu_3^4}{\mu_2^2} - \frac{140\mu_2^3\mu_6}{\mu_2^2} + \frac{240\mu_3\mu_4\mu_5}{\mu_2^2} \\
&\quad - \frac{40\mu_3\mu_9}{\mu_2^2} - \frac{12\mu_5\mu_7}{\mu_2^2} + \frac{30\mu_6^2}{\mu_2^2} - \frac{520\mu_3^3\mu_5}{\mu_2^3} + \frac{20\mu_3^2\mu_8}{\mu_2^3} + \frac{52\mu_3\mu_5\mu_6}{\mu_2^3} - \frac{2\mu_6\mu_8}{\mu_2^3} + \frac{100\mu_3^4\mu_4}{\mu_2^4} \\
&\quad \left. - \frac{20\mu_3^2\mu_4\mu_6}{\mu_2^4} + \frac{\mu_4\mu_6^2}{\mu_2^4} \right) / n \\
\text{Var}\left(\frac{C_7}{C_1}\right) &= \left(\frac{861\mu_{10}\mu_2^2}{\langle N \rangle^2} - \frac{70\mu_{10}\mu_4}{\langle N \rangle^2} - \frac{70\mu_{11}\mu_3}{\langle N \rangle^2} - \frac{42\mu_{12}\mu_2}{\langle N \rangle^2} + \frac{\mu_{14}}{\langle N \rangle^2} + \frac{396900\mu_2^7}{\langle N \rangle^2} - \frac{529200\mu_2^5\mu_4}{\langle N \rangle^2} \right. \\
&\quad - \frac{1102500\mu_2^4\mu_3^2}{\langle N \rangle^2} + \frac{79380\mu_2^4\mu_6}{\langle N \rangle^2} + \frac{299880\mu_2^3\mu_3\mu_5}{\langle N \rangle^2} + \frac{176400\mu_2^3\mu_4^2}{\langle N \rangle^2} - \frac{10080\mu_2^3\mu_8}{\langle N \rangle^2} \\
&\quad + \frac{558600\mu_2^2\mu_3^2\mu_4}{\langle N \rangle^2} - \frac{33600\mu_2^2\mu_3\mu_7}{\langle N \rangle^2} - \frac{29400\mu_2^2\mu_4\mu_6}{\langle N \rangle^2} - \frac{10584\mu_2^2\mu_5^2}{\langle N \rangle^2} + \frac{137200\mu_2\mu_4^3}{\langle N \rangle^2} \\
&\quad - \frac{43120\mu_2\mu_3^2\mu_6}{\langle N \rangle^2} - \frac{76440\mu_2\mu_3\mu_4\mu_5}{\langle N \rangle^2} + \frac{2310\mu_2\mu_3\mu_9}{\langle N \rangle^2} - \frac{14700\mu_2\mu_4^3}{\langle N \rangle^2} + \frac{1890\mu_2\mu_4\mu_8}{\langle N \rangle^2} \\
&\quad + \frac{966\mu_2\mu_5\mu_7}{\langle N \rangle^2} + \frac{343\mu_2\mu_6^2}{\langle N \rangle^2} - \frac{15680\mu_3^3\mu_5}{\langle N \rangle^2} - \frac{14700\mu_3^2\mu_4^2}{\langle N \rangle^2} + \frac{1505\mu_3^2\mu_8}{\langle N \rangle^2} + \frac{2590\mu_3\mu_4\mu_7}{\langle N \rangle^2} \\
&\quad + \frac{2254\mu_3\mu_5\mu_6}{\langle N \rangle^2} + \frac{1715\mu_4^2\mu_6}{\langle N \rangle^2} + \frac{1911\mu_4\mu_5^2}{\langle N \rangle^2} - \frac{42\mu_5\mu_9}{\langle N \rangle^2} - \frac{14\mu_6\mu_8}{\langle N \rangle^2} - \frac{\mu_7^2}{\langle N \rangle^2} + \frac{264600\mu_2^6\mu_3}{\langle N \rangle^3} \\
&\quad - \frac{26460\mu_2^5\mu_5}{\langle N \rangle^3} - \frac{220500\mu_2^4\mu_3\mu_4}{\langle N \rangle^3} + \frac{1260\mu_2^4\mu_7}{\langle N \rangle^3} - \frac{235200\mu_2^3\mu_3^3}{\langle N \rangle^3} + \frac{11760\mu_2^3\mu_3\mu_6}{\langle N \rangle^3} \\
&\quad + \frac{17640\mu_2^3\mu_4\mu_5}{\langle N \rangle^3} + \frac{47040\mu_2^2\mu_3^2\mu_5}{\langle N \rangle^3} + \frac{44100\mu_2^2\mu_3\mu_4^2}{\langle N \rangle^3} - \frac{420\mu_2^2\mu_3\mu_8}{\langle N \rangle^3} - \frac{840\mu_2^2\mu_4\mu_7}{\langle N \rangle^3} \\
&\quad - \frac{1176\mu_2^2\mu_5\mu_6}{\langle N \rangle^3} + \frac{39200\mu_2\mu_3^3\mu_4}{\langle N \rangle^3} - \frac{1120\mu_2\mu_3^2\mu_7}{\langle N \rangle^3} - \frac{1960\mu_2\mu_3\mu_4\mu_6}{\langle N \rangle^3} - \frac{2352\mu_2\mu_3\mu_5^2}{\langle N \rangle^3} \\
&\quad - \frac{1470\mu_2\mu_4^2\mu_5}{\langle N \rangle^3} + \frac{42\mu_2\mu_5\mu_8}{\langle N \rangle^3} + \frac{56\mu_2\mu_6\mu_7}{\langle N \rangle^3} - \frac{3920\mu_3^2\mu_4\mu_5}{\langle N \rangle^3} - \frac{2450\mu_3\mu_4^3}{\langle N \rangle^3} + \frac{70\mu_3\mu_4\mu_8}{\langle N \rangle^3} \\
&\quad + \frac{112\mu_3\mu_5\mu_7}{\langle N \rangle^3} + \frac{70\mu_4^2\mu_7}{\langle N \rangle^3} - \frac{2\mu_7\mu_8}{\langle N \rangle^3} + \frac{44100\mu_2^5\mu_3^2}{\langle N \rangle^4} - \frac{8820\mu_2^4\mu_3\mu_5}{\langle N \rangle^4} - \frac{14700\mu_2^3\mu_3^2\mu_4}{\langle N \rangle^4} \\
&\quad + \frac{420\mu_2^3\mu_3\mu_7}{\langle N \rangle^4} + \frac{441\mu_2^3\mu_5^2}{\langle N \rangle^4} + \frac{1470\mu_2^2\mu_3\mu_4\mu_5}{\langle N \rangle^4} \\
&\quad \left. - \frac{42\mu_2^2\mu_5\mu_7}{\langle N \rangle^4} + \frac{1225\mu_2\mu_3^2\mu_4^2}{\langle N \rangle^4} - \frac{70\mu_2\mu_3\mu_4\mu_7}{\langle N \rangle^4} + \frac{\mu_2\mu_7^2}{\langle N \rangle^4} \right) / n
\end{aligned}$$

$$\begin{aligned}
\text{Var}\left(\frac{C_8}{C_2}\right) = & (-27300\mu_{10}\mu_2 + \frac{4760\mu_{10}\mu_4}{\mu_2} + \frac{3136\mu_{10}\mu_3^2}{\mu_2^2} + \frac{112\mu_{10}\mu_3\mu_5}{\mu_2^3} + \frac{70\mu_{10}\mu_4^2}{\mu_2^3} - \frac{2\mu_{10}\mu_8}{\mu_2^3} \\
& + \frac{5376\mu_{11}\mu_3}{\mu_2} - \frac{112\mu_{11}\mu_5}{\mu_2^2} + 1624\mu_{12} - \frac{140\mu_{12}\mu_4}{\mu_2^2} - \frac{112\mu_{13}\mu_3}{\mu_2^2} - \frac{56\mu_{14}}{\mu_2} + \frac{\mu_{16}}{\mu_2^2} \\
& - 3572100\mu_2^6 + 6747300\mu_2^4\mu_4 + 48686400\mu_2^3\mu_3^2 - 1693440\mu_2^3\mu_6 - 13335840\mu_2^2\mu_3\mu_5 \\
& - 2425500\mu_2^2\mu_4^2 + 282240\mu_2^2\mu_8 - 25166400\mu_2\mu_3^2\mu_4 + 1545600\mu_2\mu_3\mu_7 + 664440\mu_2\mu_4\mu_6 \\
& + 606816\mu_2\mu_5^2 - 1254400\mu_3^4 + 1881600\mu_3^2\mu_6 + 3974880\mu_3\mu_4\mu_5 - 119840\mu_3\mu_9 + 102900\mu_4^3 \\
& - 78540\mu_4\mu_8 - 77952\mu_5\mu_7 - 784\mu_6^2 - \frac{439040\mu_3^3\mu_5}{\mu_2} + \frac{1764000\mu_3^2\mu_4^2}{\mu_2} - \frac{115360\mu_3^2\mu_8}{\mu_2} \\
& - \frac{268800\mu_3\mu_4\mu_7}{\mu_2} - \frac{119168\mu_3\mu_5\mu_6}{\mu_2} - \frac{31360\mu_4^2\mu_6}{\mu_2} - \frac{131712\mu_4\mu_5^2}{\mu_2} + \frac{3808\mu_5\mu_9}{\mu_2} \\
& - \frac{840\mu_6\mu_8}{\mu_2} + \frac{512\mu_7^2}{\mu_2} - \frac{62720\mu_3^2\mu_4\mu_6}{\mu_2^2} + \frac{159936\mu_3^2\mu_5^2}{\mu_2^2} + \frac{3920\mu_3\mu_4^2\mu_5}{\mu_2^2} + \frac{8960\mu_3\mu_4\mu_9}{\mu_2^2} \\
& + \frac{224\mu_3\mu_5\mu_8}{\mu_2^2} + \frac{896\mu_3\mu_6\mu_7}{\mu_2^2} + \frac{28175\mu_4^4}{\mu_2^2} + \frac{2100\mu_4^2\mu_8}{\mu_2^2} + \frac{9856\mu_4\mu_5\mu_7}{\mu_2^2} + \frac{3136\mu_5^2\mu_6}{\mu_2^2} \\
& - \frac{16\mu_7\mu_9}{\mu_2^2} + \frac{56\mu_8^2}{\mu_2^2} + \frac{62720\mu_3^3\mu_4\mu_5}{\mu_2^3} + \frac{39200\mu_3^2\mu_4^3}{\mu_2^3} - \frac{1120\mu_3^2\mu_4\mu_8}{\mu_2^3} - \frac{7168\mu_3^2\mu_5\mu_7}{\mu_2^3} \\
& - \frac{4480\mu_3\mu_4^2\mu_7}{\mu_2^3} - \frac{7840\mu_3\mu_4\mu_5\mu_6}{\mu_2^3} - \frac{6272\mu_3\mu_5^3}{\mu_2^3} + \frac{128\mu_3\mu_7\mu_8}{\mu_2^3} - \frac{4900\mu_4^3\mu_6}{\mu_2^3} - \frac{3920\mu_4^2\mu_5^2}{\mu_2^3} \\
& + \frac{140\mu_4\mu_6\mu_8}{\mu_2^3} + \frac{112\mu_5^2\mu_8}{\mu_2^3} + \frac{3136\mu_3^2\mu_4\mu_5^2}{\mu_2^4} + \frac{3920\mu_3\mu_4^3\mu_5}{\mu_2^4} \\
& - \frac{112\mu_3\mu_4\mu_5\mu_8}{\mu_2^4} + \frac{1225\mu_4^5}{\mu_2^4} - \frac{70\mu_4^3\mu_8}{\mu_2^4} + \frac{\mu_4\mu_8^2}{\mu_2^4})/n
\end{aligned}$$
